

Murat SERTKOL

M.S. Thesis in Physics

August - 2008

**PREPARATION AND MAGNETIC
CHARACTERIZATION
OF
MICROWAVE ABSORBING MAGNETIC
NANOCOMPOSITES**

by

Murat SERTKOL

August 2008

**PREPARATION AND MAGNETIC CHARACTERIZATION
OF
MICROWAVE ABSORBING MAGNETIC NANOCOMPOSITES**

by

Murat SERTKOL

A thesis submitted to

the Graduate Institute of Sciences and Engineering

of

Fatih University

in partial fulfillment of the requirements for the degree of

Master of Science

in

Physics

August 2008
Istanbul, Turkey

APPROVAL PAGE

I certify that this thesis satisfies all the requirements as a thesis for the degree of Master of Science.

Prof. Dr. Mustafa KUMRU
Head of Department

This is to certify that I have read this thesis and that in my opinion it is fully adequate, in scope and quality, as a thesis for the degree of Master of Science.

Assist. Prof. Dr. Yüksel KÖSEOĞLU
Supervisor

Examining Committee Members

Assoc. Prof. Dr. Yüksel KÖSEOĞLU

Prof. Dr. Mustafa KUMRU

Assist. Prof. Dr. Abdülhadi BAYKAL

It is approved that this thesis has been written in compliance with the formatting rules laid down by the Graduate Institute of Sciences and Engineering.

Assist. Prof. Dr. Nurullah ARSLAN
Director

August 2008

**PREPARATION AND MAGNETIC CHARACTERIZATION
OF
MICROWAVE ABSORBING MAGNETIC NANOCOMPOSITES**

Murat SERTKOL

M.S. Thesis – Physics
August 2008

Supervisor: Assoc. Prof. Dr. Yüksel KÖSEOĞLU

ABSTRACT

Magnetic Ni-Zn ferrites are important because of their microwave absorptions due to their advantages in weight, design flexibility, low cost, and other microwave properties over many different kinds of spinels. The magnetic properties of ferrites are known to control by changing synthesis methods. In this study, we have synthesized $Zn_xNi_{1-x}Fe_2O_4$ ($x = 0.0 - 1.0$) nanoparticles by using PEG 400 assisted hydrothermal method and microwave combustion method (urea and citric acid used as fuel). The effects of the synthesis methods on the structural and magnetic properties of the Ni-Zn ferrite nanoparticles have been studied. Advantages and disadvantages of the fuels and surfactants to the magnetism of nanosize Ni-Zn ferrite compounds are compared and analysed.

The coercivity, saturation and remanent magnetizations, and changes in magnetic properties are investigated. The effect of the urea, citric acid as fuels and PEG 400 (Polyethylene Glycol 400) as a surfactant to the magnetic properties for the Zn doped

Ni-ferrites are investigated. The crystallite sizes (with XRD powder diffraction, TEM and VSM), blocking temperatures (T_B or Curie temperature) are determined and compared.

Keywords: Superparamagnetism, spinel structure, saturation magnetization, magnetic nanoparticles, blocking temperature.

MİKRODALGA SOĞURUCU MANYETİK NANOKOMPOZİTLERİN HAZIRLANMASI VE MANYETİK KARAKTERİZASYONU

Murat SERTKOL

Yüksek Lisans Tezi – Fizik
Ağustos 2008

Tez Yöneticisi: Doç. Dr. Yüksel KÖSEOĞLU

ÖZ

Manyetik Ni-Zn feritler hafiflik, tasarım esnekliği, düşük maliyet ve diğer birçok spinellerden daha fazla mikrodalga soğurabilme özelliklerinden dolayı önemlidir. Ferritlerin manyetik özelliklerinin sentez metodunu değiştirerek kontrol edilebildiği bilinmektedir. Bu çalışmada $Zn_xNi_{1-x}Fe_2O_4$ ($x = 0.0 - 1.0$) nanoparçacıklar PEG 400 kaplamalı hidrotermal metot ve mikrodalga yanma metodu (üre ve sitrik asit yakıt olarak kullanıldı) sentezlendi. Artık (coercivity) ve kalan (remanent) mıknatıslanmaları, doyum mıknatıslanmaları mikrodalga yanma metodu ve hidrotermal metodun avantaj ve dezavantajlarının karşılaştırılmasıyla manyetik özelliklerindeki değişimler incelenmiştir.

Zn katkılı Ni-ferrit bileşiklerinde yakıt olarak kullanılan üre ve sitrik asit ile kaplama malzemesi olarak PEG 400 (Polietilenglikol 400) gibi yüzey etkin maddelerin manyetik özelliklere etkisi araştırılmıştır. Kristal büyüklükleri (X-Işını Toz Difraktometresi, Geçirgen Elektron Mikroskop ve Numune Titreştirici Manyetometre), geçiş sıcaklığı (T_B ya da Curie sıcaklığı) belirlendi.

Anahtar Kelimeler: Süperparamanyetizma, spinel yapılar, doyum manyetizasyonu, manyetik nanoparçacıklar, geçiş sıcaklığı.

ACKNOWLEDGEMENT

Firstly, I would like to gratitude to my supervisor Assoc. Prof. Dr. Yüksel KÖSEOĞLU for his motivation, help, stimulating and incentive suggestions during whole time of research and efforts for writing this thesis.

I want to thank to Prof. Dr. Mustafa KUMRU for his stimulation and motivation in my thesis.

My special thanks go to Assist. Prof. Dr. Abdülhadi BAYKAL for his heartfelt helps in FT-IR, XRD and valuable advices, motivation and collaboration in my thesis. I am grateful to Ms. Nermin KASAPOĞLU and Ms. Tevhide Ö. AHMADOV for their supports.

I am also thankful to the nanosicence group member Res. Assist. Hüseyin KAVAS for his efforts and significance advices to achieve novel analysis methods such as a goal in magnetic studies.

I am grateful to the Prof. Dr. Bekir AKTAŞ for his encouragement and significant suggestions which made this work successful. I also want to thank to Res. Assist. Ali Cemil BAŞARAN and TEM Technician Ömer DENİZ for their contributions during measurements.

Finally I want to thank to my university for funding this research with the project no. of P50010701.

TABLE OF CONTENTS

| | |
|--|-------|
| ABSTRACT..... | iii |
| ÖZ..... | v |
| ACKNOWLEDGEMENT..... | vi |
| TABLE OF CONTENTS..... | vii |
| LIST OF FIGURES..... | x |
| LIST OF TABLES..... | xv |
| LIST OF SYMBOLS AND ABBREVIATIONS..... | xviii |
| CHAPTER 1 INTRODUCTION..... | 1 |
| CHAPTER 2 THEORY OF MAGNETISM..... | 5 |
| 2.1 Magnetization and Magnetic Field..... | 5 |
| 2.2 Classification of Magnetic Materials and Types of Magnetism..... | 7 |
| 2.3 The Hysteresis Loop and Magnetic Properties..... | 10 |
| 2.4 Theory of Superparamagnetism and Paramagnetism..... | 12 |
| 2.5 The Spinel Structure and Ferrites..... | 14 |
| CHAPTER 3 EXPERIMENTAL AND CHARACTERIZATION..... | 18 |
| 3.1 Synthesis Methods..... | 18 |
| 3.1.1 Microwave Combustion Method..... | 19 |
| 3.1.2 Hydrothermal Method..... | 22 |
| 3.2 Characterization Techniques..... | 24 |
| 3.2.1 Fourier Transform Infrared Spectroscopy (FT-IR)..... | 24 |
| 3.2.2 X-RAY Powder Diffractometry (XRD)..... | 24 |
| 3.2.3 Transmission Electron Microscopy (TEM)..... | 26 |
| 3.2.4 Magnetic Measurements..... | 27 |
| CHAPTER 4 RESULTS AND DISCUSSION..... | 28 |
| 4.1 Microwave Combustion Method: Synthesis with Citric Acid as Fuel..... | 28 |

| | |
|--|----|
| 4.1.1 FT-IR Analysis..... | 28 |
| 4.1.2 X-Ray Powder Diffraction Analysis..... | 29 |
| 4.1.3 TEM Micrographs of $Zn_xNi_{1-x}Fe_2O_4$ Nanoparticles with Citric Acid..... | 32 |
| 4.1.3.1 $NiFe_2O_4$ and $Zn_{0.2}Ni_{0.8}Fe_2O_4$ Nanoparticles..... | 33 |
| 4.1.3.2 $Zn_{0.5}Ni_{0.5}Fe_2O_4$ and $Zn_{0.7}Ni_{0.3}Fe_2O_4$ Nanoparticles..... | 34 |
| 4.1.3.3 $ZnFe_2O_4$ Nanoparticles..... | 35 |
| 4.2 Microwave Combustion Method: Synthesis with Urea as Fuel..... | 35 |
| 4.2.1 FT-IR Analysis..... | 36 |
| 4.2.2 X-Ray Powder Diffraction Analysis..... | 37 |
| 4.2.3 TEM Micrographs of $Zn_xNi_{1-x}Fe_2O_4$ Nanoparticles with Urea..... | 39 |
| 4.2.3.1 $NiFe_2O_4$ and $Zn_{0.2}Ni_{0.8}Fe_2O_4$ Nanoparticles..... | 39 |
| 4.2.3.2 $Zn_{0.5}Ni_{0.5}Fe_2O_4$ and $Zn_{0.7}Ni_{0.3}Fe_2O_4$ Nanoparticles..... | 40 |
| 4.2.3.3 $ZnFe_2O_4$ Nanoparticles..... | 41 |
| 4.3 Results of Magnetization Measurements for $Zn_xNi_{1-x}Fe_2O_4$ Samples Synthesized by Microwave Combustion Method..... | 42 |
| 4.3.1 $NiFe_2O_4$ Nanoparticles..... | 42 |
| 4.3.2 $Zn_{0.2}Ni_{0.8}Fe_2O_4$ Nanoparticles..... | 43 |
| 4.3.3 $Zn_{0.5}Ni_{0.5}Fe_2O_4$ Nanoparticles..... | 45 |
| 4.3.4 $Zn_{0.7}Ni_{0.3}Fe_2O_4$ Nanoparticles..... | 46 |
| 4.3.5 $ZnFe_2O_4$ Nanoparticles..... | 47 |
| 4.4 Hydrothermal Method: Synthesis with PEG 400 as a Surfactant..... | 50 |
| 4.4.1 FT-IR Analysis..... | 50 |
| 4.4.2 X-Ray Powder Diffraction Analysis..... | 51 |
| 4.4.3 TEM Micrographs of $Zn_xNi_{1-x}Fe_2O_4$ Nanoparticles with PEG 400..... | 57 |
| 4.4.3.1 $NiFe_2O_4$ Nanoparticles..... | 57 |
| 4.4.3.2 $Zn_{0.2}Ni_{0.8}Fe_2O_4$ Nanoparticles..... | 58 |
| 4.4.3.3 $Zn_{0.4}Ni_{0.6}Fe_2O_4$ Nanoparticles..... | 59 |

| | |
|--|----|
| 4.4.3.4 Zn _{0.6} Ni _{0.4} Fe ₂ O ₄ Nanoparticles..... | 60 |
| 4.4.3.5 Zn _{0.8} Ni _{0.2} Fe ₂ O ₄ Nanoparticles..... | 61 |
| 4.4.3.6 ZnFe ₂ O ₄ Nanoparticles..... | 62 |
| 4.4.4 Results of Magnetic Measurements for Zn _x Ni _{1-x} Fe ₂ O ₄ Samples Synthesized by PEG Assisted Hydrothermal Route..... | 65 |
| 4.4.4.1 NiFe ₂ O ₄ Nanoparticles..... | 66 |
| 4.4.4.2 Zn _{0.2} Ni _{0.8} Fe ₂ O ₄ Nanoparticles..... | 69 |
| 4.4.4.3 Zn _{0.4} Ni _{0.6} Fe ₂ O ₄ Nanoparticles..... | 72 |
| 4.4.4.4 Zn _{0.6} Ni _{0.4} Fe ₂ O ₄ Nanoparticles..... | 75 |
| 4.4.4.5 Zn _{0.8} Ni _{0.2} Fe ₂ O ₄ Nanoparticles..... | 78 |
| 4.4.4.6 ZnFe ₂ O ₄ Nanoparticles..... | 81 |
| CHAPTER 5 CONCLUSION..... | 92 |
| REFERENCES..... | 95 |

LIST OF FIGURES

| | | |
|------------|--|----|
| Figure 2.1 | Hysteresis loop sample for a ferromagnet..... | 11 |
| Figure 2.2 | Tetrahedral and octahedral sites in a crystal structure..... | 14 |
| Figure 2.3 | Crystal structure of spinel..... | 15 |
| Figure 2.4 | The coercivity of soft ferrites and hard ferrites..... | 17 |
| Figure 3.1 | Synthesis outline of our samples..... | 18 |
| Figure 3.2 | Combustion reaction of $Zn_xNi_{1-x}Fe_2O_4$ nanoparticles..... | 19 |
| Figure 3.3 | Autoclaves used for hydrothermal synthesis..... | 22 |
| Figure 3.4 | Sample in Cartesian coordinate system and specific angles for XRD measurements..... | 25 |
| Figure 4.1 | FT-IR spectra of the $Zn_xNi_{1-x}Fe_2O_4$ nanoparticles with Zn contents of $x = 0.0, 0.2, 0.5, 0.7$ and 1.0 synthesized by microwave combustion method using citric acid as fuel..... | 29 |
| Figure 4.2 | X-Ray diffraction pattern for $Zn_xNi_{1-x}Fe_2O_4$ nanoparticles with Zinc contents of $x = 0.0, 0.2, 0.4, 0.6, 0.8$ and 1.0 synthesized by microwave combustion method using citric acid as fuel..... | 30 |
| Figure 4.3 | Lattice parameters of $Zn_xNi_{1-x}Fe_2O_4$ nanoparticles with synthesized by microwave method using citric acid as fuel..... | 31 |
| Figure 4.4 | (a) The TEM micrograph of $NiFe_2O_4$ nanoparticles synthesized by using citric acid, (b) The TEM micrograph of $Zn_{0.2}Ni_{0.8}Fe_2O_4$ nanoparticles..... | 33 |
| Figure 4.5 | (a) The TEM micrograph of $Zn_{0.5}Ni_{0.5}Fe_2O_4$ nanoparticles synthesized by using citric acid, (b) The TEM micrograph of $Zn_{0.7}Ni_{0.3}Fe_2O_4$ nanoparticles..... | 34 |

| | | |
|-------------|--|----|
| Figure 4.6 | The TEM micrograph of ZnFe_2O_4 nanoparticles synthesized by using citric acid..... | 35 |
| Figure 4.7 | FT-IR spectra of the $\text{Zn}_x\text{Ni}_{1-x}\text{Fe}_2\text{O}_4$ nanoparticles with Zn contents of $x = 0.0, 0.2, 0.5, 0.7$ and 1.0 synthesized by microwave combustion method using urea as fuel..... | 36 |
| Figure 4.8 | X-Ray diffraction pattern for $\text{Zn}_x\text{Ni}_{1-x}\text{Fe}_2\text{O}_4$ nanoparticles with Zinc contents of $x = 0.0, 0.2, 0.4, 0.6, 0.8$ and 1.0 synthesized by microwave combustion method using urea as fuel..... | 37 |
| Figure 4.9 | Lattice parameters of $\text{Zn}_x\text{Ni}_{1-x}\text{Fe}_2\text{O}_4$ nanoparticles with synthesized by microwave method using urea as fuel..... | 38 |
| Figure 4.10 | (a) The TEM micrograph of NiFe_2O_4 nanoparticles synthesized by using urea, (b) The TEM micrograph of $\text{Zn}_{0.2}\text{Ni}_{0.8}\text{Fe}_2\text{O}_4$ nanoparticles..... | 39 |
| Figure 4.11 | (a) The TEM micrograph of $\text{Zn}_{0.5}\text{Ni}_{0.5}\text{Fe}_2\text{O}_4$ nanoparticles synthesized by using urea, (b) The TEM micrograph of $\text{Zn}_{0.7}\text{Ni}_{0.3}\text{Fe}_2\text{O}_4$ nanoparticles..... | 40 |
| Figure 4.12 | The TEM micrograph of ZnFe_2O_4 nanoparticles synthesized by using urea..... | 41 |
| Figure 4.13 | Magnetic field vs magnetization curve of NiFe_2O_4 synthesized by microwave combustion method using urea and citric acid as fuel at room temperature..... | 43 |
| Figure 4.14 | Magnetic field vs magnetization curve of $\text{Zn}_{0.2}\text{Ni}_{0.8}\text{Fe}_2\text{O}_4$ synthesized by microwave combustion method using urea and citric acid as fuel at room temperature..... | 44 |
| Figure 4.15 | Magnetic field vs magnetization curve of $\text{Zn}_{0.5}\text{Ni}_{0.5}\text{Fe}_2\text{O}_4$ synthesized by microwave combustion method using urea and citric acid as fuel at room temperature..... | 45 |

| | | |
|-------------|--|----|
| Figure 4.16 | Magnetic field vs magnetization curve of $Zn_{0.7}Ni_{0.3}Fe_2O_4$ synthesized by microwave combustion method using urea and citric acid as fuel at room temperature..... | 46 |
| Figure 4.17 | Magnetic field vs magnetization curve of $ZnFe_2O_4$ synthesized by microwave combustion method using urea and citric acid as fuel at room temperature..... | 48 |
| Figure 4.18 | FT-IR spectra of the $Zn_xNi_{1-x}Fe_2O_4$ nanoparticles with Zn contents of $x = 0.0, 0.2, 0.4, 0.6, 0.8$ and 1.0 synthesized by hydrothermal method..... | 50 |
| Figure 4.19 | Experimental and theoretically fitted XRD patterns of $(Zn_xNi_{1-x}Fe_2O_4)$ nanoparticles (from $x = 0$ to 1)..... | 52 |
| Figure 4.20 | Variation of lattice parameter a (filled circles) and oxygen positional parameter: u (circles) with respect to the Zn content in $Zn_xNi_{1-x}Fe_2O_4$ nanoparticles (from $x = 0$ to 1)..... | 56 |
| Figure 4.21 | (a) The TEM micrograph of $NiFe_2O_4$ nanoparticles synthesized by using PEG 400, (b) particle size distribution..... | 57 |
| Figure 4.22 | (a) The TEM micrograph of $Zn_{0.2}Ni_{0.8}Fe_2O_4$ nanoparticles synthesized by using PEG 400, (b) particle size distribution..... | 58 |
| Figure 4.23 | (a) The TEM micrograph of $Zn_{0.4}Ni_{0.6}Fe_2O_4$ nanoparticles synthesized by using PEG 400, (b) particle size distribution..... | 59 |
| Figure 4.24 | (a) The TEM micrograph of $Zn_{0.6}Ni_{0.4}Fe_2O_4$ nanoparticles synthesized by using PEG 400, (b) particle size distribution..... | 60 |
| Figure 4.25 | (a) The TEM micrograph of $Zn_{0.8}Ni_{0.2}Fe_2O_4$ nanoparticles synthesized by using PEG 400, (b) particle size distribution..... | 61 |
| Figure 4.26 | (a) The TEM micrograph of $ZnFe_2O_4$ nanoparticles synthesized by using PEG 400, (b) particle size distribution..... | 62 |
| Figure 4.27 | TEM micrographs of $Zn_xNi_{1-x}Fe_2O_4$ nanoparticles (a) $x = 0$; (b) 0.2 ; (c) 0.4 ; (d) 0.6 ; (e) 0.8 ; (f) 1.0 | 63 |
| Figure 4.28 | Histogram and log normal fits for $Zn_xNi_{1-x}Fe_2O_4$ nanoparticles (a) $x = 0$; (b) 0.2 ; (c) 0.4 ; (d) 0.6 ; (e) 0.8 ; (f) 1 | 64 |

| | |
|-------------|---|
| | |
| Figure 4.29 | Magnetic field vs magnetization curve of NiFe_2O_4 synthesized by hydrothermal method using PEG 400 as fuel at room temperature..... 66 |
| Figure 4.30 | Magnetic field vs magnetization curve of NiFe_2O_4 synthesized by hydrothermal method using PEG 400 as fuel at 10K..... 67 |
| Figure 4.31 | Magnetization vs temperature curve of NiFe_2O_4 synthesized by hydrothermal method using PEG 400 as surfactant..... 68 |
| Figure 4.32 | Magnetic field vs magnetization curve of $\text{Zn}_{0.2}\text{Ni}_{0.8}\text{Fe}_2\text{O}_4$ synthesized by hydrothermal method using PEG 400 as fuel at room temperature..... 69 |
| Figure 4.33 | Magnetic field vs magnetization curve of $\text{Zn}_{0.2}\text{Ni}_{0.8}\text{Fe}_2\text{O}_4$ synthesized by hydrothermal method using PEG 400 as surfactant at 10K..... 70 |
| Figure 4.34 | Magnetization vs temperature curve of $\text{Zn}_{0.2}\text{Ni}_{0.8}\text{Fe}_2\text{O}_4$ synthesized by hydrothermal method using PEG 400 as surfactant..... 71 |
| Figure 4.35 | Magnetic field vs magnetization curve of $\text{Zn}_{0.4}\text{Ni}_{0.6}\text{Fe}_2\text{O}_4$ synthesized by hydrothermal method using PEG 400 as surfactant at room temperature..... 72 |
| Figure 4.36 | Magnetic field vs magnetization curve of $\text{Zn}_{0.4}\text{Ni}_{0.6}\text{Fe}_2\text{O}_4$ synthesized by hydrothermal method using PEG 400 as surfactant at 10K..... 73 |
| Figure 4.37 | Magnetization vs temperature curve of $\text{Zn}_{0.4}\text{Ni}_{0.6}\text{Fe}_2\text{O}_4$ synthesized by hydrothermal method using PEG 400 as surfactant..... 74 |
| Figure 4.38 | Magnetic field vs magnetization curve of $\text{Zn}_{0.6}\text{Ni}_{0.4}\text{Fe}_2\text{O}_4$ synthesized by hydrothermal method using PEG 400 at room temperature..... 75 |

| | | |
|-------------|--|----|
| Figure 4.39 | Magnetic field vs magnetization curve of $Zn_{0.6}Ni_{0.4}Fe_2O_4$ synthesized by hydrothermal method using PEG 400 as surfactant at 10K temperature..... | 76 |
| Figure 4.40 | Magnetization vs temperature curve of $Zn_{0.6}Ni_{0.4}Fe_2O_4$ synthesized by hydrothermal method using PEG 400 as surfactant..... | 77 |
| Figure 4.41 | Magnetic field vs magnetization curve of $Zn_{0.8}Ni_{0.2}Fe_2O_4$ synthesized by hydrothermal method using PEG 400 as surfactant at room temperature..... | 78 |
| Figure 4.42 | Magnetic field vs magnetization curve of $Zn_{0.8}Ni_{0.2}Fe_2O_4$ synthesized by hydrothermal method using PEG 400 as surfactant at 10K temperature..... | 79 |
| Figure 4.43 | Magnetization vs temperature curve of $Zn_{0.8}Ni_{0.2}Fe_2O_4$ synthesized by hydrothermal method using PEG 400 as surfactant..... | 80 |
| Figure 4.44 | Magnetic field vs magnetization curve of $ZnFe_2O_4$ synthesized by hydrothermal method using PEG 400 as surfactant at room temperature..... | 81 |
| Figure 4.45 | Magnetic field vs magnetization curve of $ZnFe_2O_4$ synthesized by hydrothermal method using PEG 400 as surfactant at 10K temperature..... | 82 |
| Figure 4.46 | Magnetic hysteresis loops of $ZnFe_2O_4$ nanoparticles at different temperatures..... | 83 |
| Figure 4.47 | ZFC M-T curve of $ZnFe_2O_4$ nanoparticles with applied field of 20 Oe..... | 84 |
| Figure 4.48 | FC M-T curve of $ZnFe_2O_4$ nanoparticles with applied field of 1 kOe..... | 85 |
| Figure 4.49 | Zn content vs blocking temperature graph of $Zn_xNi_{1-x}Fe_2O_4$ | 86 |
| Figure 4.50 | M vs H curves at room temperature and their size weighted | |

| | | |
|-------------|--|----|
| | Langevien fits..... | 87 |
| Figure 4.51 | Magnetization vs Applied magnetic field curves of $Zn_xNi_{1-x}Fe_2O_4$ nanoparticles ($x =0$ to 1)..... | 90 |
| Figure 4.52 | Zn composition dependent H_c , M_r and M_s values of 10 K hysteresis curves..... | 91 |

LIST OF TABLES

| | | |
|-----------|--|----|
| Table 2.1 | Five different types of magnetic behaviour of matter..... | 8 |
| Table 2.2 | Some important minerals with the spinel structures..... | 16 |
| Table 3.1 | Stoichiometric amounts of metal nitrates (in gr) used in $Zn_xNi_{1-x}Fe_2O_4$ with microwave combustion method with citric acid..... | 20 |
| Table 3.2 | The compounds which has been synthesized by using citric acid as fuel and their particle sizes..... | 20 |
| Table 3.3 | Stoichiometric amounts of metal nitrates (in gr) used in $Zn_xNi_{1-x}Fe_2O_4$ with microwave combustion method with urea... | 21 |
| Table 3.4 | The compounds which has been synthesized by using urea as fuel and their particle sizes..... | 21 |
| Table 3.5 | Stoichiometric amounts of metal nitrates (in gr) used in $Zn_xNi_{1-x}Fe_2O_4$ with hydrothermal method with PEG 400..... | 23 |
| Table 3.6 | The compounds which has been synthesized by hydrothermal method by using PEG 400 as surfactant and their particle sizes.. | 23 |
| Table 4.1 | Average particle sizes of $Zn_xNi_{1-x}Fe_2O_4$ nanoparticles calculated by using Debye-Sherrer equation synthesized by microwave combustion method using citric acid as fuel..... | 31 |
| Table 4.2 | Average particle sizes $Zn_xNi_{1-x}Fe_2O_4$ nanoparticles calculated by using Debye-Sherrer equation synthesized by microwave combustion method using urea as fuel..... | 38 |
| Table 4.3 | Mean particle diameter and magnetic parameters with an applied magnetic field for $Zn_xNi_{1-x}Fe_2O_4$ nanoparticles | |

| | | |
|------------|--|----|
| | synthesized using citric acid as fuel at room temperature..... | 49 |
| Table 4.4 | Mean particle diameter and magnetic parameters with an applied magnetic field for $Zn_xNi_{1-x}Fe_2O_4$ nanoparticles synthesized using urea as fuel at room temperature..... | 49 |
| Table 4.5 | The obtained particle sizes of $Zn_xNi_{1-x}Fe_2O_4$ nanoparticles (from $x = 0$ to 1) for (a) Experimental data (by Debye-Scherrer), (b) XRD - profile fit..... | 52 |
| Table 4.6 | The values of XRD cation distribution in $Zn_xNi_{1-x}Fe_2O_4$ nanoparticles ($x = 0$ to 1)..... | 54 |
| Table 4.7 | The magnetic moment per unit formula from XRD and VSM for $Zn_xNi_{1-x}Fe_2O_4$ nanoparticles ($x = 0$ to 1)..... | 55 |
| Table 4.8 | The obtained particle sizes or size distributions of $Zn_xNi_{1-x}Fe_2O_4$ nanoparticles (from $x = 0$ to 1)..... | 64 |
| Table 4.9 | Mean particle diameter and magnetic parameters with an applied magnetic field of $Zn_xNi_{1-x}Fe_2O_4$ nanoparticles synthesized using PEG 400..... | 87 |
| Table 4.10 | Statistical median size (d_m), geometric standart deviation (s_m) and average diameter (D_m) of $Zn_xNi_{1-x}Fe_2O_4$ nanoparticles ($x = 0$ to 1) obtained from magnetization measurements..... | 89 |

LIST OF SYMBOLS AND ABBREVIATIONS

| | |
|---------|--|
| m | :Pole strengths |
| μ | :Magnetic moment or magnetic dipole moment of bar magnet |
| T | :Period |
| e | :Charge of Electron |
| g | :Gyromagnetic Ratio Constant |
| μ_B | :Bohr Magnetron |
| μ_0 | :Magnetic Permeability of Free Space |
| A | :Area |
| L | :Angular Momentum Vector |
| S | :Spin Vector |
| J | :Total Angular Momentum Vector ($J = L + S$) |
| M | :Magnetization Vector |
| M_s | :Saturation Magnetization |
| B | :Total Magnetic Field |
| B_0 | :Applied (external) Field |
| H | :Effective Magnetic Field |
| χ | :Magnetic Susceptibility |
| T_c | :Curie Temperature (Critical temperature) |
| T_N | :Neél Temperature |
| T_B | :Blocking temperature |
| C | :Curie constant |
| k | :Boltzman Constant |
| J | :Exchange Constant |

G :Magnetic Field Unit (cgs), Gauss
T :Magnetic Field Unit, Tesla
 M_r :Remenance
 H_c :Coercivity
a.u. :Arbitrary Unit
Oe :Magnetic Field Strength
emu/g : (Mass) magnetization, A·m²/kg in (SI)

CHAPTER 1

INTRODUCTION

Nanotechnology is understanding and control of matter at dimensions in 1-100 nm range, where this new view provides us many opportunities to investigate nature in nanoscale. Various applications especially in medicine, magnetic recording media, read-write head systems, medical diagnostics, information technology, information storage systems, defense industry and nanodevices which take us one step closer to new inventions through this research has been improved rapidly for a few years.

The changes in last decade showed many different and easy ways to produce nanoparticles of a variety of compositions for the synthesis with more control. However, many abilities and tools are improved to characterize and explore the physical properties of nanoparticles. The use of chemical nanoparticles from magnetic fluids to medical treatment of cancer increased by the increase in applications with various preparation and characterization techniques. Since chemical compositions yield producing different compounds, we can see an inevitable change in physical properties and internal structure. This change is the main reason to produce various grains which are expected to behave in a predicted frame.

Magnetic nano-composites are used for many purposes because of their microwave absorption advantages with design flexibility, low cost for preparation equipments, and other microwave properties over various kinds of chemical compounds. When the size is reduced to a few nanometers, particles change their behavior extremely.

The sensitivity of ferrites is well known for the manufacturing which explains their microstructurally dependent properties. When the size of ferrite particles change by controlling a doped metal in it, magnetic properties also change between different types

of magnetism above and below a certain temperature called blocking temperature. All of these possibilities come from spinel structure of ferrites [1,2].

Spinel ferrites (MFe_2O_4 , M:Co, Mg, Zn, Ni) have been investigated in recent years for their useful electrical and magnetic properties and applications in information storage systems, microwave absorbers, magnetic bulk cores, magnetic ferrofluids and refrigerants (like paramagnetic and intermetallic compounds) [3-7]. They crystallize in a spinel structure, in which both divalent and trivalent cations are distributed among tetrahedral (A) and octahedral (B) sites. The unit cell contains 32 O-atoms in a cubic structure with 8 tetrahedral and 16 octahedral occupied sites [8-10]. The site preference exhibited by divalent ions defines if the spinel is normal, inverse or mixed. In the “normal” structure, the divalent cations enter fourfold tetrahedral coordination, and ferric ions occupy the octahedral sites. In the “inverse” structure, much common in (Ni, Zn)-ferrites the A cations move to the octahedral sites and are replaced by half the Fe ions, the other half of Fe ions remain at the octahedral sites. In most cases, magnetic divalent cations (such as Ni^{2+}) prefer the octahedral sites and produce an inverse spinel structure. Diamagnetic divalent cations (such as Zn^{2+}) have preference for the tetrahedral positions and the resulting structure is a normal spinel [11, 12].

Due to their various technological applications, such as usages in electromagnetic devices operated in high frequencies with their high resistivities and low eddy current, Ni-Zn ferrites have attracted recently considerable research interest. Its high resistivity and low magnetic coercive field, supply excellent core material for power transformers in electronics, antenna rods, loading coils, and telecommunication devices.

The physical properties of nanoparticles are of current interest due to size-dependent behavior observed in nanometer length scale. Magnetic properties of (Ni, Zn)-ferrites are strongly depend on grain size and composition. It is necessary to take into account of heat treatments on the microstructure of some selected compositions of the Ni-Zn ferrite compounds in order to observe ferrite samples with expected behaviors [13, 14].

The magnetic order in ferrimagnetic spinels is based on a super exchange interaction mechanism that occurs between the metal ions in the A and B sublattices (or sites).

When we compare the effects of Ni and Zn ions, it is seen that there exists a possibility to vary magnetic properties of the fine particles [8, 13].

Generally the degree of changing ions in octahedral and tetrahedral sites is inversely proportional to the crystallite size. Synthesis method also plays a crucial role. Several techniques, e.g., coprecipitation, microwave combustion, ball milling, sol gel, and hydrothermal technique have been applied to synthesize nanosized ZnFe_2O_4 and NiFe_2O_4 with a partially inverted spinel structure [14-17].

Zinc ferrite (ZnFe_2O_4) has a continuous research interest due to its simple magnetic structure compared to other spinel ferrites [10, 12, 15]. In stable equilibrium it is paramagnetic and shows antiferromagnetic property below 10K Néel temperature. When we dope a metal which has higher ionic diameter, it has been proved that particle size increase. R. Arulmurugan et al. [16] proved that fine particles with higher zinc content are agglomerated less than 10 nm scales. It is also known that Zn promotes sintering, bringing an increase in grain size.

The fundamental difference in the heating mechanism of microwave synthesis offers unique advantages over conventional sintering processes [18]. In conventional heating, heat is generated by heating elements (in resistive heating) and then transferred to a sample via radiation, conduction and convection, which require a long duration for sintering materials that cause some of the constituents to evaporate, thereby modify the desired stoichiometry. In microwave synthesis, the materials absorb microwave energy themselves and then transform it into heat within the sample volume and sintering can be completed in shorter times. Major advantages of microwave processing are higher efficiency, enhanced reaction and sintering rate as well as shorter cycle times and cost savings [11]. This part of research selects urea and citric acid as fuels to confirm both the feasibility of our proposal and the applicability of using our organic compounds. $\text{Zn}_x\text{Ni}_{1-x}\text{Fe}_2\text{O}_4$ with the x ratios between 0.0, 0.2, 0.5, 0.7, 1.0 are synthesized both for urea and citric acid used as a fuel.

Hydrothermal method got a new influence to develop techniques for preparing ferrite particles in nanosize, which have quite different magnetic properties. Electrical and magnetic properties of cations in tetrahedral and octahedral sites depend

distribution in the chemical composition, where equilibrium configuration changes in bulk and nanophase [19-23] . According to these behaviors of ions, hydrothermal method is found to be very effective to prepare nanophase ferrites in a controlled process of synthesis [6, 24-29]. The process parameters such as pH of solution, temperature of mixed compounds, are widely known to act the purity, narrow size particle distribution, surface morphology, high crystallinity and fewer defects. Also use of surfactant (such as PEG 400) affects the size and magnetic properties of spinel ferrites [28, 30]. Therefore we have used surfactants to investigate affects of size and magnetic properties of $Zn_xNi_{1-x}Fe_2O_4$ nanoparticles.

$Zn_xNi_{1-x}Fe_2O_4$ with $x = 0.0, x = 0.2, x = 0.4, x = 0.6, x = 0.8, x = 1.0$ ratios for hydrothermal method and $x = 0.0, x = 0.2, x = 0.5, x = 0.7, x = 1.0$ for microwave combustion method have been studied. Structural and magnetic characterization has been considered. FT-IR and XRD are used to identify desired chemical compounds and vibrating sample magnetometer (VSM) has been used for magnetizatic characterization of products. Results are evaluated to understand the magnetic behavior of $Zn_xNi_{1-x}Fe_2O_4$ with different synthesis methods and fuels.

CHAPTER 2

THEORY OF MAGNETISM

2.1 MAGNETIZATION AND MAGNETIC FIELD

Substances placed near a magnetizing force are affected by it, and shows some magnetic properties [31]. If a substance has magnetic moments, it is possible to mention about a quantity which describes an internal property of it. The net magnetic moment per unit volume is defined as *magnetization*. Magnetization is a vector quantity and symbolized as \vec{M} with the mathematical definition below in eqn. 2.1:

$$\vec{M} = \frac{\vec{\mu}}{V} \quad (2.1)$$

The amount of magnetism is introduced for a body by a magnetizing force \mathbf{H} and flux density \mathbf{B} . The amount of the flux density (\mathbf{B}) is effected by the intensity of the magnetizing force \mathbf{H} , the properties of the substance, and by the mixture of media between the systems. The total amount of flux per area is given by

$$\Phi = \vec{B} \cdot \vec{A} \quad B = \frac{\Phi}{A} \quad \left(T = \frac{Wb}{m^2} \right) \quad \text{in (SI)}$$
$$\left(G = \frac{Mx}{cm^2} \right) \quad \text{in (CGS)} \quad (2.2)$$

The unit of \mathbf{B} is Tesla (T) in SI unit system (weber per meter – square) , and Gauss (G) in CGS unit system (maxwell per centimeter – square).

$$1T = 10^4 G \quad \text{and} \quad 1Wb = 10^8 Mx \quad (2.3)$$

Magnetic flux density \vec{B} and magnetic field strength \vec{H} are linearly related by

$$\vec{B} = \mu_0 \vec{H} \quad (2.4)$$

If we want to consider total magnetic field of a substance, two terms join the magnetic field expression; one of them is B_0 which is produced by a current carrying conductor. And the second one is external magnetic field B_m which produced by the magnetic substance. Thus total magnetic field is:

$$\vec{B} = \vec{B}_0 + \vec{B}_m = \vec{B}_0 + \mu_0 \vec{M} \quad (2.5)$$

Magnetization can be expressed in a special way which is linearly related to magnetic field \mathbf{H} . So

$$\vec{M} = \chi \vec{H} \quad (2.6)$$

χ is defined as magnetic susceptibility, it is a dimensionless quantity. If we want to write \vec{B} in terms of magnetic susceptibility and field, we get

$$\vec{B} = \mu_0 (1 + \chi) \vec{H} = \mu_0 \mu_r \vec{H} \quad (2.7)$$

where $\mu_r = 1 + \chi$ is given as the relative permeability of the substance. χ and μ_r are basic parameters and help us to distinguish various magnetic behaviours of the substances.

- a) Empty space $\chi = 0$, because there is no matter to magnetize so, $\mu_r = 1$
- b) Diamagnetic material: χ is small and negative, and μ_r is slightly less than 1

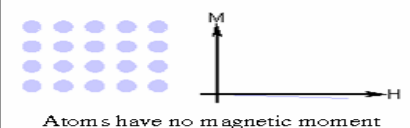

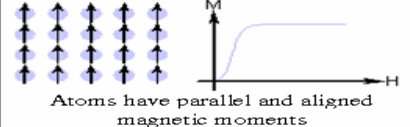
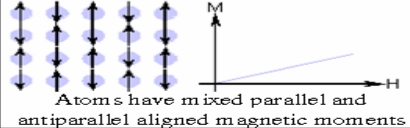
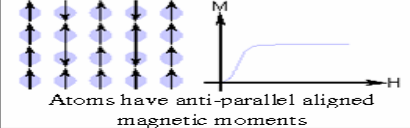
- c) Paramagnetic and antiferromagnetic: χ is small and positive, and μ_r is slightly greater than 1
- d) Ferromagnetic and ferrimagnetic: χ and μ_r are large and positive.

2.2 CLASSIFICATION OF MAGNETIC MATERIALS AND TYPES OF MAGNETISM

All materials can be classified in terms of their magnetic behavior falling into one of five categories depending on their responses to an externally applied magnetic field. The two most common types of magnetism are diamagnetism and paramagnetism, which account for the magnetic properties of most of the periodic table of elements at room temperature. And most useful ones are ferromagnetic materials.

Diamagnetic and paramagnetic elements are usually referred to as non-magnetic, whereas those are referred to as magnetic actually classified as ferromagnetic. The only other type of magnetism observed in pure elements at room temperature is antiferromagnetism. Magnetic materials can also be classified as ferrimagnetic however this is not observed in any pure element but can only be found in compounds, such as spinels, mixed oxides, ferrites, from which the name “ferrimagnetism” comes from. The value of magnetic susceptibility is denoted in a particular range for each type of material and this is shown in Table 2.1 with some examples.

Table 2.1 Five different types of magnetic behaviour of matter [32].

| Type of Magnetism | Atomic Behaviour | Example Susceptibility |
|--------------------|--|--|
| Diamagnetism |  <p>Atoms have no magnetic moment</p> | Au: -2.74×10^{-6} Cu: -0.77×10^{-6} |
| Paramagnetism |  <p>Atoms have randomly oriented magnetic moments</p> | β -Sn : 0.19×10^{-6} Pt : 21.04×10^{-6} Mn: 66.10×10^{-6} |
| Ferromagnetism |  <p>Atoms have parallel and aligned magnetic moments</p> | Fe ~ 100,000 |
| Antiferromagnetism |  <p>Atoms have mixed parallel and antiparallel aligned magnetic moments</p> | Cr : $3,6 \times 10^{-6}$ |
| Ferrimagnetism |  <p>Atoms have anti-parallel aligned magnetic moments</p> | Ba Ferrite ~ 3 |

All materials have some magnetic moments inside their atoms. When an external magnetic field is applied, some of them are influenced and some of them do not show any response. If a substance doesn't show any magnetization both in the presence or absence of magnetic field, these kind of materials are said to be diamagnetic. Inherently, default responses of materials in a magnetic field are diamagnetic but when we apply some external field, we expect that they will have a change in their magnetic moments and supply us a residual magnetic property. But diamagnetic materials never have a tendency to achieve that of ability like a magnet. Their susceptibilities are negative as it can be seen for Au and Cu in Table 2.1.

A material which have permanent magnetic moments is defined as paramagnetic. When a magnetic field is applied, magnetic moments don't align perfectly and they have a positive susceptibility in the range of 10^{-5} to 10^{-3} . If a small fraction of the atoms are aligned with the field (30 % or less), then the magnetization obeys Curie's Law, [33]

$$\vec{M} = \chi \vec{H}_{ext} \quad (\text{from 2.6})$$

$$\vec{M} = C \frac{\vec{H}_{ext}}{T} \quad \text{and} \quad \chi = \frac{C}{T} \quad (2.7)$$

where C is constant (different for each different material), \mathbf{H}_{ext} is the applied field and T is the temperature in kelvin. Curie's Law says that if \mathbf{H}_{ext} is increased, the magnetization increases. That means stronger magnetic field helps more magnetic moments to align. And magnetization is inversely proportional to the temperature. An increase in thermal activity prevents the alignment of dipoles. When the aligned fraction of dipoles becomes larger and closes to %100, then magnetization doesn't change with temperature. Because all of the dipoles are aligned and there won't be any change in susceptibility and magnetization even if you increase applied field. As a result, when a paramagnetic substance located inside a strong magnetic field, it becomes a magnet relative to applying time of magnetic field. When \mathbf{H}_{ext} is removed, then magnetization is no longer available.

Ferromagnetism is the most common type of magnetism where we are familiar some substances in (iron, nickel, cobalt). Ferromagnetic materials have a long-range order in their atomic structure which causes the unpaired electron spins to align parallel to each other in a region called “domain”. In the presence of a magnetic field, all magnetic moments are aligned and magnetic susceptibility is high. If magnetic field is removed, dipoles retain their magnetization. We can get all these informations by analyzing the hysteresis loop. That's way it is possible to determine saturation magnetization (M_S) and remanent magnetization (M_R). Ferromagnetic materials are mostly used in magnetic recording medias, storage systems, information technology, defense industry and medical treatments and applications.

In antiferromagnetic materials, the magnetic momenta of electrons align in a regular pattern with neighboring spins in opposite directions. This is a different type of magnetism called antiferromagnetism. Generally it is observed at low temperatures where magnetic moments of atoms are observed in a disordered alignment above a critical temperature (or transition temperature) which is called as Néel temperature. Below T_N the two sublattices of an antiferromagnet spontaneously get magnetised in the same way as a ferromagnet but the net magnetisation is zero due to the opposite orientation of the magnetic moments. They show paramagnetic behavior above the Néel

temperature. It is usually observed at low temperature in diamagnetic properties. Antiferromagnets can also be considered with ferromagnetic materials with a mechanism called as exchange anisotropy. In an aligning inside a magnetic field, it causes the surface atoms of the ferromagnet to align with the surface atoms of the antiferromagnet. This provides an ability to "pin" the orientation of a ferromagnetic film, which is the one of the main uses in magnetic sensors including modern hard drive write-read heads.

In ferrimagnetic materials the magnetic ions are located on two magnetic sublattices of oppositely directed spins and magnetic moments like in antiferromagnetism. But despite this similarity, the magnetic moments of the two sublattices in a ferrimagnetic material are exactly opposite in direction and magnitude. Thus they don't compensate each other. Magnetic sublattices are constructed, which have a ferromagnetic character separately. That's way M_s arises as the difference between these sublattice magnetizations. The number of ions on the different sites does not need to be equal and variation of M_s with temperature and they may rise in certain ranges. The most typical ferrites are the spinel ferrites (Fe_3O_4), magnetic garnets, and certain rare earth-transition metal alloys [33].

2.3 THE HYSTERESIS LOOP AND MAGNETIC PROPERTIES

Much information about magnetic properties of a substance can be obtained by analyzing its hysteresis loop. A hysteresis loop shows the relation between magnetic flux density \mathbf{B} and magnetic field strength \mathbf{H} . It is also called as B-H loop.

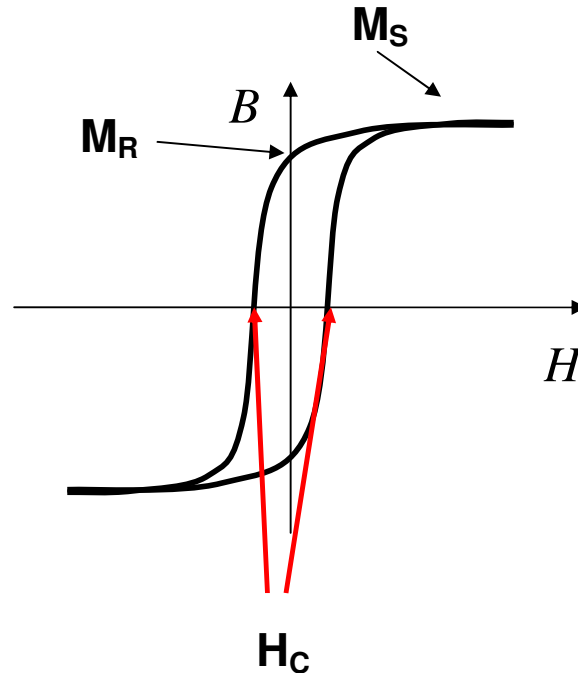


Figure 2.6 Hysteresis loop sample for a ferromagnet

Fig. 2.6 shows a hysteresis loop in more details. The loop is generated by changing magnetic flux density \mathbf{B} with magnetic field strength \mathbf{H} . A ferromagnetic material follows these lines when it is located in a magnetic field. As the line demonstrates, the greater the amount of applied magnetic field \mathbf{H} , creates stronger magnetic field on the component \mathbf{B} . When the line becomes parallel to the x axis, almost all of the magnetic domains are aligned and an additional increase in the magnetizing force will produce very little increase in \mathbf{B} . Then it is said that the material has reached the point of magnetic saturation described by \mathbf{M}_S in Fig. 2.6 . When \mathbf{H} is reduced to zero, an inductive coercive force will arise to move the curve from saturation point to origin. Now an amount of magnetic flux remains in the material even though the magnetizing force is zero. This is referred to the point of remenence and indicates the level of residual magnetism in the material. It is shown as \mathbf{M}_R on the Fig. 2.6 .In remenence situation some of the magnetic domains remain aligned but some have lost their alignment. As the magnetizing force is reversed, the curve behaves same. Just its direction changes and creates \mathbf{M}_R and \mathbf{M}_S again for negative magnetic flux axis.

1. **Retentivity** – An amount of the residual flux density corresponding to the saturation point of a magnetic material. Also it is material's ability to retain a

certain amount of residual magnetic field when the magnetizing force is removed after saturation.

2. **Remanent Magnetism** – Amount of magnetic flux density that remains in a material when the magnetizing force is zero. Note that residual magnetism and retentivity are the same when the material has been magnetized to the saturation point. However, the level of residual magnetism may be lower than the retentivity value when the magnetizing force did not reach the saturation level.
3. **Coercive Force** - The amount of reverse magnetic field which must be applied to a magnetic material to make the magnetic flux return to zero.

2.4 THEORY OF SUPERPARAMAGNETISM AND PARAMAGNETISM

Superparamagnetism is a phenomenon in which magnetic materials may exhibit a different behavior similar to paramagnetism. At temperatures below the Curie or the Neel temperature superparamagnetism is observed.

This temperature can be used to determine the structural or magnetic properties of substances below or above the critical point, called Curie temperature. Usually, coupling forces in ferromagnetic materials cause the magnetic moments of neighboring atoms to align, resulting in very large internal magnetic field. At temperatures above the Curie temperature, the thermal energy is dominant to overcome the coupling forces. So that it causes the atomic magnetic moments to fluctuate randomly. If there is no longer any magnetic order, the internal magnetic field no longer exists and the material exhibits paramagnetic behavior.

Superparamagnetism is observed when the material size is in the interval of very small dimensions around 10 nm. McNab et al. showed that there was no stable magnetization in 10-16 nm range for a magnetite [34]. The significant point here is the thermal energy is not sufficient to align the coupling forces between neighboring atoms in this scale. In this case temperature fluctuations should change the entire magnetization of the crystallite by causing average magnetic field to zero where as the temperature is below the Curie or Neel temperature. If the crystallite sizes are so small then the thermal energy fluctuations can overcome the anisotropy energy and change

the direction of the magnetization of a particle from one easy axis to another, where superparamagnetic relaxation is observed in. Relaxation is a time interval in which magnetic moments need to align their initial position. And that time is given by [35] :

$$\tau = \tau_0 \exp\left(\frac{KV}{k_B T}\right) \quad (2.8)$$

The energy required to change the direction of magnetization of a crystallite is called the Crystalline anisotropy energy and depends both on the material properties and the crystallite size. The term “K” in eqn. 2.8 is anisotropy constant and V is the volume. So KV describes magnetic anisotropy energy and $k_B T$ describes thermal energy.

As the crystalline size decreases, then Crystalline anisotropy energy decreases, resulting in a decrease in the temperature at which superparamagnetism observed in the material [36-38].

Hysteresis curves are usually obtained in “s” shape form and saturation magnetizations did not attain saturation. Despite ferromagnetic materials, superparamagnetic materials have tiny coercive field and a magnetization curve increase rapidly up to remenence point (M_s) and after this point it follows linearly as the magnetic field increases.

Paramagnetism is another form of magnetism and it differs a little from diamagnetism because of atoms have permanent magnetic moments in that substances. When a magnetic field is applied, the dipole moments try to align with the magnetic field. So the susceptibility of a paramagnetic material is positive. If magnetic field is removed, it is well known that magnetization becomes zero in paramagnetic materials.

2.5 THE SPINEL STRUCTURE AND FERRITES

Tetrahedral and octahedral sites in an atomic structure can be occupied by other atoms or ions in crystal structures of salts and alloys. Thus, recognizing their existence and their geometrical constraints can identify its crystal structure. If we put four (4) spheres together touching each other, arrangement of spheres is **tetrahedral** and the space in the center is called a **tetrahedral site**. These sites are also called **holes** in some literature. The **octahedral site** is formed by six spheres. Both structures are shown in the diagrams below in Fig.2.7

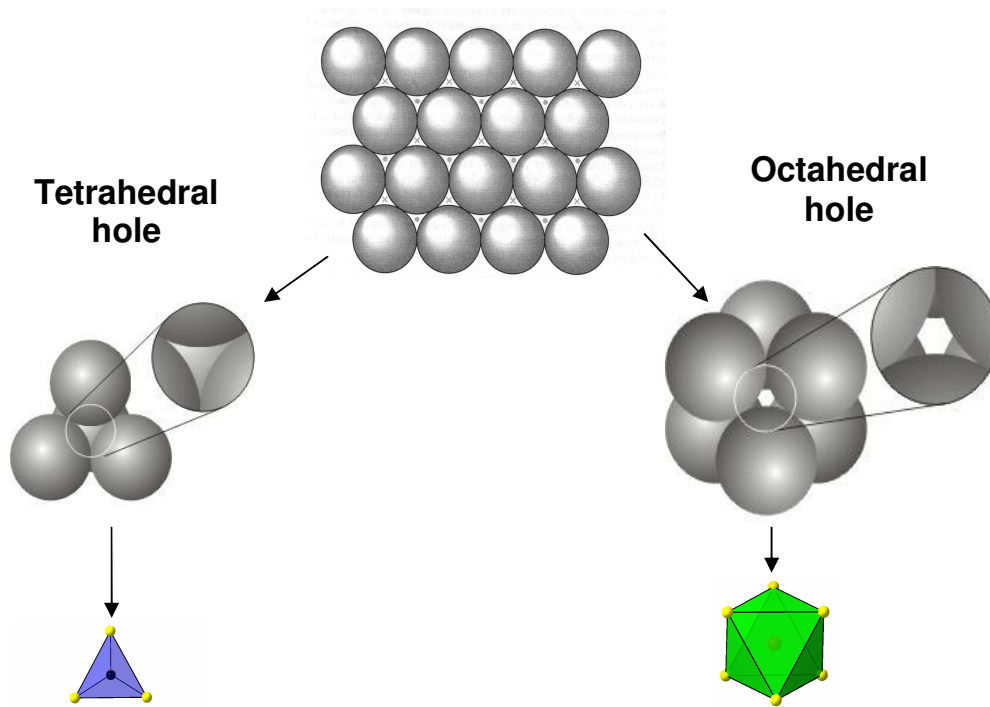


Figure 2.7 Tetrahedral and octahedral sites in a crystal structure.

The spinels group of minerals has a general formula AB_2O_4 , where A is a divalent ion (e.g. Mg^{2+}) and B is a trivalent ion (e.g. Al^{3+}). The oxygen atoms are cubic close-packed and the A and B ions occupy both tetrahedral and octahedral positions.

The way in which the interstitial sites are occupied means that the unit cell of spinel is 2 x 2 x 2 times larger than the cubic unit cell of the oxygen close-packed structure.

Therefore there are 32 oxygen atoms in the unit cell of spinel. The total number of interstitial sites in the unit cell is therefore 32 octahedral sites and 64 tetrahedral sites. The contents of the unit cell are $A_8B_{16}O_{32}$ and it is clear that relatively few of the total number of interstitial sites are occupied.

The 8 tetrahedral sites are positioned at fixed symmetry points with coordinates of the form $(1/8, 1/8, 1/8)$.

The 16 octahedral sites are positioned at fixed symmetry points with coordinates of the form $(1/2, 1/2, 1/2)$.

There are two types of spinel structures: *normal spinels* and *inverse spinels*

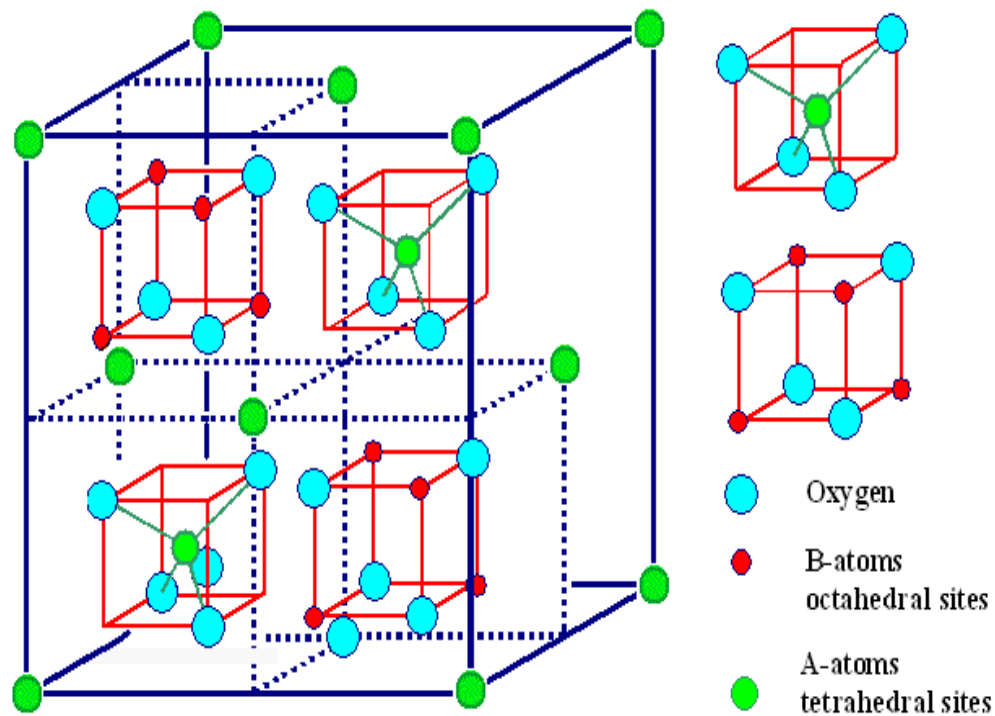


Figure 2.8 Crystal structure of spinel [39].

The spinel structure is also called *normal spinel structure*, where X cations occupy the tetrahedral sites of the oxide lattice, and Y cations the octahedral sites. In normal spinels, the 8 A cations occupy 8 tetrahedral sites and the 16 B cations occupy 16 octahedral sites. It can be written as an example [40]:



In the case of an *inverse spinel*, 8 of the B cations occupy the 8 tetrahedral sites, while 8 A cations and 8 B cations are distributed over the 16 occupied octahedral sites.

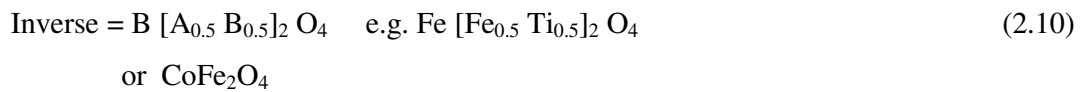


Table 2.2 : Some important minerals with the spinel structures

| Name of Mineral | Chemical Formula | Cation Distribution |
|-----------------|---------------------------|--|
| magnetite | Fe_3O_4 | $\text{Fe}^{3+}[\text{Fe}^{2+}, \text{Fe}^{3+}]\text{O}_4$ |
| chromite | FeCr_2O_4 | $\text{Fe}^{2+}[\text{Cr}^{3+}]_2\text{O}_4$ |
| spinel | MgAl_2O_4 | $\text{Mg}^{2+}[\text{Al}^{3+}]\text{O}_4$ |
| ulvöspinel | Fe_2TiO_4 | $\text{Fe}^{2+}[\text{Fe}^{2+}, \text{Ti}^{4+}]\text{O}_4$ |

Some of important minerals, their chemical formulas and cation distributions are given in Table 2.2

Ferrites are a class of spinels, materials that adopt a crystal motif consisting of cubic close-packed (FCC) oxides (O^{2-}) with A cations occupying one eighth of the octahedral holes and B cations occupying half of the octahedral holes. The magnetic material known as "ZnFe" has the deceptively simple formula ZnFe_2O_4 , with Fe^{3+} occupying the octahedral sites and half of the tetrahedral sites. The remaining tetrahedral sites in this spinel are occupied by Zn^{2+} .

There are two types of ferrites: *Soft ferrites* and *hard ferrites*.

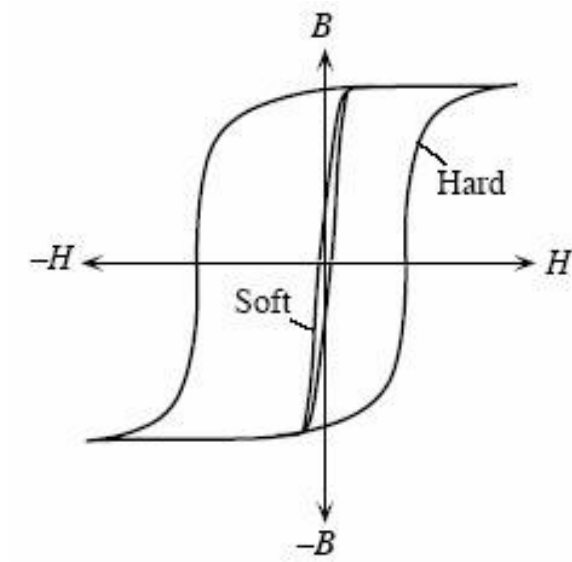


Figure 2.9 The coercivity of soft ferrites and hard ferrites

The M-H curve behavior of soft ferrites and hard ferrites are shown in Fig. 2.9. Soft ferrites are used in transformer or electromagnetic cores contain nickel, zinc, or manganese compounds. They have low losses at high frequencies and extensively used in the cores of power supplies and RF transformers and inductors where as hard ferrites have the most usages in magnets in radios because of their permanent magnetization and large coercivity [41].

CHAPTER 3

EXPERIMENTAL AND CHARACTERIZATION

3.1 SYNTHESIS METHODS

Our $Zn_xNi_{1-x}Fe_2O_4$ samples have been synthesized by two different synthesis methods: Microwave combustion synthesis and hydrothermal synthesis. In microwave synthesis citric acid and urea have been used as fuel. For hydrothermal method, PEG 400 (Polyethylene Glycol 400) has been used as surfactant. As a result, $Zn_xNi_{1-x}Fe_2O_4$ has three types of variations as it can be seen in Fig.3.1.

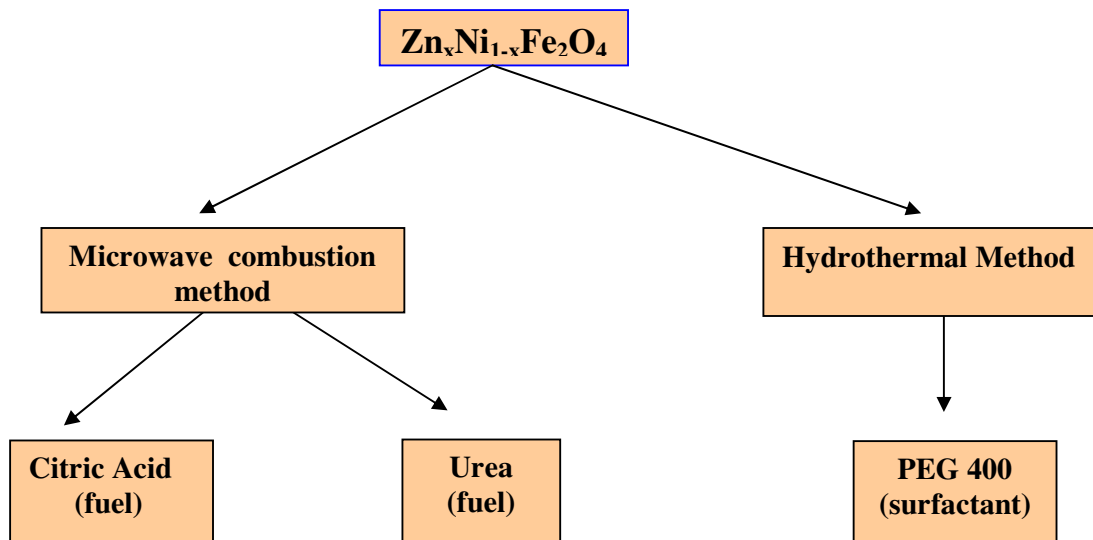


Figure 3.1 Synthesis outline of our samples.

3.1.1 Microwave Combustion Method

$Zn_xNi_{1-x}Fe_2O_4$ has been synthesized with different Zn ratios of $x = 0.0$, $x = 0.2$, $x = 0.5$, $x = 0.7$, $x = 1.0$ by using urea and citric acid. $Zn(NO_3)_2 \cdot 6H_2O$, $Ni(NO_3)_2 \cdot 6H_2O$, $Fe(NO_3)_3 \cdot 9H_2O$, $(NH_2)_2CO$ (Urea), and $C_6H_8O_7$ (Citric acid) are used as chemicals. Citric acid and urea are used as fuel to ignite samples for combustion method.

All of these chemicals are mixed in a crucible and heated in a microwave oven at $150^\circ C$ for 5 min. Luminous flame and smoke gas arised (Fig 3.2) following the ignition of mixture [42]. Finally, the powder sample has been picked from the bottom of the crucible. According to the humidity of the sample, it has been put into oven for drying.

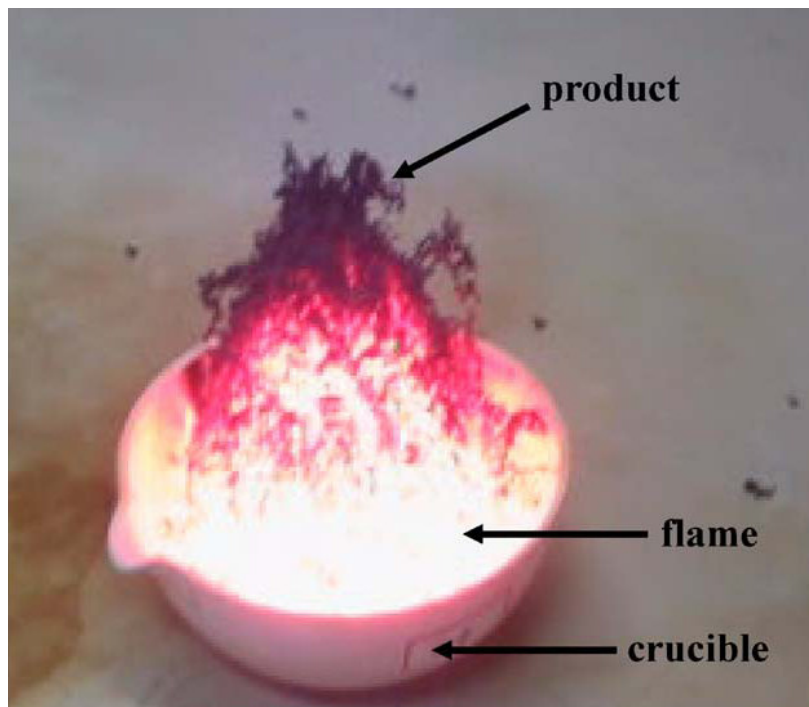


Figure 3.2 Combustion reaction of $Zn_xNi_{1-x}Fe_2O_4$ nanoparticles.

Citric Acid as Fuel:

The expected chemical reaction for the $Zn_xNi_{1-x}Fe_2O_4$ nanoparticles for $x = 0.0 - 1.0$ for citric acid is given below. Stoichiometric amounts of chemicals used during synthesis process are shown in Table 3.1. Synthesized samples and their particle sizes are given in Table 3.2.

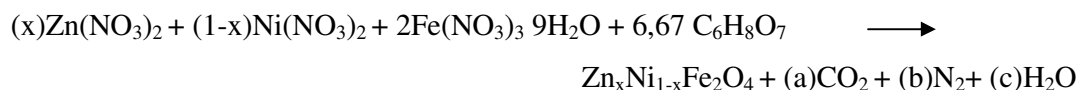


Table 3.1 Stoichiometric amounts of metal nitrates (in gr) used in $Zn_xNi_{1-x}Fe_2O_4$ with microwave combustion method with citric acid.

| Zn (mol) | Ni (mol) | 2Fe(NO ₃) ₃ | Citric Acid | Compound |
|----------|----------|------------------------------------|-------------|--|
| 0,298 | 0 | 0,808 | 1,28 | ZnFe ₂ O ₄ |
| 0,209 | 0,087 | 0,808 | 1,28 | Zn _{0,7} Ni _{0,3} Fe ₂ O ₄ |
| 0,149 | 0,146 | 0,808 | 1,28 | Zn _{0,5} Ni _{0,5} Fe ₂ O ₄ |
| 0,06 | 0,233 | 0,808 | 1,28 | Zn _{0,2} Ni _{0,8} Fe ₂ O ₄ |
| 0 | 0,291 | 0,808 | 1,28 | NiFe ₂ O ₄ |

Table 3.2 The compounds which has been synthesized by using citric acid as fuel and their particle sizes.

| Compounds | Crystallite Size (nm) (by Debye-Scherrer) |
|--|--|
| NiFe ₂ O ₄ | 19.07 |
| Zn _{0,2} Ni _{0,8} Fe ₂ O ₄ | 27.56 |
| Zn _{0,5} Ni _{0,5} Fe ₂ O ₄ | 24.24 |
| Zn _{0,7} Ni _{0,3} Fe ₂ O ₄ | 30.56 |
| ZnFe ₂ O ₄ | 29.94 |

Urea as Fuel:

The expected chemical reaction for the $Zn_xNi_{1-x}Fe_2O_4$ nanoparticles for $x = 0.0 - 1.0$ for urea is given below. Stoichiometric amounts of chemicals used during synthesis process are shown in Table 3.3. In the following, synthesized samples and their particle sizes are given in Table 3.4.

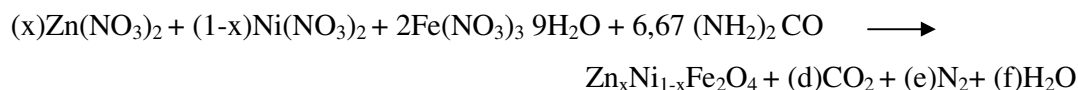


Table 3.3 Stoichiometric amounts of metal nitrates (in gr) used in $Zn_xNi_{1-x}Fe_2O_4$ with microwave combustion method with urea.

| Zn (mol) | Ni (mol) | 2Fe(NO ₃) ₃ | Urea | Compound |
|----------|----------|------------------------------------|------|--|
| 0,298 | 0 | 0,808 | 0,4 | ZnFe ₂ O ₄ |
| 0,209 | 0,087 | 0,808 | 0,4 | Zn _{0,7} Ni _{0,3} Fe ₂ O ₄ |
| 0,149 | 0,146 | 0,808 | 0,4 | Zn _{0,5} Ni _{0,5} Fe ₂ O ₄ |
| 0,06 | 0,233 | 0,808 | 0,4 | Zn _{0,2} Ni _{0,8} Fe ₂ O ₄ |
| 0 | 0,291 | 0,808 | 0,4 | NiFe ₂ O ₄ |

Table 3.4 The compounds which has been synthesized by using urea as fuel and their particle sizes.

| Compounds | Crystallite Size (nm) (by Debye-Scherrer) |
|--|--|
| NiFe ₂ O ₄ | 34.92 |
| Zn _{0,2} Ni _{0,8} Fe ₂ O ₄ | 24.44 |
| Zn _{0,5} Ni _{0,5} Fe ₂ O ₄ | 22.67 |
| Zn _{0,7} Ni _{0,3} Fe ₂ O ₄ | 25.55 |
| ZnFe ₂ O ₄ | 24.25 |

3.1.2 HYDROTHERMAL METHOD

The chemical compounds have been prepared and mixed. The prepared compounds for $Zn_xNi_{1-x}Fe_2O_4$ have been put in a pH container with a volume of 5.5ml. NaOH solution has been added to set the pH to 11 in an autoclave (showed in Fig. 3.3). 15mg PEG 400 (Polyethylene Glycol 400) has been added. And another 10 mg PEG 400 has been added, after a while. The $Zn_{0.4}Ni_{0.6}Fe_2O_4$ sample has been synthesized to test and PEG 400 amount in this sample was 30 g. In other samples total PEG was 25g. 10ml alcohol has been added. Prepared solution has been put in to an oven at $150^\circ C$ for 21h. Powder inside a wet filter was taken out to dry at the room temperature spontaneously. Then powder has been put in the oven again to provide the vaporization. Substance has been filtered by adding alcohol.

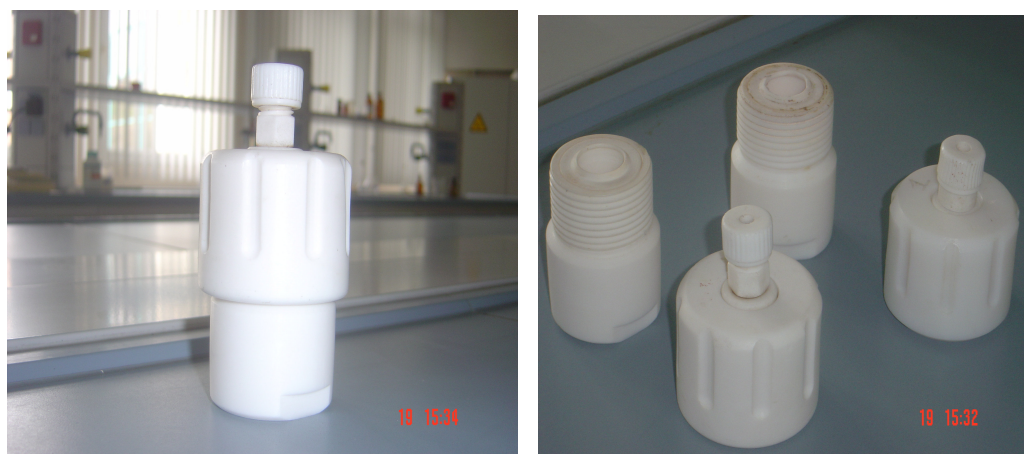


Figure 3.3 Autoclaves used for hydrothermal synthesis.

PEG 400 as Surfactant:

The expected chemical reaction for the $Zn_xNi_{1-x}Fe_2O_4$ nanoparticles for $x = 0.0 - 1.0$ for PEG 400 is given below. The stoichiometric amounts of chemicals used during

synthesis process are shown in Table 3.5 and particle sizes of samples are given in the following, Table 3.6.

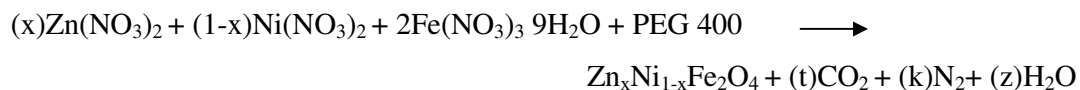


Table 3.5 Stoichiometric amounts of metal nitrates (in gr) used in $\text{Zn}_x\text{Ni}_{1-x}\text{Fe}_2\text{O}_4$ with hydrothermal method with PEG 400.

| Zn (mol) | Ni (mol) | 2Fe(NO ₃) ₃ | PEG 400 | Compound |
|----------|----------|------------------------------------|---------|--|
| 0,298 | 0 | 0,808 | 25 | ZnFe ₂ O ₄ |
| 0,95 | 0,233 | 3,232 | 25 | Zn _{0,8} Ni _{0,2} Fe ₂ O ₄ |
| 0,535 | 0,349 | 2,424 | 25 | Zn _{0,6} Ni _{0,4} Fe ₂ O ₄ |
| 1,2 | 1,75 | 8,08 | 30 | Zn _{0,4} Ni _{0,6} Fe ₂ O ₄ |
| 0,059 | 0,233 | 0,808 | 25 | Zn _{0,2} Ni _{0,8} Fe ₂ O ₄ |
| 0 | 2,91 | 8,08 | 25 | NiFe ₂ O ₄ |

Table 3.6 The compounds which has been synthesized by hydrothermal method by using PEG 400 as surfactant and their particle sizes.

| Compounds | Crystallite Size (nm) (by Debye-Scherrer) |
|--|--|
| NiFe ₂ O ₄ | 30.03 |
| Zn _{0,2} Ni _{0,8} Fe ₂ O ₄ | 28.38 |
| Zn _{0,4} Ni _{0,6} Fe ₂ O ₄ | 13.20 |
| Zn _{0,6} Ni _{0,4} Fe ₂ O ₄ | 14.00 |
| Zn _{0,8} Ni _{0,2} Fe ₂ O ₄ | 11.42 |
| ZnFe ₂ O ₄ | 14.35 |

3.2 CHARACTERIZATION TECHNIQUES

In this study, FT-IR (Fourier Transform Infrared Spectroscopy), X-ray Diffraction (XRD), and Transmission Electron Microscopy (TEM) measurements are used to determine the molecular structure for chemical compounds. Vibrating Sample Magnetometer (VSM) is used for the magnetic characterization of the samples.

3.2.1 Fourier Transform Infrared Spectroscopy (FT-IR)

FT-IR transmission spectra were used to study chemical structure changes. All measurements have been taken on Mattson Satellite Infrared Spectrometer in the range of 4000 to 400 cm^{-1} . Microwave method; by using *urea* and *citric acid* as fuel and hydrothermal method with PEG 400 (Polyethylene Glycol 400) as a surfactant have been used in synthesis processes.

3.2.2 X-RAY Powder Diffractometry (XRD)

Various information can be derived from X-ray Diffraction (XRD) measurements which provides many hints from the position and shape of the lines, one can obtain the unit cell parameters and microstructural parameters (grain size, microstrain, etc.) respectively.

Diffraction of Waves by Crystals (Bragg's Law) : When the wavelength of the incident radiation to a sample is comparable or smaller with lattice constant, we may find diffracted beams in directions quite different from the incident direction. W.L. Bragg presented a simple explanation (eqn. 3.1) of the diffracted beams from a crystal [43].

The relationship between reflection angle θ , wavelength λ and path difference is given by

$$2d\sin\theta = n\lambda \quad (3.1)$$

where n is an integral number n of wavelengths λ . The reflection of incident beam is only allowed for certain values of theta. To evaluate a deeper analysis from the basis of atoms, we need to describe spatial distribution of electrons within each cell. This is required for identifying crystal structure with the "long range order" property. To do so, the unit cells must repeat themselves for a distance of \vec{r} .

$$n(\vec{r} + \vec{T}) = n(\vec{r}) \quad (3.2)$$

As we have repeated unit cells in a crystal, we can see their projection by exposing those X-ray beams. And by the help of Fourier analysis, it is possible to see that reflection patterns correspond reciprocal lattice vectors in a theoretical based lattice which are consistent with the Fourier constants.

Standard θ - 2θ Scans: The geometry of the XRD measurements is depicted in Fig. 3.4. An X-ray beam impinges on a sample and the intensity of the scattered beam is measured. In order to determine the lattice parameter and the average grain size in our samples we have performed standard θ - 2θ scans. The parameters of the diffraction line: position and width were obtained using Origin, Miniflex and Matlab.

Consequently we have assigned the entire broadening of the experimental line to the effect due to the specimen. Usually the lines could be fitted with Lorentzian functions, suggesting that the main contribution to the line-width is due to the reduced size of the crystallites. Under these conditions the observed profile was fitted with a convolution of the emission profile of the Cu- K_α radiation.

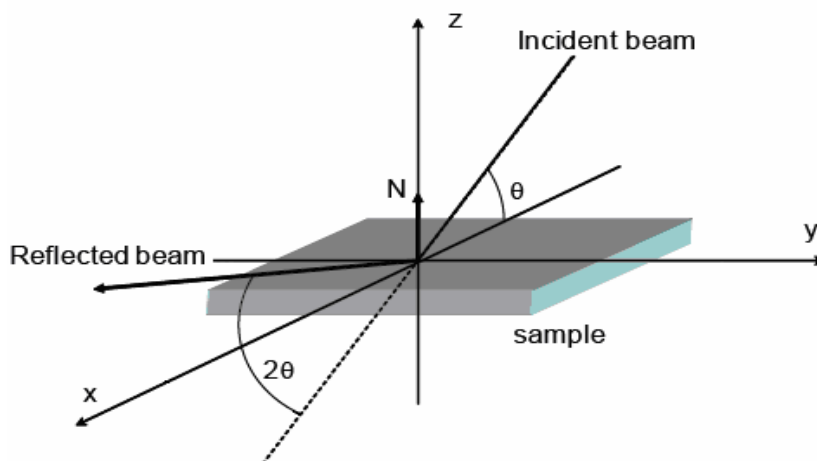


Figure 3.4 Sample in Cartesian coordinate system and specific angles for XRD measurements.

The X-Ray powder diffraction (XRD) patterns of the samples were recorded on a Rigaku Diffractometer using Cu-K α radiation ($\lambda = 1.54059 \text{ \AA}$). Standard scans were carried out in 0.02 step size in the range of 10^0 - 90^0 . The average crystallite size (D_{XRD}) of the nanocrystalline samples was calculated from the X-Ray FWHM (full width half maximum) line broadening analyses using the Debye – Scherrer formula in eqn. 3.3,

$$D_{XRD} = \frac{0.89\lambda}{\Delta\omega \cos\theta} \quad (3.3)$$

where λ is wavelength of the X-Ray used in \AA unit, $\Delta\omega$ is FWHM given by radians in the 2θ scale, θ is the Bragg angle and D_{XRD} is crystallite size in nm.

3.2.3 Transmission Electron Microscopy (TEM)

TEM is a special microscope which helps us to get bigger image of an object at microscale or nanoscale range. By growing up the picture, it is easy to make observations in the atomic structure of the matter. The arrangements and alignments of chemical structures, shapes, surface morphology, crystallinity and particle size are easily determined by using “*transmission electron microscopy*” (TEM).

Light is used in optic microscopes and this provides us 250 nm resolutions for observations in micrometer area. In TEM, electron is used because of its wavelength is high compared with the light. Some TEM devices are capable to show down to 0.2 nm resolution. And this result confirms the usability of this technique at nanoscale range.

In medicine TEM is used also to detect chemical changes in a cell or microorganisms. The effect of an X-ray beam in 50 nm scale can be considered to investigate micro chemical analyses.

TEM analysis was performed using a FEI Tecnai G2 Sphera Microscope. A drop of diluted sample in alcohol was dripped on the grid. Following drying, the sample was loaded into a TEM column for analysis. Particle size distribution of $Zn_xNi_{1-x}Fe_2O_4$ nanoparticles was obtained from the micrographs, counting at least 75 particles. The benefit of TEM measurements was to supply information about morphology of the sample and visual results that which explains the crystallite structure. The shape and the existence of agglomeration are determined as well.

3.2.4 Magnetic Measurements

Magnetic properties of the as synthesized samples such as coercive field (H_c), saturation magnetization (M_s), and remanent magnetization (M_r), blocking temperature (T_B) values are measured by using Quantum Design Vibrating Sample Magnetometer (VSM). The samples are located in thin glass pipes, with 4-10 centimeters length and 1-2 millimeters of diameter. As it can be understood from the name of the device, samples must be located correctly into the vibrating sample magnetometer. Any vibration inside the sample causes distortion of the signal and may not be clear for identifying magnetic properties of a sample. That's why glass pipes are filled with powders nearly 3-4 mm thickness and paraffin has dumped after weighed the amount of substance. The frozen paraffin then made our sample motionless and provided us reliable measurements for analysing magnetic characteristics of Zn-Ni ferrite nanoparticles.

CHAPTER 4

RESULTS AND DISCUSSION

All data are evaluated and results of the structural and magnetic characterizations are plotted and discussed in this chapter. Following the synthesis process, FT-IR spectra of the samples are measured. Then X-Ray Powder Diffraction and TEM have been measured. VSM measurements were the last experimental part of our work. All graphs and datas are plotted and given below in the order of FT-IR, XRD, TEM and VSM.

4.1 Microwave Combustion Method: Synthesis with Citric Acid as Fuel

$Zn_xNi_{1-x}Fe_2O_4$ nanoparticles have been synthesized with different Zn ratios ($x = 0.0$, $x = 0.2$, $x = 0.5$, $x = 0.7$, $x = 1.0$) by microwave combustion method with using citric acid as a fuel. The structural, morphological and magnetic characterizations are explained as follows.

4.1.1 FT-IR Analysis

The FT-IR graph of all $Zn_xNi_{1-x}Fe_2O_4$ nanoparticles synthesized with citric acid is given in Fig. 4.1. Infrared spectra of dried ferrite samples were recorded on FTIR spectrometer in the range of $400-4000\text{cm}^{-1}$. All samples are prepared with KBr powder which is highly hygroscopic, and mixed with sample to construct thin pellets.

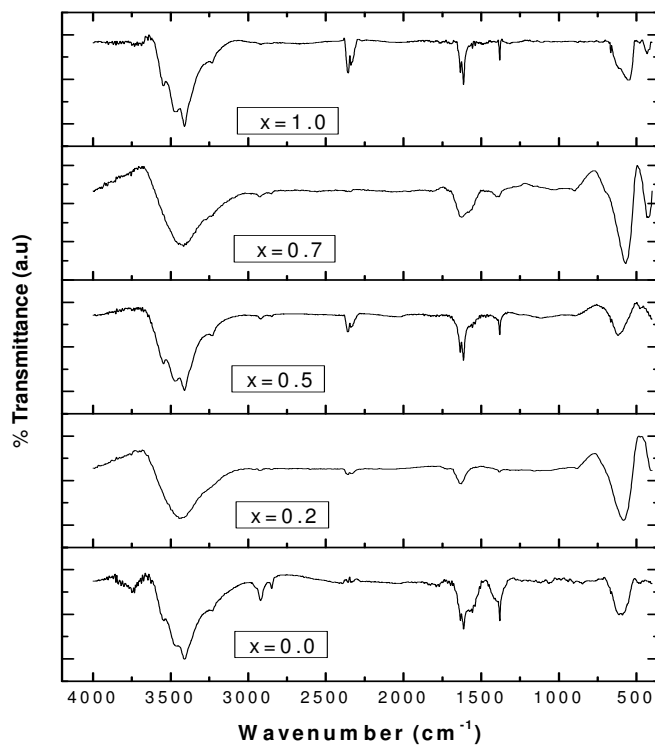


Figure 4.1 FT-IR spectra of the $Zn_xNi_{1-x}Fe_2O_4$ nanoparticles with Zn contents of $x = 0.0, 0.2, 0.5, 0.7$ and 1.0 synthesized by microwave combustion method using citric acid as fuel.

Two main peaks metal–oxygen bands are seen in the IR spectra of all spinels, and ferrites in particular. The peaks are observed in the range $616\text{--}590\text{ cm}^{-1}$. Increasing Zn content from 0 to 1 decreased the wavenumber as it is observed in Fig.4.1. The peaks around 1500 cm^{-1} comes from the stretching of the O-H bands and the peaks around 3500 cm^{-1} come from the bending of the O-H bands.

4.1.2 X-Ray Powder Diffraction Analysis

X-Ray diffraction pattern for $Zn_xNi_{1-x}Fe_2O_4$ nanoparticles with Zinc contents of $x = 0.0, x = 0.2, x = 0.5, x = 0.7$ and $x = 1.0$ synthesized by microwave combustion method using citric acid as fuel is given in Fig. 4.2. The hkl indices of the samples are

determined. For spinels (AB_2O_4), the expected peak is [311]. That gives the “spinel” information of compound. Other indices like (111, 220, 311, 400, 422, 511, 440, 620 and 533) shows another hkl miller indices that helps us to identify our sample.

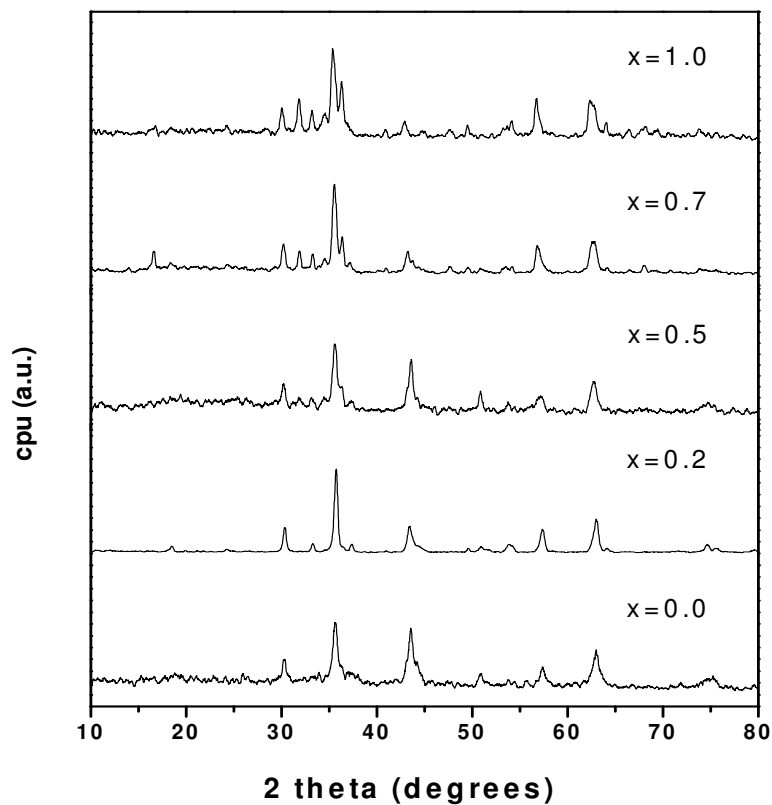


Figure 4.2 X-Ray diffraction pattern for $Zn_xNi_{1-x}Fe_2O_4$ nanoparticles with Zinc contents of $x = 0.0, 0.2, 0.5, 0.7$ and 1.0 synthesized by microwave combustion method using citric acid as fuel

The crystallite sizes of samples $Zn_xNi_{1-x}Fe_2O_4$ nanoparticles synthesized by citric acid are determined and given in Table 4.1. The (111), (220), (311), (400), (422), (511), (440) indices for the dimensions, resulted the size of particles in the range of 19 – 30 nm. A broad identification for [311] indices were not appeared providing higher size

nanoparticles. Crystal formation of $x = 0.2$ and $x = 0.7$ samples were better from the other compositions.

Table 4.1 Average particle sizes of $Zn_xNi_{1-x}Fe_2O_4$ nanoparticles calculated by using Debye-Scherrer equation synthesized by microwave combustion method using citric acid as fuel.

| Compounds | Crystallite Size (nm) (by Debye-Scherrer) |
|---------------------------|--|
| $NiFe_2O_4$ | 19.06 |
| $Zn_{0.2}Ni_{0.8}Fe_2O_4$ | 27.56 |
| $Zn_{0.5}Ni_{0.5}Fe_2O_4$ | 24.23 |
| $Zn_{0.7}Ni_{0.3}Fe_2O_4$ | 30.57 |
| $ZnFe_2O_4$ | 27.63 |

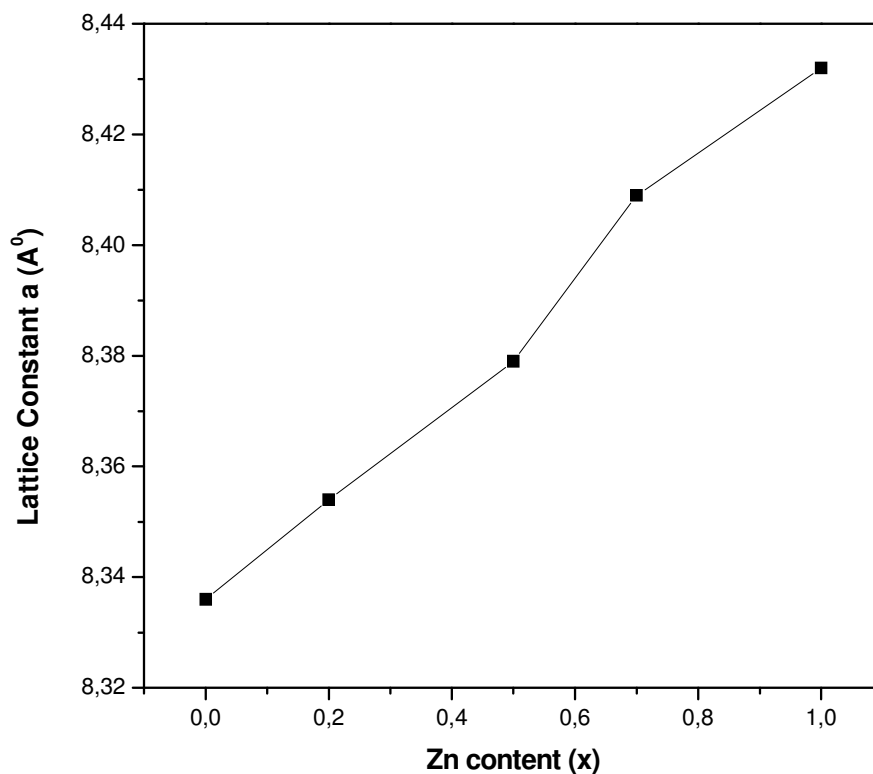


Figure 4.3 Lattice parameters of $Zn_xNi_{1-x}Fe_2O_4$ nanoparticles with synthesized by microwave combustion method using citric acid as fuel

The variation of lattice constant a as a function of Zn^{2+} is depicted in Fig. 4.3 for $Zn_xNi_{1-x}Fe_2O_4$ nanoparticles synthesized by microwave method using citric acid as fuel. The lattice parameters a have been computed using the d-spacing values and the respective (hkl) parameters from the classical formula [7] given in eqn. 4.1 :

$$a = \frac{\lambda}{2} \frac{[h^2 + k^2 + l^2]^{\frac{1}{2}}}{\sin \theta} \quad (4.1)$$

It is observed that the sample with higher Zn content has larger lattice parameters. The lattice parameter can also be affected by the distribution of metal Zn^{2+} and Ni^{2+} cations in the spinel structure [44]. We attribute this to the different radius of Zn (0.82 Å) and Ni (0.78 Å) which means that larger the ions correspond to the larger the lattice parameters [45].

4.1.3 TEM Micrographs of $Zn_xNi_{1-x}Fe_2O_4$ nanoparticles with citric acid

The TEM micrographs of $Zn_xNi_{1-x}Fe_2O_4$ nanoparticles synthesized by using citric acid are given in below, by starting from the $x = 0$ to $x = 1$. The crystallite structure and morphology are discussed in details. Average particle sizes calculated and compared with the XRD sizes obtained by using Debye-Scherrer formula. Particles have been counted on the TEM image as much as possible.

4.1.3.1 NiFe₂O₄ and Zn_{0.2}Ni_{0.8}Fe₂O₄ Nanoparticles

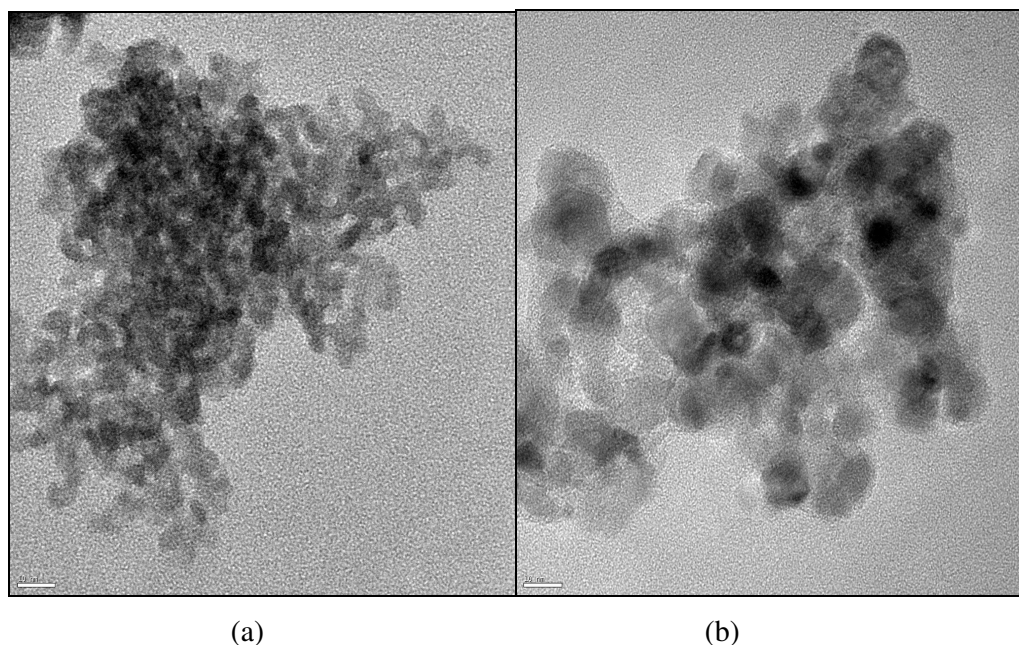


Figure 4.4 (a) The TEM micrograph of NiFe₂O₄ nanoparticles synthesized by using citric acid, (b) The TEM micrograph of Zn_{0.2}Ni_{0.8}Fe₂O₄ nanoparticles

The TEM micrograph of NiFe₂O₄ nanoparticles synthesized by using citric acid is given in Fig. 4.4 (a) and Fig. 4.4 (b). For the NiFe₂O₄ nanoparticles in Fig. 4.4 (a), the XRD size of NiFe₂O₄ nanoparticles was 19 nm.

75 nanoparticles have been counted and they seem to be spherical for Fig. 4.4 (b). The average particle size is about 10nm. XRD size was 28 nm. A blur and obscure view dominates here. Well crystallinity can not be obtained during the synthesis method. Heat and the temperature during the synthesis process may not be enough to ignite entire elements. Black regions denote the agglomeration of particles because of the uncontrolled temperature distribution resulting different sizes between 6-18 nm interval.

4.1.3.2 $\text{Zn}_{0.5}\text{Ni}_{0.5}\text{Fe}_2\text{O}_4$ and $\text{Zn}_{0.7}\text{Ni}_{0.3}\text{Fe}_2\text{O}_4$ Nanoparticles

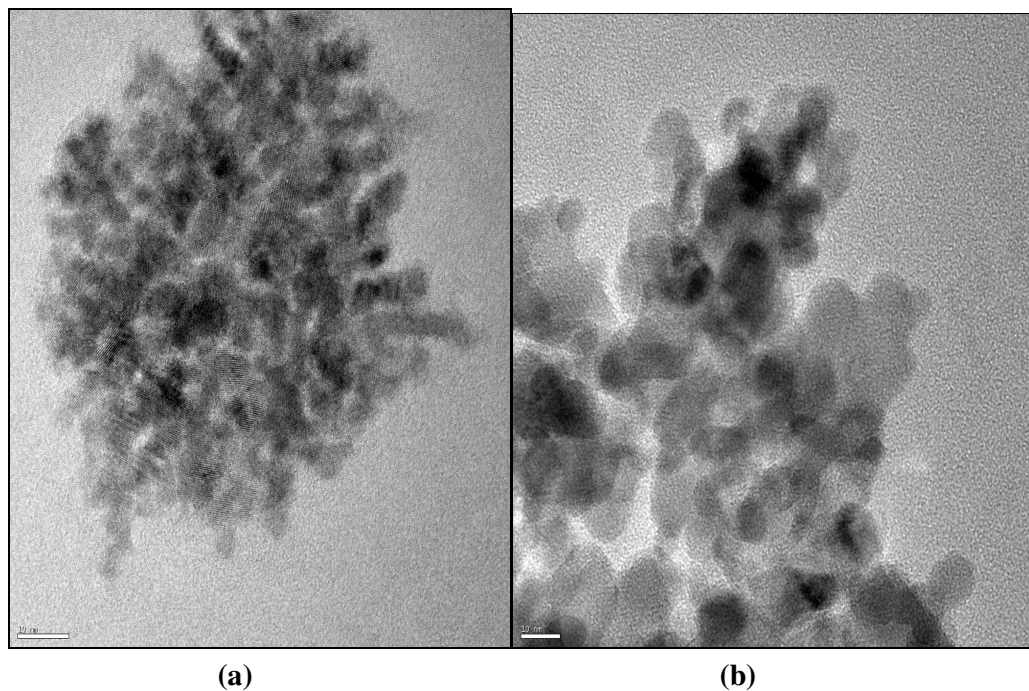


Figure 4.5 (a) The TEM micrograph of $\text{Zn}_{0.5}\text{Ni}_{0.5}\text{Fe}_2\text{O}_4$ nanoparticles synthesized by using citric acid, (b) The TEM micrograph of $\text{Zn}_{0.7}\text{Ni}_{0.3}\text{Fe}_2\text{O}_4$ nanoparticles

The TEM micrograph of $\text{Zn}_{0.5}\text{Ni}_{0.5}\text{Fe}_2\text{O}_4$ nanoparticles with 0.5 zinc content is given in Fig. 4.5 (a). Image is not clear but it seems like particles are agglomerated. Actual size of $\text{Zn}_{0.5}\text{Ni}_{0.5}\text{Fe}_2\text{O}_4$ nanoparticles obtained from XRD measurement is 24 nm. In figure, if black regions take into account, particle sizes can be estimated about 10-15 nm interval.

A better view for $\text{Zn}_{0.7}\text{Ni}_{0.3}\text{Fe}_2\text{O}_4$ compound is obtained in Fig. 4.5 (b) compared with the $\text{Zn}_{0.5}\text{Ni}_{0.5}\text{Fe}_2\text{O}_4$ nanoparticles. 20 particles have been counted here and average particle size is found as 12 nm. Photo has been taken at 10 nm scale. The XRD size was found as 31 nm.

4.1.3.3 ZnFe₂O₄ Nanoparticles

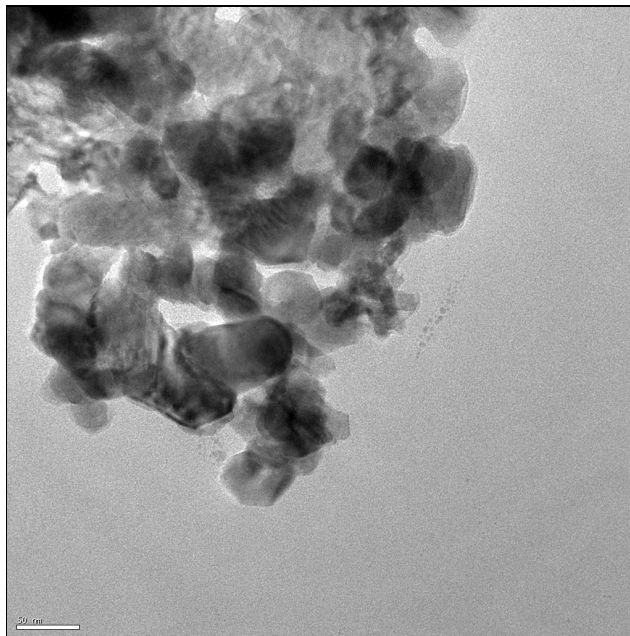


Figure 4.6 The TEM micrograph of ZnFe₂O₄ nanoparticles synthesized by using citric acid

In Fig. 4.6, the TEM micrograph of ZnFe₂O₄ nanoparticles seem bigger than XRD based calculation which is obtained for this sample as 30 nm. But when it is compared with the TEM micrograph at 50 nm scale, the existence of particles around 30 nm can be determined. Some regions have high contrast. Generally it is clear to observe the ZnFe₂O₄ nanoparticles. The XRD size and the size determined from the TEM micrograph are in consistency.

4.2 Microwave Combustion Method: Synthesis with Urea As Fuel

Zn_xNi_{1-x}Fe₂O₄ nanoparticles have been synthesized with different Zn ratios ($x = 0.0, x = 0.2, x = 0.5, x = 0.7, x = 1.0$) by microwave combustion method with using

urea as a fuel. The structural, morphological and magnetic characterizations are explained as follows.

4.2.1 FT-IR Analysis

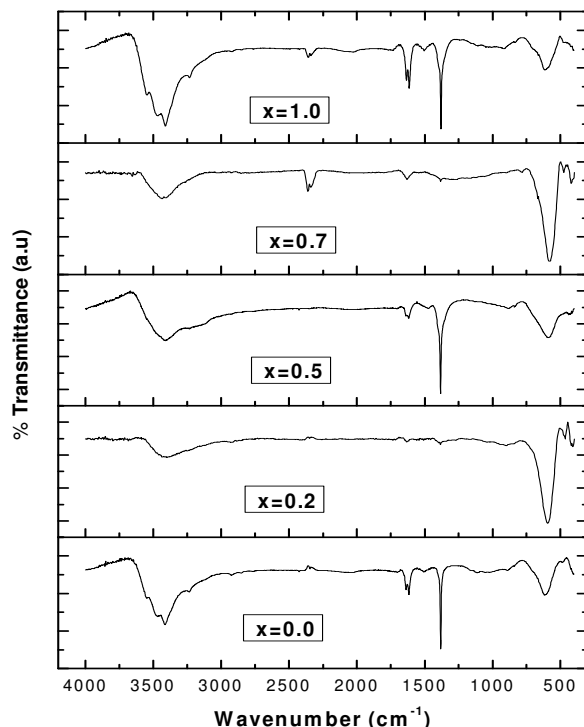


Figure 4.7 FT-IR spectra of the $Zn_xNi_{1-x}Fe_2O_4$ nanoparticles with Zn contents of $x = 0.0, 0.2, 0.5, 0.7$ and 1.0 synthesized by microwave combustion method using urea as fuel.

Two main broad metal–oxygen bands are seen in the IR spectra of all spinels, and ferrites in particular. The highest one generally observed in the range $600\text{--}550\text{ cm}^{-1}$ in Fig.4.7, corresponds to intrinsic stretching vibrations at the tetrahedral site. Ni^{2+} ions are known that they have octahedral-site preference, whereas Zn^{2+} and Fe^{3+} ions can occupy both octahedral and tetrahedral sites [6, 7]. No peaks have been observed due to octahedrally coordinated metal ions which is expected to be below 400 cm^{-1} . This may be due to the working range of our FT-IR instrument. The increase in Zn content from 0 to 1 denoted decrease in wavenumber.

4.2.2 X-Ray Powder Diffraction Analysis

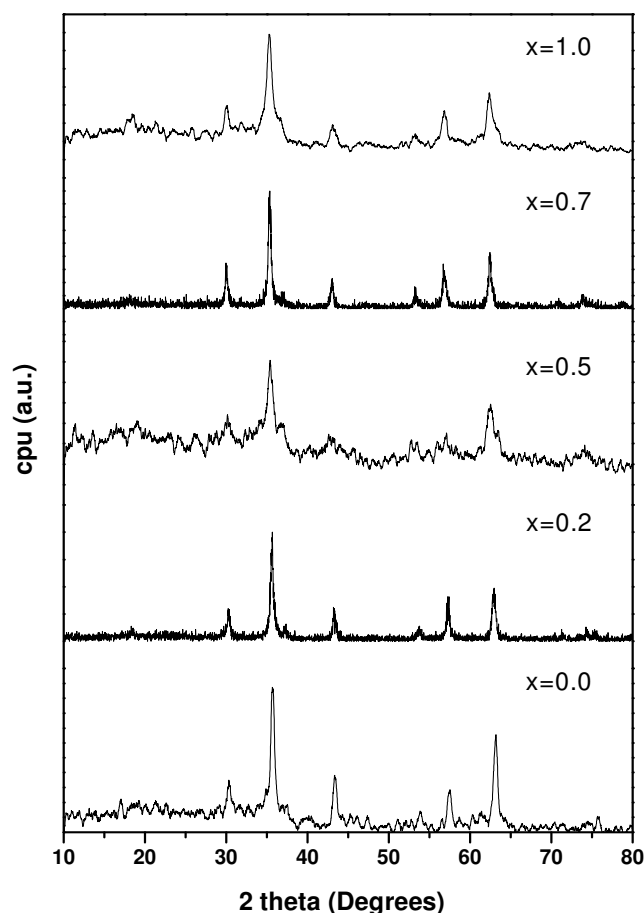


Figure 4.8 X-Ray diffraction pattern for $Zn_xNi_{1-x}Fe_2O_4$ nanoparticles with Zinc contents of $x = 0.0, 0.2, 0.5, 0.7$ and 1.0 synthesized by microwave combustion method using urea as fuel.

X-Ray diffraction pattern for $Zn_xNi_{1-x}Fe_2O_4$ nanoparticles with Zinc contents of $x = 0.0, 0.2, 0.5, 0.7$ and 1.0 synthesized by microwave combustion method using urea as fuel is given in Fig. 4.8. The samples synthesized with urea showed that, particle sizes differed from the samples that synthesized with citric acid. Table 4.2 shows the average particles sizes of the samples obtained by using the Debye-Scherrer equation. For urea, it is suitable to say that particle size is inversely proportional to the Zn ratio. The range changes a little but it is possible to see the decrease in particle size.

Table 4.2 Average particle sizes of $Zn_xNi_{1-x}Fe_2O_4$ nanoparticles calculated by using Debye-Scherrer equation synthesized by microwave combustion method using urea as fuel.

| Compounds | Crystallite Size (nm) (by Debye-Scherrer) |
|---------------------------|--|
| $NiFe_2O_4$ | 34.92 |
| $Zn_{0.2}Ni_{0.8}Fe_2O_4$ | 24.44 |
| $Zn_{0.5}Ni_{0.5}Fe_2O_4$ | 22.67 |
| $Zn_{0.7}Ni_{0.3}Fe_2O_4$ | 25.55 |
| $ZnFe_2O_4$ | 24.25 |

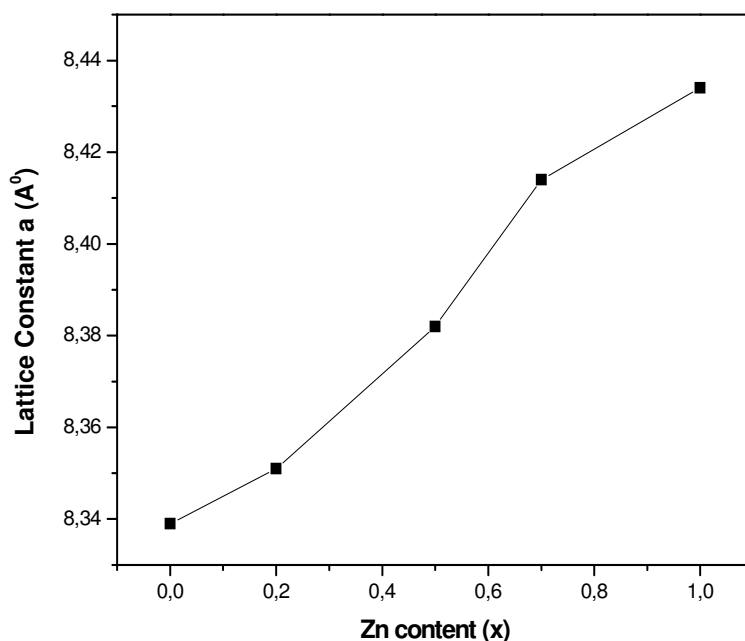


Figure 4.9 Lattice parameters of $Zn_xNi_{1-x}Fe_2O_4$ nanoparticles with synthesized by microwave combustion method using urea as fuel

The variation of lattice constant as a function of Zn content in $Zn_xNi_{1-x}Fe_2O_4$ nanoparticles with synthesized by microwave combustion method using urea as fuel is

given in Fig. 4.9. Sayed et al. [46] reported that $Zn_xNi_{1-x}Fe_2O_4$ samples have linear increase in the lattice constant from 8.362 to 8.442 Å in between $y = 0.1$ to 0.9. This result agrees with our samples synthesized with the microwave combustion method using urea as fuel. The lattice parameters in Fig. 4.9 are obtained in the range of 8.339-8.434 Å which is consistent with above values. It is seen that lattice parameter is increased by increasing the Zn content [47].

4.2.3 TEM Micrographs of $Zn_xNi_{1-x}Fe_2O_4$ Nanoparticles with Urea

The TEM micrographs of $Zn_xNi_{1-x}Fe_2O_4$ nanoparticles synthesized by urea as fuel are given in below, by starting from the $x = 0$, to $x = 1$. The crystallite structure and morphology are discussed in details as it has been done for citric acid. Average particle sizes and the XRD sizes obtained by using Debye-Scherrer formula are compared.

4.2.3.1 $NiFe_2O_4$ and $Zn_{0.2}Ni_{0.8}Fe_2O_4$ Nanoparticles

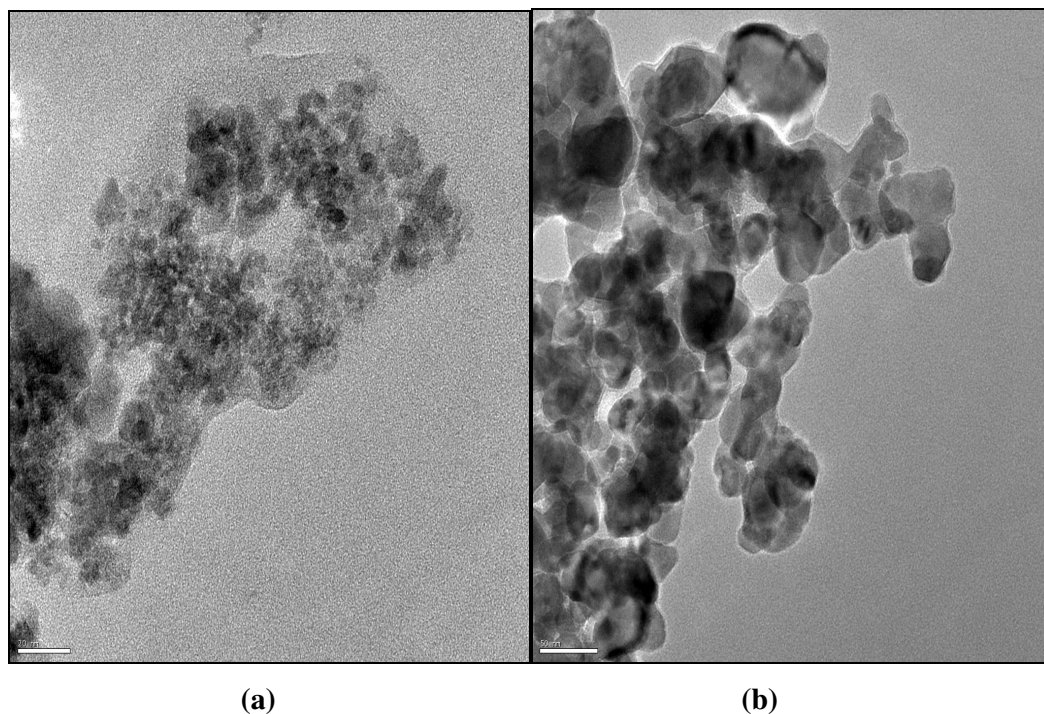


Figure 4.10 (a) The TEM micrograph of $NiFe_2O_4$ nanoparticles synthesized by using urea, (b) The TEM micrograph of $Zn_{0.2}Ni_{0.8}Fe_2O_4$ nanoparticles.

The result of TEM micrograph of NiFe_2O_4 nanoparticles synthesized by using urea at 20 nm scale is given in Fig. 4.10 (a). Decreasing resolution from 100 nm to smaller scale, the image loses its clear view. When both micrographs are compared with each other, high scale observations showed that crystalline structure seems easier at high 50 nm. But, the Fig. 4.10 (a) was the best image that has been detected for the NiFe_2O_4 nanoparticles. The XRD size of the particles are 35 nm. So the result of TEM micrograph shows us NiFe_2O_4 nanoparticles in the right coast of image but it should be said that general image about the center of image has a suspicious effect like some of the particles divided into grains during the synthesis process.

In the TEM micrograph of $\text{Zn}_{0.2}\text{Ni}_{0.8}\text{Fe}_2\text{O}_4$ nanoparticles showed Fig.4.10 (b), it's not difficult to say that the crystals are evident at the scale of 50 nm. 25 particles have been detected here and the average particle size is found as 26 nm. The XRD size of this sample was 24 nm which agrees well with the TEM micrograph. Particles seem to be agglomerated in dark areas by superimposing to each other.

4.2.3.2 $\text{Zn}_{0.5}\text{Ni}_{0.5}\text{Fe}_2\text{O}_4$ and $\text{Zn}_{0.7}\text{Ni}_{0.3}\text{Fe}_2\text{O}_4$ Nanoparticles

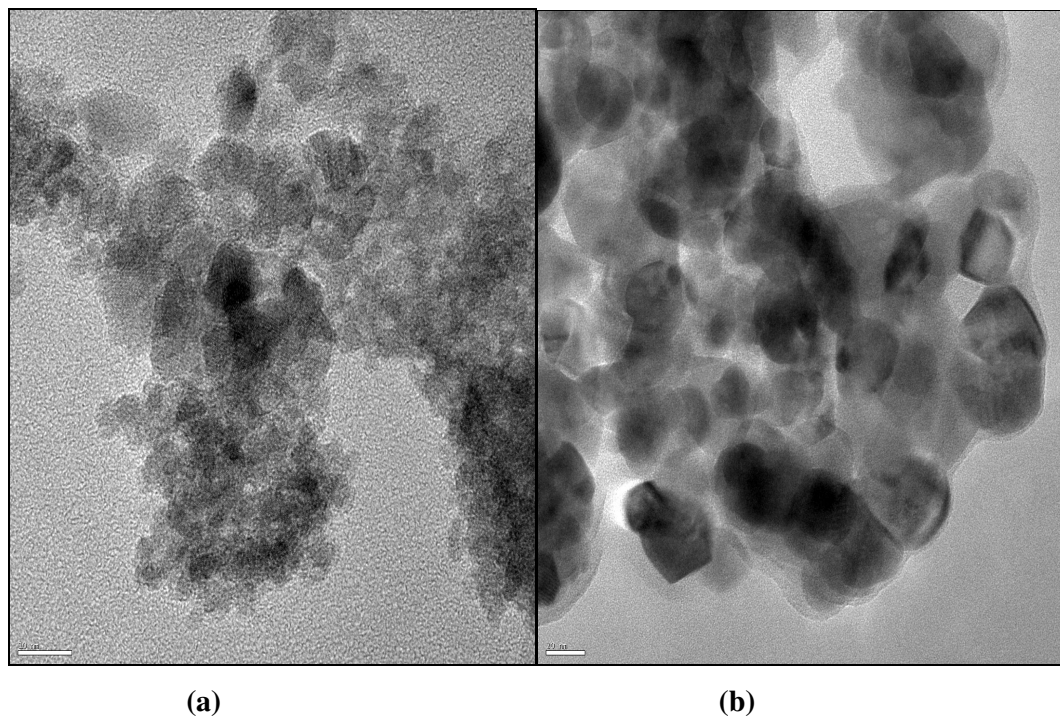


Figure 4.11 (a) The TEM micrograph of $\text{Zn}_{0.5}\text{Ni}_{0.5}\text{Fe}_2\text{O}_4$ nanoparticles synthesized by using urea, (b) The TEM micrograph of $\text{Zn}_{0.7}\text{Ni}_{0.3}\text{Fe}_2\text{O}_4$ nanoparticles.

The TEM micrograph of $\text{Zn}_{0.5}\text{Ni}_{0.5}\text{Fe}_2\text{O}_4$ nanoparticles in Fig.4.11 (a) have many grains large and small. Only some of them should be seen in the center of image at 10 nm scale. Their sizes are about 20-25 nm range. XRD based size estimation of $\text{Zn}_{0.5}\text{Ni}_{0.5}\text{Fe}_2\text{O}_4$ particles is 23 nm which agrees well with the TEM micrograph in Fig. 4.11 (a).

For the TEM micrograph of $\text{Zn}_{0.7}\text{Ni}_{0.3}\text{Fe}_2\text{O}_4$ nanoparticles, the image existing black regions is clear. 25 particles have been counted in Fig. 4.11 (b) at 20 nm scale and average particle size is found 24 nm. The XRD size of the sample was 26 nm which is consistent with the size obtained from the TEM micrograph.

4.2.3.3 ZnFe_2O_4 Nanoparticles

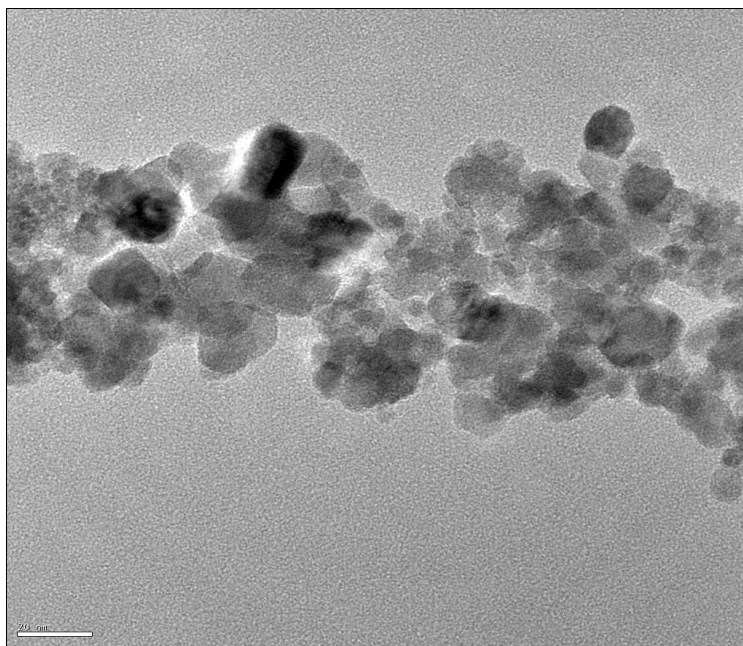


Figure 4.12 The TEM micrograph of ZnFe_2O_4 nanoparticles synthesized by using urea.

The TEM micrograph of ZnFe_2O_4 in Fig. 4.12 shows entire structure of zinc ferrite. Measurement was performed at 20 nm scale and average particle size is found as 16 nm which is smaller than that was found from the XRD based size estimation as 24 nm.

4.3 Results of Magnetization Measurements for $\text{Zn}_x\text{Ni}_{1-x}\text{Fe}_2\text{O}_4$ Nanoparticles Synthesized by Microwave Combustion Method

The microwave combustion method was a quick and efficient solution for producing chemical compounds. Urea and citric acid was chosen as fuels to understand their effect on magnetic properties of $\text{Zn}_x\text{Ni}_{1-x}\text{Fe}_2\text{O}_4$ nanoparticles. Magnetic measurements were carried out with the Quantum Design Model 6000 vibrating sample magnetometer (VSM) option for the physical property measurement system (PPMS) and parameters like specific saturation magnetization (M_s), coercive force (H_c) and remanence (M_r) were analysed. The results obtained for each sample have shown below, respectively.

4.3.1 NiFe_2O_4 Nanoparticles

NiFe_2O_4 is synthesized by microwave combustion method for both urea and citric acid used as fuels separately and their room temperature magnetic hysteresis loops (M-H curves) are shown in Fig. 4.13.

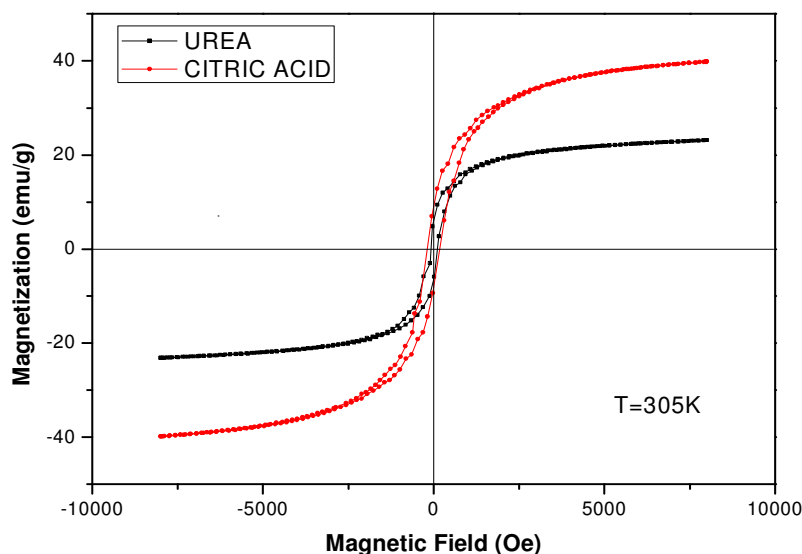


Figure 4.13 The room temperature magnetic field vs magnetization (M-H) curve of NiFe_2O_4 nanoparticles synthesized by microwave combustion method using urea and citric acid as fuel.

The magnetic hysteresis curves were recorded by sweeping the external field between ± 8 kOe at room temperature. M-H curves of both samples show ferromagnetic behavior at room temperature. Both curves do not reach saturation even at 8 kOe applied field and has s shape with hysteresis. For citric acid a coercive field (H_c) of 187 Oe is found where as H_c of urea was 94 Oe. The coercivities of two samples differs on each graph. The saturation magnetization (M_s calculated from a plot of M vs. $1/H$ (M at $1/H \geq 0$)) value of the samples is found as 43.7 emu/g for citric acid and 24.4 emu/g for urea, separately. It is seen that magnetization of NiFe_2O_4 has higher saturation and coercivity when it has been synthesized with citric acid.

4.3.2 $\text{Zn}_{0.2}\text{Ni}_{0.8}\text{Fe}_2\text{O}_4$ Nanoparticles

Zinc is doped to the NiFe_2O_4 with the ratios of $x = 0.0$, $x = 0.2$, $x = 0.5$, $x = 0.7$ and $x = 1.0$. Room temperature magnetization is observed for both urea and citric acid and M-H graph is plotted.

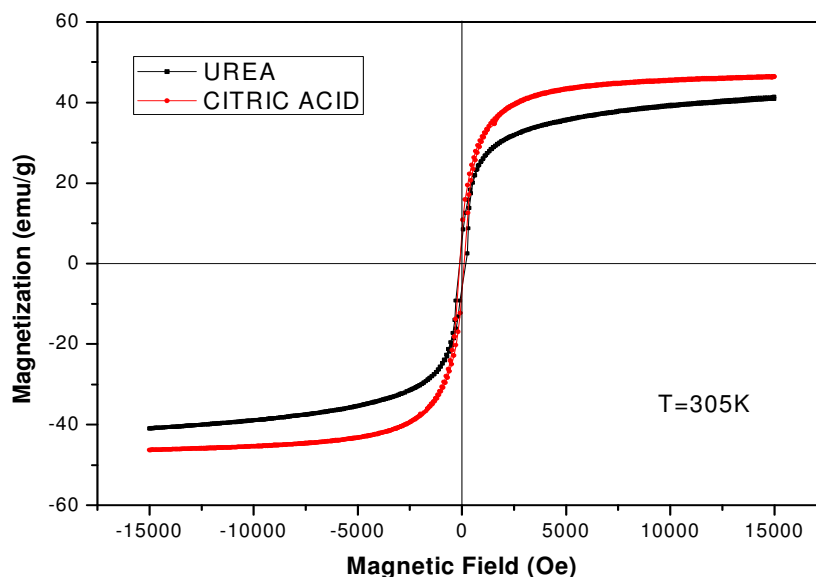


Figure 4.14 Magnetic field vs magnetization curve of $Zn_{0.2}Ni_{0.8}Fe_2O_4$ synthesized by microwave combustion method using urea and citric acid as fuel at room temperature.

Saturation magnetization (M_s), and coercive field (H_c) have been observed from the M-H curve of $Zn_{0.2}Ni_{0.8}Fe_2O_4$ synthesized by microwave combustion method using urea and citric acid as fuel at room temperature in Fig. 4.14. M_s for urea is measured as 44.5 emu/g from the extrapolation of M vs $1/H$ graph. Zn ratio is increased to 0.2 and it has been seen that magnetization increased twice (M_s without Zn was 24.4 emu/g) compared to previous sample. The cation distribution and orientation of spins may cause this alignment. Same behavior can be observed with same reason for citric acid. But increase of magnetization is not as urea. It is about 4 emu/g. Citric acid is a chemical compound that consists carbon atoms. Carbon is flammable and should provide more heat during the combustion. The reaction temperature did not measured, where as microwave Owen's knob was set to $150^\circ C$. Heat difference can be a reason of magnetization change in urea and citric acid.

In the compound with urea coercive field is increased to 149.21 Oe, despite it decreased to 104 Oe in the compound with citric acid. Heat transfer to the formation of crystallinity should cause this difference.

4.3.3 $\text{Zn}_{0.5}\text{Ni}_{0.5}\text{Fe}_2\text{O}_4$ Nanoparticles

Zn content is now 0.5 and it is expected that some of magnetic properties will decrease in this sample because of the non-magnetic nature of the Zn^{2+} ions in Fig. 4.15.

Magnetic field measurements are carried out up to 8 KOe in both sides and M-H curves are obtained for both of fuels again. The saturation magnetization is higher than previous sample. 57.22 emu/g is read from M-1/H graph for citric acid sample. When we have a look to the urea, saturation magnetization is found to decrease to 18.5 emu/g value. The coercive field of $\text{Zn}_{0.5}\text{Ni}_{0.5}\text{Fe}_2\text{O}_4$ nanoparticles seem larger than urea and the value is 153 Oe which provides our view from the graph. Same trend did not observe for urea. The H_c of urea has decreased to 42.79 Oe. The M-H curve of sample seems like a superparamagnetic behavior for urea sample because of tiny coercivity and a straight saturation line which does not saturate even at high magnetic fields.

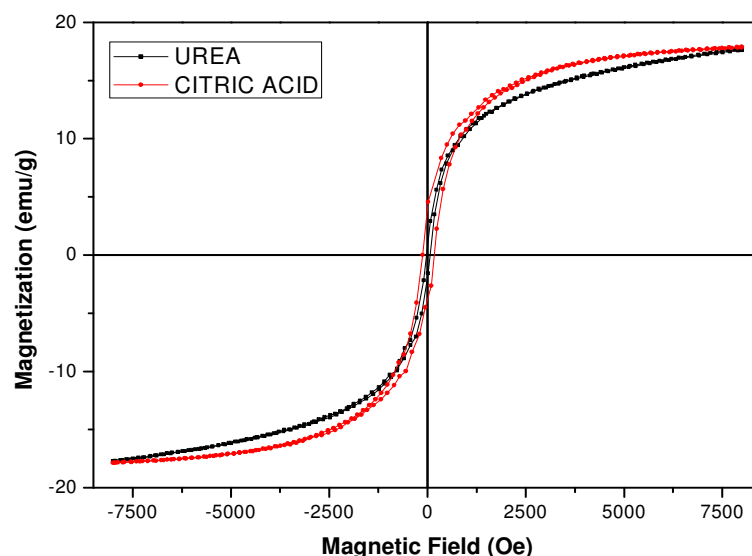


Figure 4.15 Magnetic field vs magnetization curve of $\text{Zn}_{0.5}\text{Ni}_{0.5}\text{Fe}_2\text{O}_4$ synthesized by microwave combustion method using urea and citric acid as fuel at room temperature.

The molecular weight of the urea is only 60 g/mol and, it consists only one C atom in its structure. When heat is occurred in microwave oven, there may not be enough heat

because ignition of the urea and this may not supply heat during synthesis process. And this situation should bring a decrease of magnetic properties and crystallinity for this sample.

4.3.4 $\text{Zn}_{0.7}\text{Ni}_{0.3}\text{Fe}_2\text{O}_4$ Nanoparticles

Magnetic field vs magnetization curve of $\text{Zn}_{0.7}\text{Ni}_{0.3}\text{Fe}_2\text{O}_4$ synthesized by microwave combustion method using urea and citric acid as fuel at room temperature is given in Fig. 4.16.

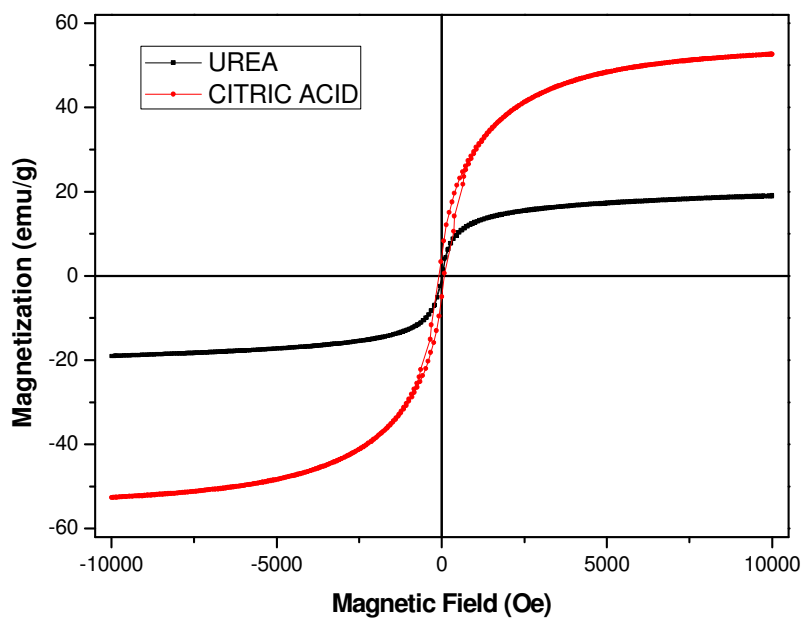


Figure 4.16 Magnetic field vs magnetization curve of $\text{Zn}_{0.7}\text{Ni}_{0.3}\text{Fe}_2\text{O}_4$ synthesized by microwave combustion method using urea and citric acid as fuel at room temperature.

The coercive field and saturation magnetization decreased in citric acid sample. H_c is measured as 81 Oe where the sample synthesized with urea was 7.98 Oe. Urea shows superparamagnetic behavior here because it seems like “s-shape”, coercive field is

nearly zero, and the saturation magnetization obtained from M-1/H plot is 28.6 emu/g. The M_s of citric acid has 104.69 emu/g which is very high compared with the previous sample. In $Zn_{0.5}Ni_{0.5}Fe_2O_4$ sample, saturation magnetization was %50 percent of Zn 0.7 sample. Citric acid has more efficiency in this graph. As it has been said before, this situation may be related to the heat that reveals the role of carbon atoms in the citric acid's structure. The increase in Zn ratio in this sample can locate Zn ions in tetrahedral sites. That explains why Ni atoms can't make bonds with Fe^{2+} ions inside the crystal. The nickel, which is a magnetic element in nature, loses its efficiency in octahedral sites this sample. So, it is expected that the sample will have lower magnetization values compared with the previous sample.

4.3.5 $ZnFe_2O_4$ Nanoparticles

The room temperature magnetic field vs magnetization curves of $ZnFe_2O_4$ nanoparticles synthesized by microwave combustion method using urea and citric acid as fuel are plotted in Fig. 4.17. The coercivity of the sample with citric acid is measured as 119 Oe. The magnetization of $ZnFe_2O_4$ sample synthesized with citric acid did not attain saturation even at high magnetic field of 8 kOe. The saturation magnetization, M_s , of the sample was found as 18 emu/g at room temperature.

In the $ZnFe_2O_4$ samples synthesized with urea shows approximately linear magnetic field dependence. But, when we analyse this curve more accurately, it has coercive field of 57 Oe and a saturation magnetization, M_s , of 3.0 emu/g. The evidence of almost closed hysteresis loop and weak saturation for urea confirms the superparamagnetic behavior of $ZnFe_2O_4$ nanoparticle at around room temperature. Low coercivity values are often observed in soft ferrites [24]. The M-H graph of sample also confirms that Zn-ferrites is soft ferrite.

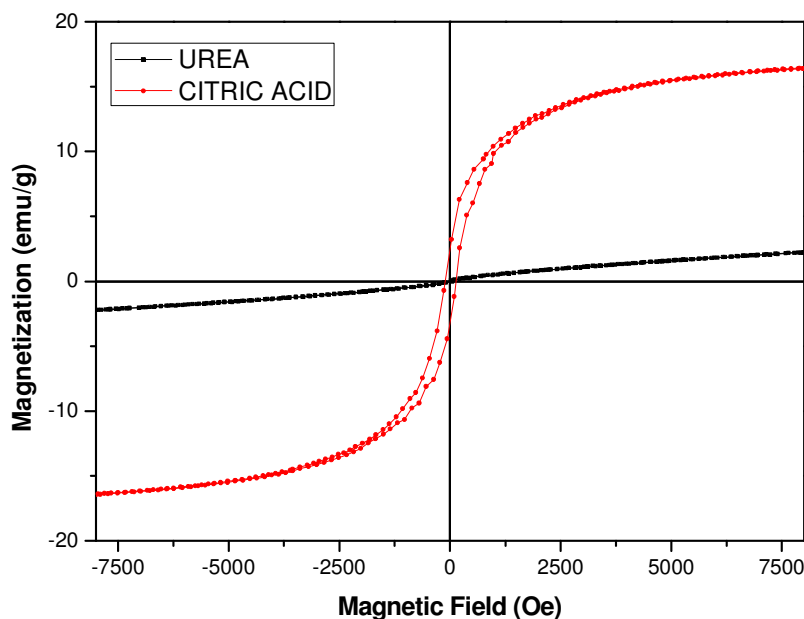


Figure 4.17 Magnetic field vs magnetization curve of ZnFe_2O_4 synthesized by microwave combustion method using urea and citric acid as fuel at room temperature.

As a result, when we increase the Zn content (x), the coercivity and saturation magnetization (M_s) of $\text{Zn}_x\text{Ni}_{1-x}\text{Fe}_2\text{O}_4$ nanoparticles is found to decrease. If we take into account the effect of the fuels (urea and citric acid), the saturation magnetization and the coercivity of the samples synthesized with citric acid are greater than those of samples synthesized with urea. All of these informations can easily be seen in tables 4.3 and 4.4. Actually ZnFe_2O_4 with urea is expected to have less magnetic properties than $\text{Zn}_{0.7}\text{Ni}_{0.3}\text{Fe}_2\text{O}_4$ but this situation may be attributed to the reaction mechanism in the synthesis process. The transfer of heat may cause this difference.

The Table 4.3 showing the mean particle diameter and magnetic parameters of $\text{Zn}_x\text{Ni}_{1-x}\text{Fe}_2\text{O}_4$ nanoparticles is obtained from the as synthesized $\text{Zn}_x\text{Ni}_{1-x}\text{Fe}_2\text{O}_4$ ($x = 0.0, 0.2, 0.5, 0.7$ and 1.0) samples using citric acid as fuel at room temperature. Saturation magnetizations, coercive fields and particle diameters calculated from XRD are given.

Table 4.3 Mean particle diameter and magnetic parameters with an applied magnetic field of $Zn_xNi_{1-x}Fe_2O_4$ nanoparticles synthesized using citric acid as fuel at room temperature.

| Compound | Mean Diameter (X-Ray) D (nm) | Hc (Oe) (at 305K) | M _s (emu/g) (at 305K) |
|--|--------------------------------|---------------------|------------------------------------|
| NiFe ₂ O ₄ | 19.07 | 187 | 44 |
| Zn _{0.2} Ni _{0.8} Fe ₂ O ₄ | 27.56 | 106 | 48 |
| Zn _{0.5} Ni _{0.5} Fe ₂ O ₄ | 24.24 | 153 | 57 |
| Zn _{0.7} Ni _{0.3} Fe ₂ O ₄ | 30.56 | 81 | 76 |
| ZnFe ₂ O ₄ | 29.94 | 119 | 18 |

The Table 4.4 which shows the mean particle diameter and magnetic parameters of $Zn_xNi_{1-x}Fe_2O_4$ nanoparticles is obtained from the as synthesized $Zn_xNi_{1-x}Fe_2O_4$ ($x = 0.0, 0.2, 0.5, 0.7$ and 1.0) samples using urea as fuel at room temperature. The saturation magnetization for $Zn_xNi_{1-x}Fe_2O_4$ nanoparticles measured at room temperature is observed to decrease by increasing Zn content. The poor crystallinity of $Zn_xNi_{1-x}Fe_2O_4$ samples can lead to some additional degree of deviation from the applied field of magnetization and local canting of magnetic moments [48, 49]. Saturation magnetizations, coercive fields and particle diameters calculated from XRD can be compared for urea as well.

Table 4.4 Mean particle diameter and magnetic parameters with an applied magnetic field of $Zn_xNi_{1-x}Fe_2O_4$ nanoparticles synthesized using urea as fuel at room temperature.

| Compound | Mean Diameter (X-Ray) D (nm) | Hc (Oe) (at 305K) | M _s (emu/g) (at 305K) |
|--|--------------------------------|---------------------|------------------------------------|
| NiFe ₂ O ₄ | 34.92 | 93.76 | 24.4 |
| Zn _{0.2} Ni _{0.8} Fe ₂ O ₄ | 24.44 | 149.21 | 44.5 |
| Zn _{0.5} Ni _{0.5} Fe ₂ O ₄ | 22.67 | 42.79 | 18.5 |
| Zn _{0.7} Ni _{0.3} Fe ₂ O ₄ | 25.55 | 7.98 | 28.6 |
| ZnFe ₂ O ₄ | 24.25 | 56.93 | 3.0 |

4.4 Hydrothermal Method: Synthesis with PEG 400 as a Surfactant

$Zn_xNi_{1-x}Fe_2O_4$ nanoparticles ($x = 0.0, x = 0.2, x = 0.4, x = 0.6, x = 0.8, x = 1.0$) have been successfully prepared through a polyethylene glycol (PEG)-assisted route. XRD, FTIR, TEM and VSM were used for the structural, morphological and magnetic investigation of product respectively.

4.4.1 FT-IR Analysis

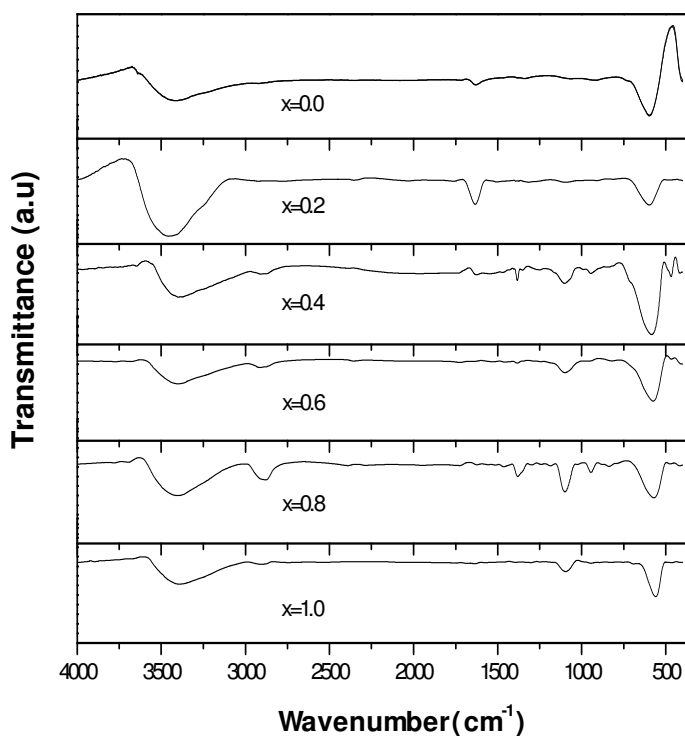


Figure 4.18 FT-IR spectra of the $Zn_xNi_{1-x}Fe_2O_4$ nanoparticles with Zn contents of $x = 0.0, 0.2, 0.4, 0.6, 0.8$ and 1.0 synthesized by hydrothermal method with PEG 400.

FT-IR spectra of the $Zn_xNi_{1-x}Fe_2O_4$ nanoparticles with Zn contents of $x = 0.0, 0.2, 0.4, 0.6, 0.8$ and 1.0 synthesized by hydrothermal method with PEG 400 is shown in Fig

4.18. Two broad peaks are observed around 3300 cm^{-1} and 590 cm^{-1} . First peaks located at 3300 cm^{-1} which come from the humidity of the sample. Second peaks denote the existence of AB_2O_4 spinel structure. Variation of wavenumber by increasing Zn content from $x = 0.0$ to $x = 1.0$, the decrease of wavenumber from 602 cm^{-1} to 559 cm^{-1} is observed as well.

To prevent water peaks in samples, they have been heated to vaporize the water inside the matrix. Despite drying process, sample $x = 0.2$ has bigger water peak compared with the other products.

4.4.2 X-Ray Powder Diffraction Analysis

The powder X-ray diffractograms recorded for samples of series $\text{Zn}_x\text{Ni}_{1-x}\text{Fe}_2\text{O}_4$ (with $x = 0.0, 0.2, 0.4, 0.6, 0.8$ and 1.0) are shown in Fig. 4.19. Samples are considered to be single-phase spinel structure as no extra peaks and no unreacted constituents were observed. The shift of (311) peak to small diffraction angles with the increase of Zn content in Fig. 4.19 reveals that the sample with higher Zn content has larger lattice parameters [45]. We attribute this to the different radius of Zn (0.82Å) and Ni (0.78 Å) which means that the larger the ions have the larger the lattice parameters [50].

This allows the estimation of average crystallite size and its standard deviation from XRD. The experimental line profiles, shown in Fig. 4.19, were fitted for 9 peaks (111), (220), (311), (400), (422), (511), (440) (622) and (533) the calculated average crystallite size D (and standard deviations σ), and the sizes found from Debye-Scherrer equation are presented in Table 4.5.

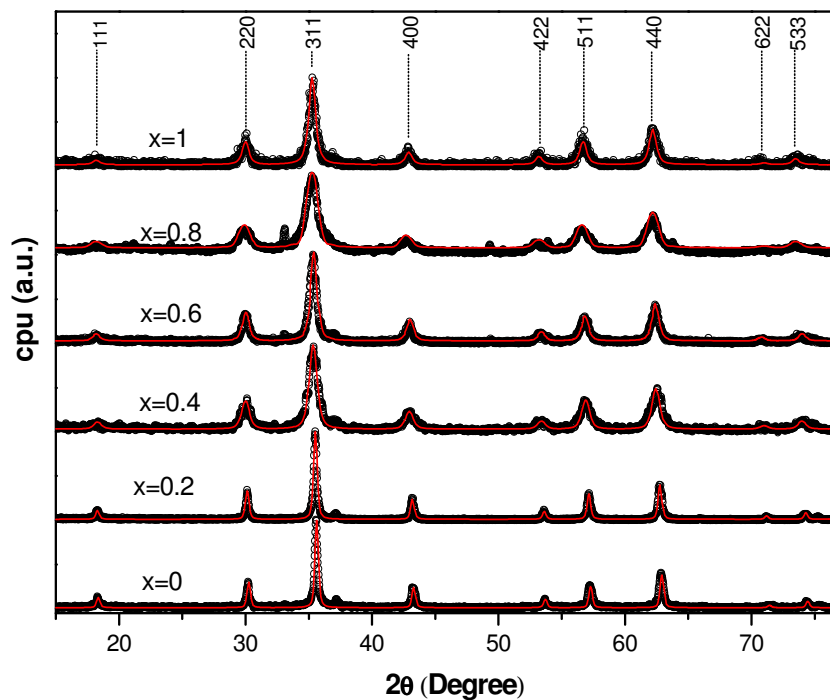


Figure 4.19 Experimental and theoretically fitted XRD patterns of $(\text{Zn}_x\text{Ni}_{1-x}\text{Fe}_2\text{O}_4)$ nanoparticles (from $x = 0$ to 1).

Table 4.5 The obtained particle sizes of $\text{Zn}_x\text{Ni}_{1-x}\text{Fe}_2\text{O}_4$ nanoparticles (from $x = 0$ to 1) for (a) Experimental data (by Debye-Scherrer), (b) XRD - profile fit

| Composition X | (a) Crystallite Size (nm) (by Debye-Scherrer) | (b) D_{XRD} (σ) Av. Size (StD.) |
|------------------|--|--|
| 1 | 14.35 | 12.1(4.2) |
| 0.8 | 11.42 | 9.1 (1.5) |
| 0.6 | 14.00 | 14.1 (5.0) |
| 0.4 | 13.20 | 11.9 (4.0) |
| 0.2 | 28.38 | 26.0 (9.0) |
| 0 | 30.03 | 37 (0.23) |

The cation distribution in $Zn_xNi_{1-x}Fe_2O_4$ can be inferred from the X-ray diffraction relative integrated intensity calculations by using the following formula suggested by Buerger [51]:

$$I_{hkl} = |F|_{hkl}^2 PL_p \quad (4.2)$$

where F is the structure factor, P the multiplicity factor and L_p is the Lorenz-polarization factor which depends only on the Bragg's diffraction angle θ

$$L_p = \frac{1 + \cos^2 2\theta}{\sin^2 \theta \cos 2\theta} \quad (4.3)$$

Some peaks' intensity ratios in the XRD pattern of spinel structures were reported as cation distribution sensitive peaks, such as I_{220}/I_{400} , I_{220}/I_{422} and I_{422}/I_{400} [52, 53]. In the calculations (i) all possible cation arrangements are considered with 0.01 stoichiometric sensitivity that Ni^{+2} , Zn^{+2} and Fe^{+3} can site both tetrahedral and octahedral sites, (ii) the oxygen positional parameter was chosen between 0.3700 and 0.3900, which includes that of Zn ferrites, Ni ferrites and ideal spinel structures that are 0.3852, 0.3822 and 0.375 respectively [54] and (iii) for the agreement of calculated and experimental intensity ratios, the difference of calculated and experimental relative intensities for all distribution cases are considered and the sum of these differences are minimized. Finally the closest calculated data are taken to be the correct distributions. Note that there should be no need for the thermal correction because of the spinel's high melting temperature and hence very small thermo-vibrational effect of spinel on XRD patterns [55]. As a result the experimental lattice constants, chosen oxygen positional parameters, the relative intensities of experimental and calculated XRD peaks, and their corresponding cation distribution results are listed in Table 4.6. The occupancy of Fe^{+3} ions on A site is greater than 0.78 and in all substance the Fe^{+3} ions dominate in T_d sub lattice.

Table 4.6 The values of XRD cation distribution in $Zn_xNi_{1-x}Fe_2O_4$ nanoparticles ($x = 0$ to 1).

| $Zn_xNi_{1-x}Fe_2O_4$ Composition x | Lattice Parameter a (Å) | Oxygen Positional Parameter u | Cation Distribution | I_{220}/I_{400} | | I_{422}/I_{400} | |
|---|----------------------------------|--|--|-------------------|------|-------------------|------|
| | | | | Obs. | Cal. | Obs. | Cal. |
| 1 | 8.45 | 0.3850 | $(Zn_{0.01}Fe_{0.99})$ $[Zn_{0.99}Fe_{1.01}]$ | 1.15 | 1.12 | 0.46 | 0.41 |
| 0.8 | 8.45 | 0.3840 | $(Ni_{0.07}Zn_{0.00}Fe_{0.93})$ $[Ni_{0.13}Zn_{0.80}Fe_{1.07}]$ | 1.14 | 1.15 | 0.50 | 0.43 |
| 0.6 | 8.41 | 0.3830 | $(Ni_{0.07}Zn_{0.06}Fe_{0.87})$ $[Ni_{0.33}Zn_{0.54}Fe_{1.13}]$ | 1.25 | 1.23 | 0.41 | 0.45 |
| 0.4 | 8.42 | 0.3825 | $(Ni_{0.17}Zn_{0.00}Fe_{0.83})$ $[Ni_{0.43}Zn_{0.40}Fe_{1.17}]$ | 1.26 | 1.23 | 0.41 | 0.46 |
| 0.2 | 8.38 | 0.3780 | $(Ni_{0.00}Zn_{0.06}Fe_{0.94})$ $[Ni_{0.80}Zn_{0.14}Fe_{1.06}]$ | 1.21 | 1.19 | 0.43 | 0.45 |
| 0 | 8.36 | 0.3750 | $(Ni_{0.22}Fe_{0.78})$ $[Ni_{0.78}Fe_{1.22}]$ | 1.25 | 1.27 | 0.52 | 0.48 |

In the spinel structure the cations on different sub lattices (A and B sites) have oppositely aligned magnetic moments according to the Neel's ferrimagnetic theory [56]. So the magnetic moment per formula unit in μ_B (Bohr magneton) is

$$n_B(x) = M_B(x) - M_A(x) \quad (4.4)$$

where M_B and M_A are B and A site magnetic moment in μ_B . The magnetic moment per formula unit is calculated by cation distribution results of XRD and Neel's theory with ionic magnetic moment of $5\mu_B$, $2\mu_B$ and $0\mu_B$ for Fe^{+3} , Ni^{+2} and Zn^{+2} , respectively [53]. The results are summarized in Table 4.7. The calculated n_B values agreed well with experimentally obtained values for all x, confirming a collinear magnetic structure.

Table 4.7 The magnetic moment per unit formula from XRD and VSM for $Zn_xNi_{1-x}Fe_2O_4$ nanoparticles ($x = 0$ to 1)

| Zn _x Ni _{1-x} Fe ₂ O ₄ Composition x | Cation Distribution (XRD) | Saturation Magnetization Ms (emu/g) (VSM) | Magneton number n _B (μ _B) | |
|--|---|--|--|---------------|
| | | | Obs. (VSM) | Cal. (XRD) |
| 1 | (Ni _{0.22} Fe _{0.78}) [Ni _{0.78} Fe _{1.22}] | 80.24 | 3.36 | 3.32 |
| 0.8 | (Ni _{0.00} Zn _{0.06} Fe _{0.94}) [Ni _{0.80} Zn _{0.14} Fe _{1.06}] | 50.19 | 2.12 | 2.20 |
| 0.6 | (Ni _{0.17} Zn _{0.00} Fe _{0.83}) [Ni _{0.43} Zn _{0.40} Fe _{1.17}] | 50.93 | 2.16 | 2.20 |
| 0.4 | (Ni _{0.07} Zn _{0.06} Fe _{0.87}) [Ni _{0.33} Zn _{0.54} Fe _{1.13}] | 42.15 | 1.79 | 1.82 |
| 0.2 | (Ni _{0.07} Zn _{0.00} Fe _{0.93}) [Ni _{0.13} Zn _{0.80} Fe _{1.07}] | 16.68 | 0.72 | 0.82 |
| 0 | (Zn _{0.01} Fe _{0.99}) [Zn _{0.99} Fe _{1.01}] | 3.09 | 0.13 | 0.10 |

The Zn substitution dependent oxygen positional parameters and lattice constants are presented in Fig 4.20. By the increase of Zn content the oxygen positional parameter increases with concave down characteristic from 0.375 to 0.385. These relative values are consistent with the bulk values established above. The difference of these values from the ideal one is explained by small displacement of anions due to the expansion of the tetrahedral interstices [57].

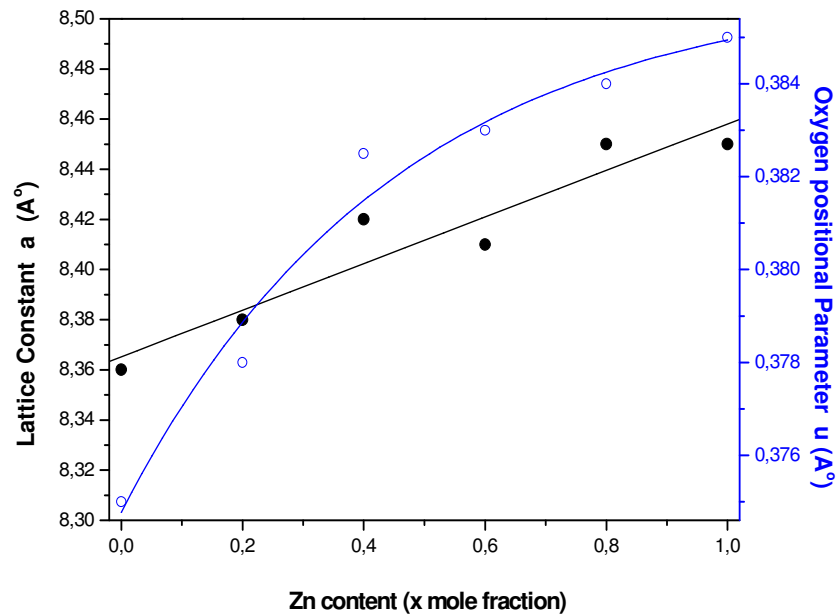


Figure 4.20 Variation of lattice parameter a (filled circles) and oxygen positional parameter: u (circles) with respect to the Zn content in $\text{Zn}_x\text{Ni}_{1-x}\text{Fe}_2\text{O}_4$ nanoparticles (from $x = 0$ to 1).

Sayed et al. reported that $\text{Zn}_x\text{Ni}_{1-x}\text{Fe}_2\text{O}_4$ samples have linear increase in the lattice constant from 8.362 to 8.442 Å in between $y = 0.1$ to 0.9 [46, 58]. In good agreement with this study, the linear increase in lattice constant from 8.38 to 8.45 Å by increasing zinc substitution is also observed as presented in Fig 4.20 and this is caused by the large ionic radius of Zn^{+2} (0.84 Å) as compared to Ni^{+2} (0.74 Å), [59].

4.4.3 TEM Micrographs of $Zn_xNi_{1-x}Fe_2O_4$ Nanoparticles with PEG 400

TEM micrographs of as-synthesized Ni-Zn ferrite nanoparticles with hydrothermal method by using PEG 400 as surfactant are given below and their particle size distributions is presented together, respectively. Size distributions are plotted with the TEM micrographs and discussed starting from $x = 0$ to 1.

4.4.3.1 $NiFe_2O_4$ Nanoparticles

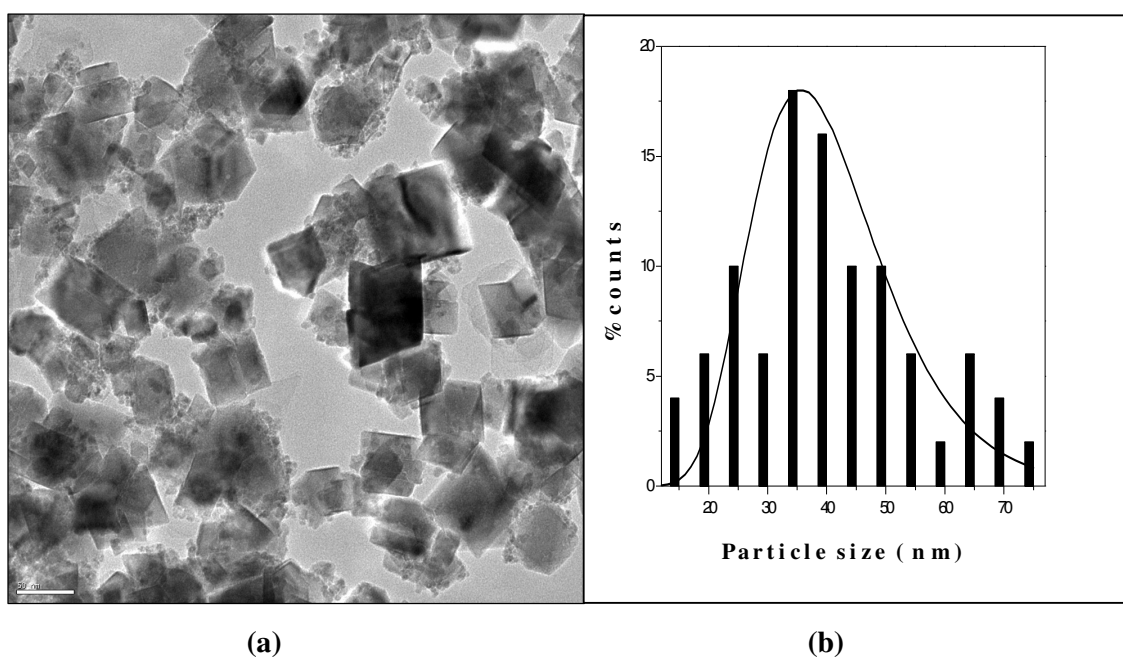


Figure 4.21 (a) The TEM micrograph of $NiFe_2O_4$ nanoparticles synthesized by using PEG 400, (b) particle size distribution.

The TEM micrograph and particle size distribution of $NiFe_2O_4$ nanoparticles synthesized by hydrothermal method using PEG 400 are given in Fig. 4.21. During synthesis, temperature was increased to $150\text{ }^{\circ}\text{C}$ and samples were kept for 21h in the oven. A good crystallinity can be attributed to the heat during synthesis process. The TEM micrograph of $NiFe_2O_4$ nanoparticles at 50 nm scale in Fig. 4.21 (a) is clearer than the microwave combustion method synthesized of $Zn_xNi_{1-x}Fe_2O_4$ nanoparticles. 15

particles are counted in NiFe_2O_4 nanoparticles and particle size has been determined as 35 nm from the size distribution from Fig.4.21 (b) which agrees with the result of XRD measurement (30 nm).

4.4.3.2 $\text{Zn}_{0.2}\text{Ni}_{0.8}\text{Fe}_2\text{O}_4$ Nanoparticles

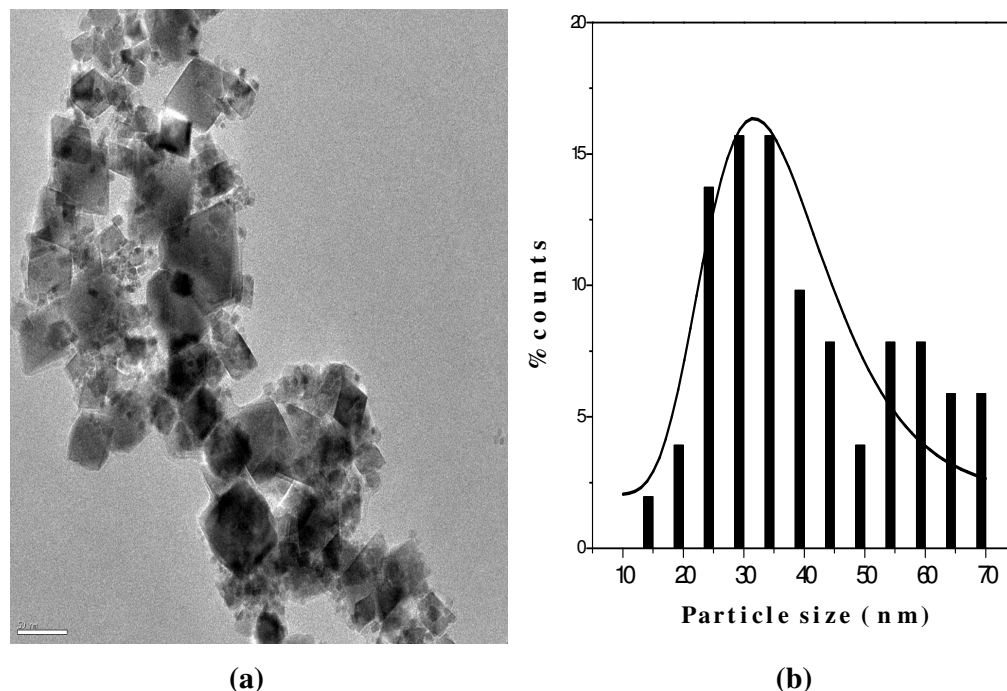


Figure 4.22 (a) The TEM micrograph of $\text{Zn}_{0.2}\text{Ni}_{0.8}\text{Fe}_2\text{O}_4$ nanoparticles synthesized by using PEG 400, (b) particle size distribution.

The TEM micrograph of $\text{Zn}_{0.2}\text{Ni}_{0.8}\text{Fe}_2\text{O}_4$ nanoparticles synthesized by using PEG 400 and their particle size distribution is given in Fig. 4.22. Crystalline structure is maintained itself at 50 nm scale again. There is no change in the type of shapes in Fig. 4.22, but size is different. XRD based measurement was 28 nm. 30 particles have been counted here and average particle size for $\text{Zn}_{0.2}\text{Ni}_{0.8}\text{Fe}_2\text{O}_4$ nanoparticles is observed as 33 nm. It can be seen that heat treatment provided better crystallinity in these samples.

4.4.3.3 $\text{Zn}_{0.4}\text{Ni}_{0.6}\text{Fe}_2\text{O}_4$ Nanoparticles

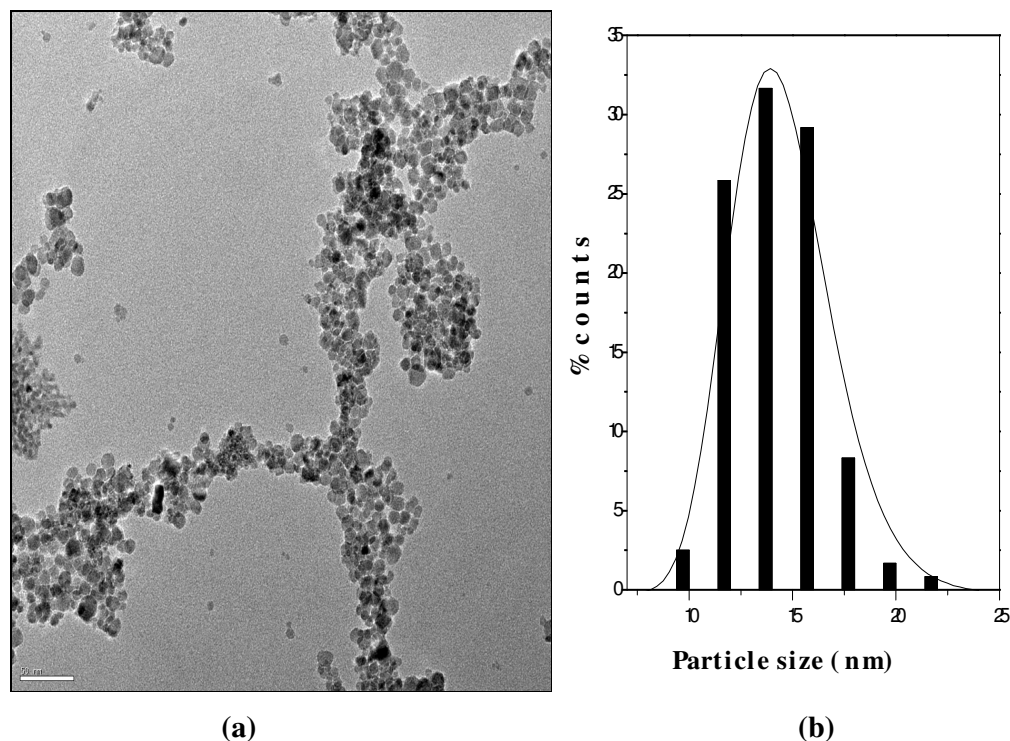


Figure 4.23 (a) The TEM micrograph of $\text{Zn}_{0.4}\text{Ni}_{0.6}\text{Fe}_2\text{O}_4$ nanoparticles synthesized by using PEG 400, (b) particle size distribution.

The TEM micrograph of $\text{Zn}_{0.4}\text{Ni}_{0.6}\text{Fe}_2\text{O}_4$ nanoparticles synthesized by using PEG 400 and their particle size distribution are given in Fig. 4.23. The biggest grain number that we obtained for our sample, was this one. 120 particles have been counted here. The average size is found as 15 nm from the size distribution of the $\text{Zn}_{0.4}\text{Ni}_{0.6}\text{Fe}_2\text{O}_4$ nanoparticles. This micrograph, (Fig. 4.23) has been taken in 50 nm scale. The XRD size of the sample was 13 nm that agrees with the TEM results. Many particles are accumulated in this micrograph which shows a broad line in XRD peaks. This sample was the easiest one to detect particles because of a crowded micrograph of the TEM grid.

4.4.3.4 $\text{Zn}_{0.6}\text{Ni}_{0.4}\text{Fe}_2\text{O}_4$ Nanoparticles

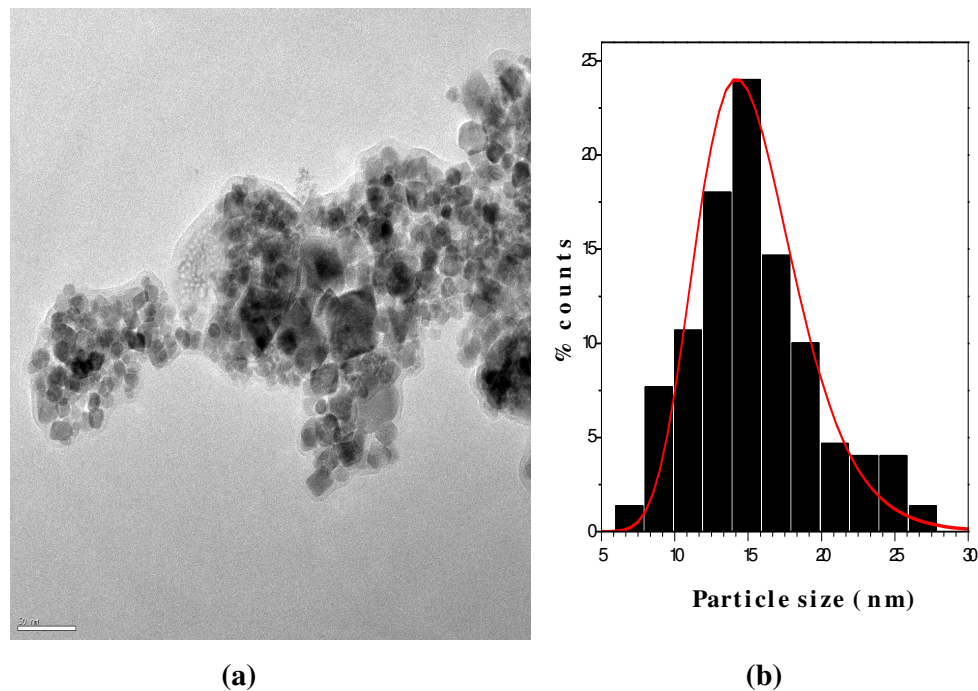


Figure 4.24 (a) The TEM micrograph of $\text{Zn}_{0.6}\text{Ni}_{0.4}\text{Fe}_2\text{O}_4$ nanoparticles synthesized by using PEG 400, (b) particle size distribution.

TEM micrograph of $\text{Zn}_{0.6}\text{Ni}_{0.4}\text{Fe}_2\text{O}_4$ nanoparticles are given in Fig. 4.24 (a). Their particle size distribution is presented in Fig. 4.24 (b). They have spherical shapes and their size is in the range of 7-27 nm, with almost a normal distribution centering around 15 nm except for some agglomerated particles. These agglomerates can increase the magnetic interaction between particles, and therefore may influence the magnetic properties of the product [23, 60]. Average particle size is calculated as $\sim 15 \pm 1$ nm (represented by dashed line in Fig. 4.24 (b)) from the TEM micrographs (at 50 nm scale) by counting a minimum of 75 nanoparticles. The XRD measurement of the particle was 14 nm which agrees with this result.

4.4.3.5 $\text{Zn}_{0.8}\text{Ni}_{0.2}\text{Fe}_2\text{O}_4$ Nanoparticles

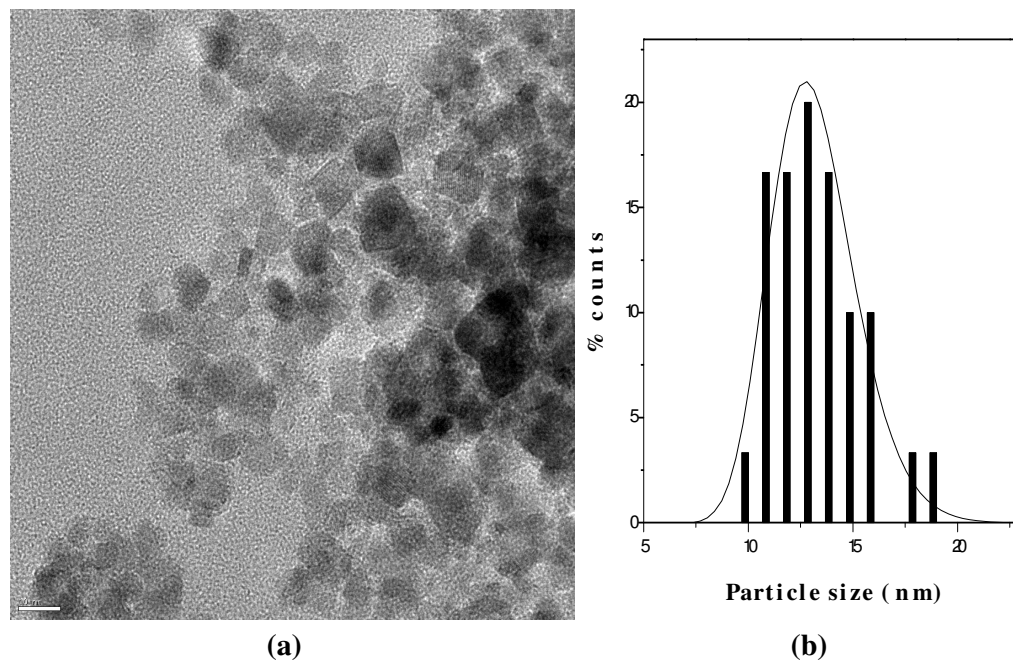


Figure 4.25 (a) The TEM micrograph of $\text{Zn}_{0.8}\text{Ni}_{0.2}\text{Fe}_2\text{O}_4$ nanoparticles synthesized by using PEG 400, (b) particle size distribution.

The distribution of the $\text{Zn}_{0.8}\text{Ni}_{0.2}\text{Fe}_2\text{O}_4$ nanoparticles in the TEM micrograph, in Fig. 4.25 (a), is obtained clearly here and helps us to identify nanoparticles easily at 10 nm scale. XRD size of the sample was 11 nm. This result agrees well with the size distribution of $\text{Zn}_{0.8}\text{Ni}_{0.2}\text{Fe}_2\text{O}_4$ nanoparticles in Fig. 4.25 (b). The highest bar is located at around 13 nm. Some dark areas prevent to distinguish particles, that's why there are a minority of particles which have different bars in size distribution graph.

4.4.3.6 ZnFe₂O₄ Nanoparticles

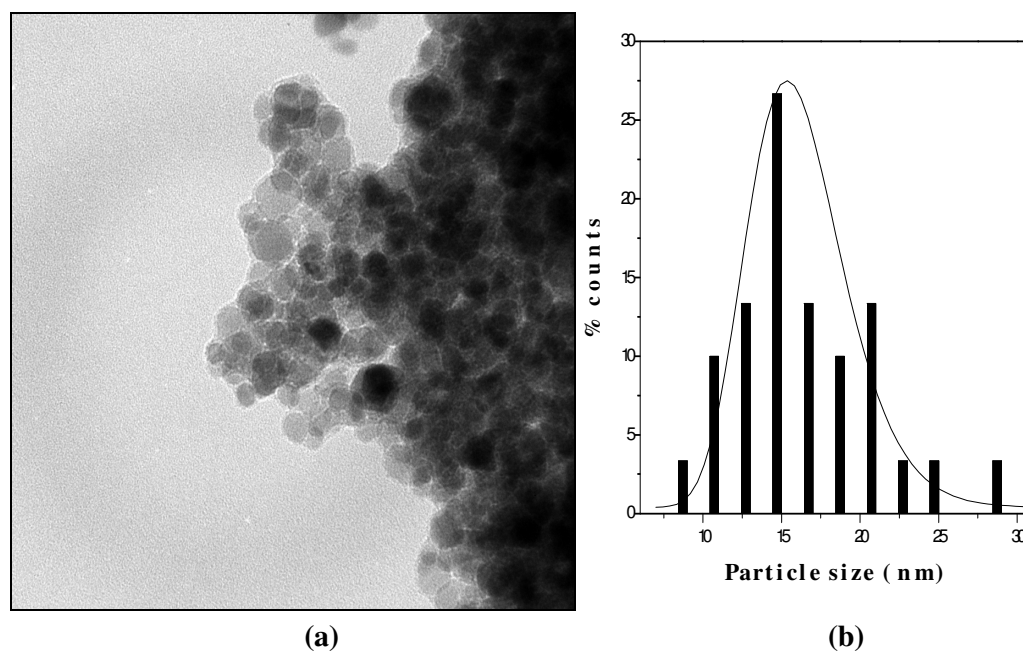


Figure 4.26 (a) The TEM micrograph of ZnFe₂O₄ nanoparticles synthesized by using PEG 400, (b) particle size distribution.

The TEM micrograph and particle size distribution of ZnFe₂O₄ nanoparticles synthesized by using PEG 400 are given in Fig. 4.26. It is expected that these nanoparticles will show Zn-ferrite properties in magnetic measurements. The TEM micrograph of the ZnFe₂O₄ nanoparticles at 50 nm scale is given in Fig. 4.26 (a). XRD size of particles is calculated as 14 nm. And here in Fig. 4.26 (b), distribution of the particles have spherical morphology and their size vary in the range of 7–21 nm, with almost a normal distribution and particle size can be read as 15 nm. Y.Köseoğlu et.al. [24] reported that PEG can increase the attraction among the polymer chains by coordination and cause the aggregation of nanoparticles (due to the rapid growth of nucleation) to larger diameter.

To determine the crystallite size distribution of the samples, the diffraction profiles were fitted according to the equation (4.1) in ref [61].

$$P(D) = \frac{A}{D\sigma_D\sqrt{2\pi}} \exp\left(-\frac{1}{2\sigma_D^2} \ln\left(\frac{D}{D_{TEM}}\right)^2\right) \quad (4.1)$$

where σ is the standard deviation of the diameter and D_{TEM} the average diameter obtained from TEM results.

All graphs are plotted and located together for comparison in Fig.4.27. The average particle sizes are found in the range of 13.1-37.3 nm by using eqn. 4.1 and results are listed in Table 4.8. Their size distribution histograms are fitted by using a log-normal function [62] and compared in the order of TEM, XRD and VSM:

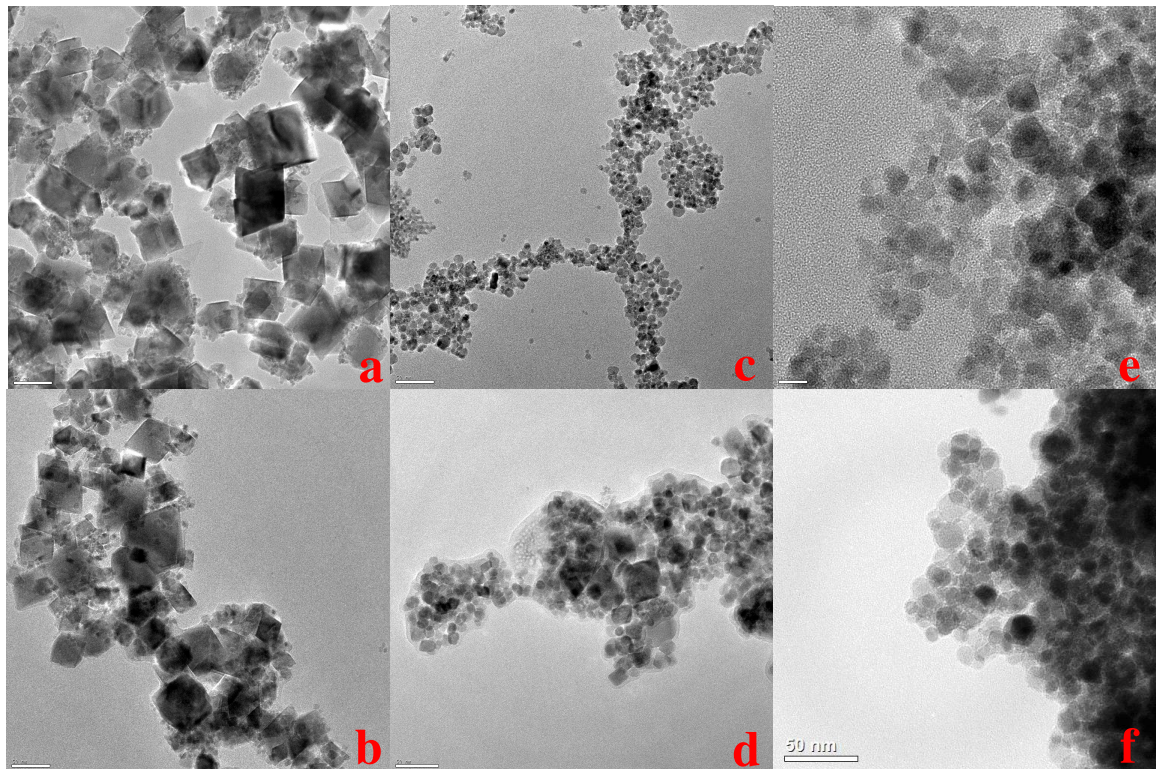


Figure 4.27 TEM micrographs of $Zn_xNi_{1-x}Fe_2O_4$ nanoparticles (a) $x=0$; (b) 0.2; (c) 0.4; (d) 0.6; (e) 0.8; (f) 1.0

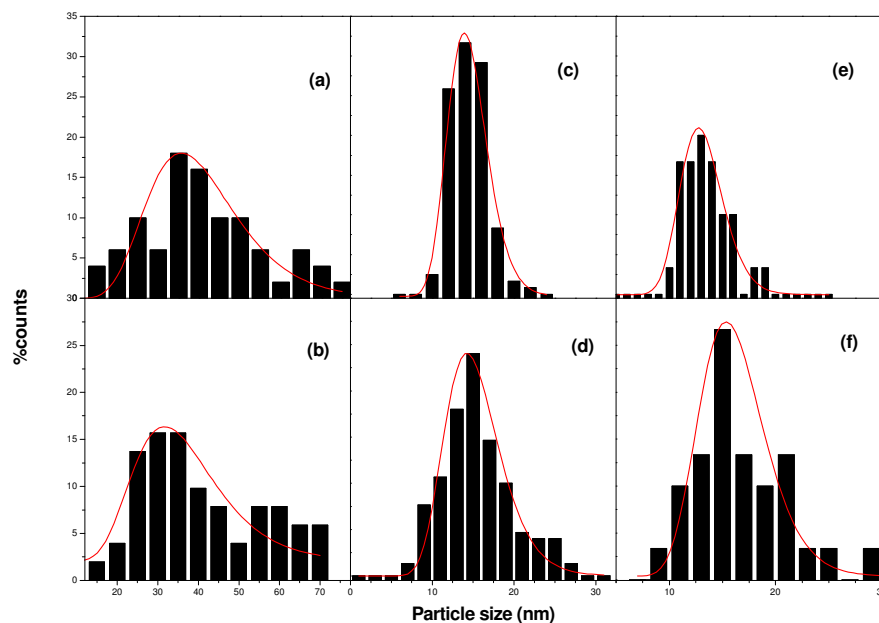


Figure 4.28 Histogram and log normal fits for $Zn_xNi_{1-x}Fe_2O_4$ nanoparticles (a) $x = 0$; (b) 0.2; (c) 0.4; (d) 0.6; (e) 0.8; (f) 1.

Table 4.8 The obtained particle sizes or size distributions of $Zn_xNi_{1-x}Fe_2O_4$ nanoparticles (from $x = 0$ to 1)

| Composition X | Size (nm) | | |
|------------------|--|---------------------------------------|--|
| | TEM | (XRD- Profile Fit) | VSM (LN Langevien Fit) |
| | $D_{TEM} (\sigma)$ Av. Size (Geo.StD) | $D_{XRD} (\sigma)$ Av. Size (StD.) | $D_m (\sigma_m)$ Av. Size (Geo .StD.) |
| 1 | 15 (0.20) | 12.1(4.2) | - |
| 0.8 | 13 (0.15) | 9.1 (1.5) | 8.8 (0.64) |
| 0.6 | 15 (0.23) | 14.1 (5.0) | 13.9 (0.58) |
| 0.4 | 14 (0.17) | 11.9 (4.0) | 11.9 (0.64) |
| 0.2 | 35 (0.32) | 26.0 (9.0) | 21.7 (0.55) |
| 0 | 37 (0.23) | 27.0 (7.0) | 19.6 (0.48) |

The sizes found from XRD are smaller than the sizes found from TEM as expected. These differences are caused from the coating effect which can be observed in TEM micrographs but can not be detected by XRD. The important point is that the agreement of distributions shows the reliability of size distribution results. In other words, what is widely distributed according to the TEM ($x = 0.8$) is widely distributed according to XRD too, likewise, narrow distribution according to the TEM ($x = 0.8$) is also narrowly distributed according to XRD. We can conclude that coating thickness over the samples is also distributed as the size of all samples.

4.4.4 Results of Magnetic Measurements for $Zn_xNi_{1-x}Fe_2O_4$ Samples Synthesized By Peg Assisted Hydrothermal Route

By using Quantum Design Vibrating Sample Magnetometer (QD-VSM), the magnetic characterizations of $Zn_xNi_{1-x}Fe_2O_4$ nanoparticles were performed. In detail, the magnetization of Ni-Zn ferrites were studied as a function of external field between ± 5 kOe and as a function of temperature (between $T=10$ K and the room temperature). Magnetic hysteresis curves were then analyzed for temperature dependency of the samples' magnetization under zero field cooling-ZFC and field cooling-FC.

4.4.4.1 NiFe₂O₄ Nanoparticles

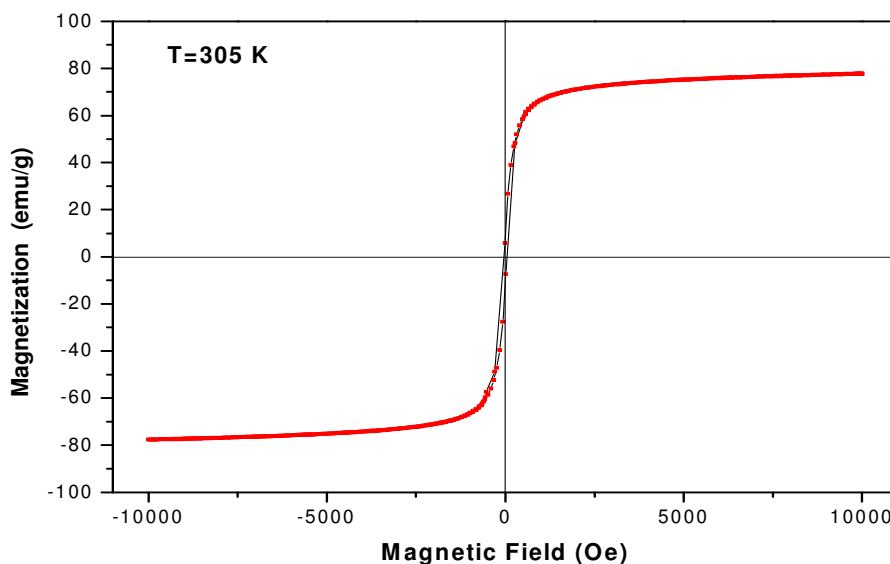


Figure 4.29 Magnetic field vs magnetization curve of NiFe₂O₄ synthesized by hydrothermal method using PEG 400 as surfactant at room temperature.

M-H curve of NiFe₂O₄ synthesized by hydrothermal method using PEG 400 as surfactant at room temperature at 10 KOe of applied magnetic field is given in Fig.4.29. The saturation magnetization is measured as 78 emu/g by extrapolating M vs. 1/H plot. When applied magnetic field is in 550 Oe regions, magnetization achieves a negative acceleration towards the origin. A tiny coercive field here is observed, which is measured 44 Oe. And then magnetization increases rapidly up to 60 emu/g after the origin. When the magnetic field is in 700 Oe regions, magnetization changes continuously. It increases with tiny amounts and it neither stops nor fulfills at a determined point of saturation magnetization as observed in earlier work [63].

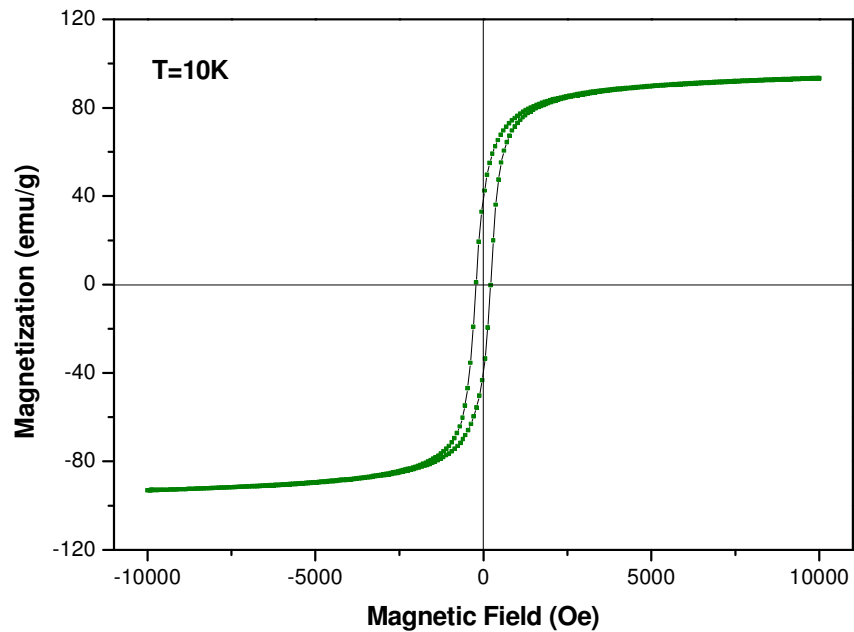


Figure 4.30 Magnetic field vs magnetization curve of NiFe_2O_4 synthesized by hydrothermal method using PEG 400 as surfactant at 10K.

The M-H curve of NiFe_2O_4 is measured at 10K as well. It is easy to perceive some changes. An increase in saturation magnetization is observed to the 94 emu/g value here, where applied magnetic field is 10 KOe. This value is higher compared with the room temperature M_s . By moving right at the scale, it is seen that curve has accelerated towards zero by indicating two arms starting from 1108 Oe point. Despite coercive field H_c seems larger than previous graph; it has a value of 212 Oe. After the origin, two lines rejoin at the 2023 Oe region of magnetic field. Remaining part of the graph demonstrates same behavior like room temperature observations.

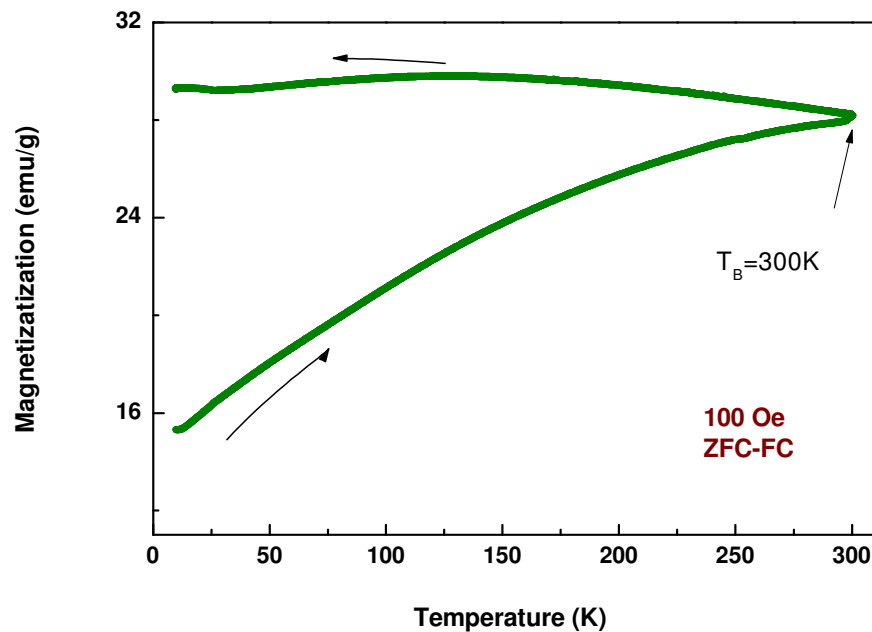


Figure 4.31 Magnetization vs temperature curve of NiFe_2O_4 synthesized by hydrothermal method using PEG 400 as surfactant.

Magnetization vs temperature curve of NiFe_2O_4 is obtained in a constant applied field of 100 Oe. Magnetization versus temperature curves for both zero-field cooled (ZFC) and field-cooled case (FC) in the measuring field were recorded. Resulting magnetization is plotted against temperature and it is seen that blocking temperature is at around $T_B = 300\text{K}$. However the curves diverge significantly when we compare ZFC and FC at lower temperatures. This can be usually seen in single domain particles [64]. First, particle is cooling by applying a magnetic field (100 Oe) starting from room temperature (FC). By decreasing temperature towards lower values, spins become frozen and protect their initial magnetizations. So it can be said that there should be a magnetization stored on domains. Measured value is about 29 emu/g. When external field is removed, thermal energy loses its dominant role by decreasing temperature and spins align randomly. At this time there isn't any factor to align them because spins are frozen again by providing a slight magnetization from the random distribution of spins. The amount of magnetization observed in ZFC is about 15 emu/g. That's why we can say that magnetization is lower than FC.

4.4.4.2 $\text{Zn}_{0.2}\text{Ni}_{0.8}\text{Fe}_2\text{O}_4$ Nanoparticles

The M-H curve of $\text{Zn}_{0.2}\text{Ni}_{0.8}\text{Fe}_2\text{O}_4$ synthesized by hydrothermal method using PEG 400 as surfactant at room temperature is given in Fig. 4.32.

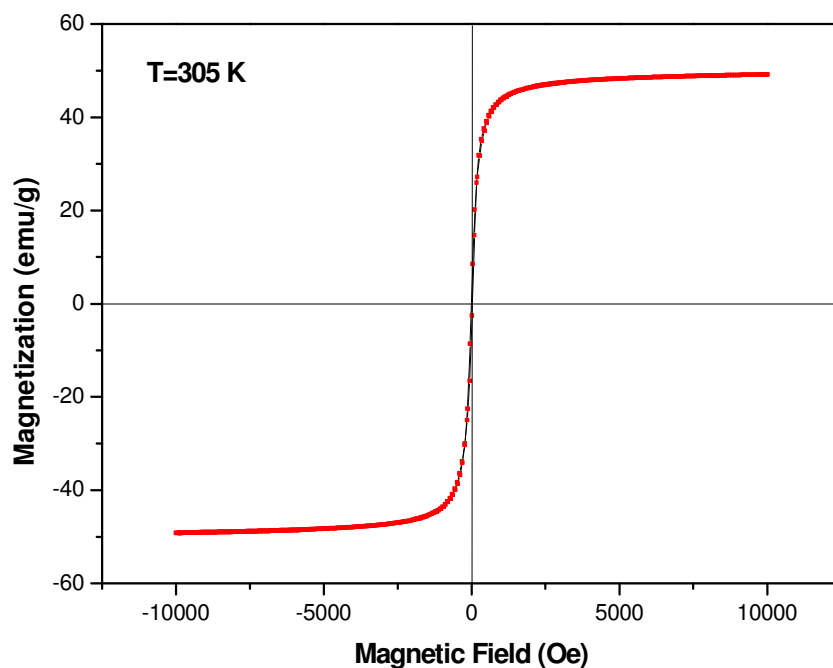


Figure 4.32 Magnetic field vs magnetization curve of $\text{Zn}_{0.2}\text{Ni}_{0.8}\text{Fe}_2\text{O}_4$ synthesized by hydrothermal method using PEG 400 as surfactant at room temperature.

The $\text{Zn}_{0.2}\text{Ni}_{0.8}\text{Fe}_2\text{O}_4$ nanoparticles under 10 kOe applied magnetic field have a magnetization of 49 emu/g which is lower than the first sample. It follows linear path up to 1710 Oe and starts to decrease. At origin it is observed that coercive field is measured as 16 Oe providing same descending trend like magnetization. A closer look to the magnetization curve after origin shows a sharp increase where as the remanent magnetization has not have a considerable value. After 1377 Oe , saturation magnetization is evident but not parallel to the magnetic field axis. Small increases of saturation magnetization of sample are measured up to 10 kOe and at this value M_s is

found to be 49.33 emu/g . The resulting magnetization is decreased in M_s and H_c which should be a evidence of Zn contribution to the structure. Because of non-magnetic nature of Zn, we aspected it to decrease the alignment of magnetic moments, magnetization and blocking temperature respectively.

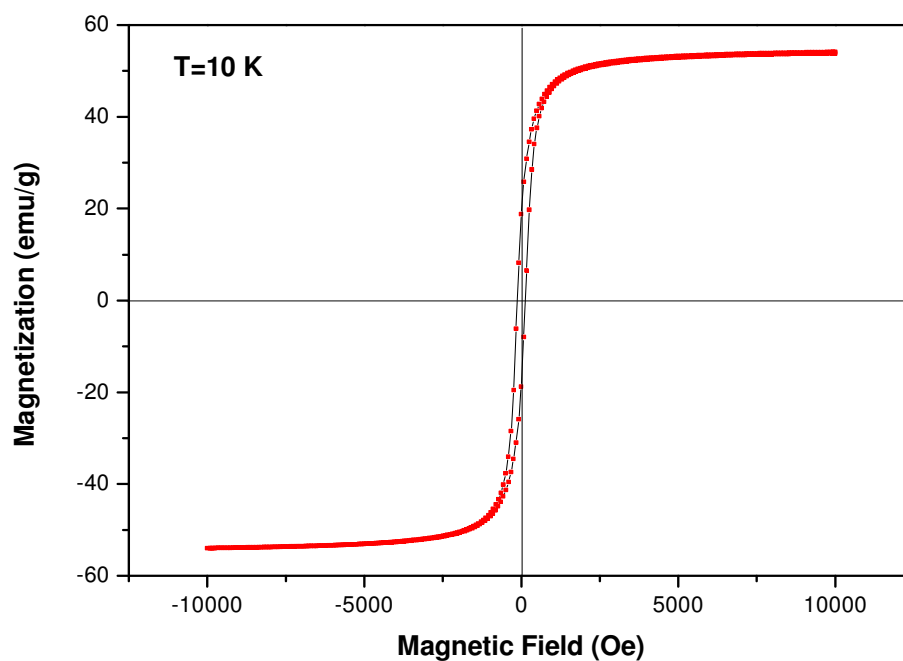


Figure 4.33 Magnetic field vs magnetization curve of Zn_{0.2}Ni_{0.8}Fe₂O₄ synthesized by hydrothermal method using PEG 400 as surfactant at 10K.

The M-H curve for Zn_{0.2}Ni_{0.8}Fe₂O₄ nanoparticles at 10K temperature, the saturation magnetization has a value of 54 emu/g which is higher compared with the previous one measured at room temperature. The curve is slightly increasing up to 1966 Oe field and then starting to decrease. Coercive field is measured as 129 Oe at the origin. Magnetization increases symmetrically by increasing applied field. After 1800 Oe the curve tends to increase linearly but slope of curve is observed. This means sample has not got a stable saturation magnetization.

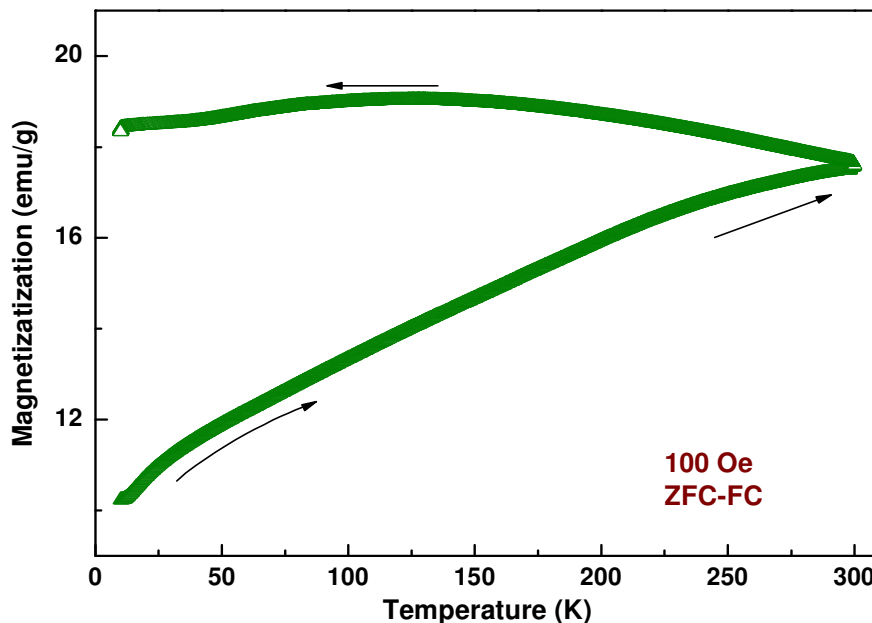


Figure 4.34 Magnetization vs temperature curve of $\text{Zn}_{0.2}\text{Ni}_{0.8}\text{Fe}_2\text{O}_4$ synthesized by hydrothermal method using PEG 400 as surfactant.

Field cooling (FC) and zero field cooling (ZFC) curves are demonstrated for $\text{Zn}_{0.2}\text{Ni}_{0.8}\text{Fe}_2\text{O}_4$ nanoparticles in the Fig. 4.34. Each curve forms a magnetic system separated an energy barrier like previous one. Here blocking temperature is determined as 300K . In ZFC process, sample is cooled without external applied field by decreasing temperature and magnetization is found to be 10.14 emu/g at 8 K which has been expected because of frozen spin magnetic moments. When a 100 Oe of applied field is turned on, cooling has started (FC), and when temperature was 8 K, magnetization is detected as 18.27 emu/g. The resulting magnetic moment of both curves differs only 8.13 emu/g from each other which is an evidence of thermal energy was dominant in FC process. Random distribution of spins in zero magnetic field has proved that the magnetization could not be observed without an external force which makes aligned the particles.

4.4.4.3 $\text{Zn}_{0.4}\text{Ni}_{0.6}\text{Fe}_2\text{O}_4$ Nanoparticles

Variation of magnetization (M-H curve) for $\text{Zn}_{0.4}\text{Ni}_{0.6}\text{Fe}_2\text{O}_4$ nanoparticles with the applied field at room temperature and at 10 K are plotted in Fig. 4.35 and Fig. 4.36 . The magnetization increases sharply by increasing the applied field in Fig. 4.35. Then it slowly increases by the field. M-H curve does not show hysteresis and does not reach to saturation even at 10 kOe applied field. The absence of saturation and coercivity at room temperature indicates the superparamagnetic nature of particles, which relax back their spins by rotation on removal of applied magnetic field so as to give a zero net magnetic moment. The room temperature saturation magnetization (obtained by extrapolating M vs. $1/H$ plot to $1/H = 0$) of the sample is found as 39.67 emu/g. A coercive field of 16 Oe was also observed.

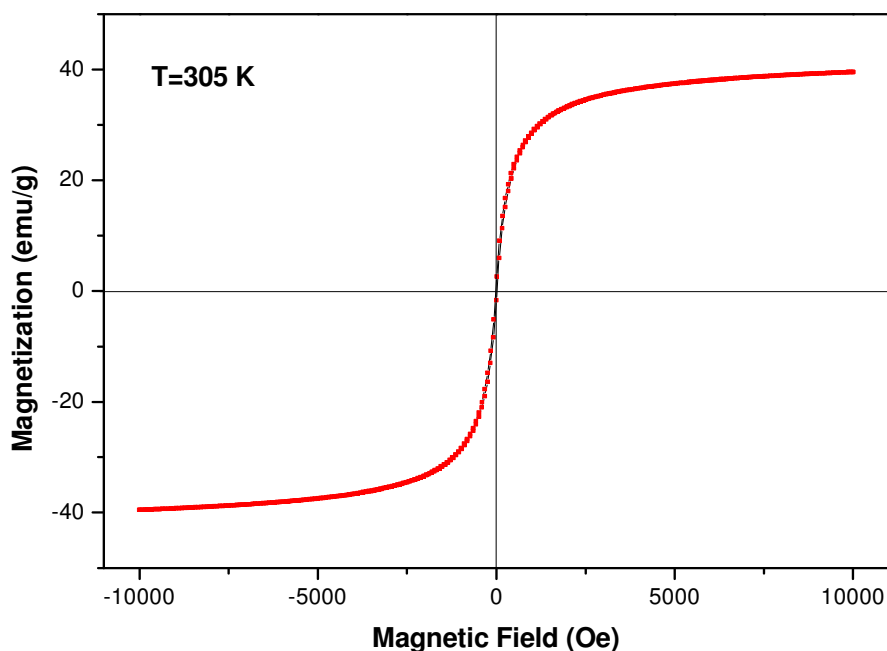


Figure 4.35 Magnetic field vs magnetization curve of $\text{Zn}_{0.4}\text{Ni}_{0.6}\text{Fe}_2\text{O}_4$ synthesized by hydrothermal method using PEG 400 as surfactant at room temperature.

Typical superparamagnetic 'S'-like shape of hysteresis curves (without open loops) were observed at high temperature region. Those 'S'-like shape loops can be divided into two parts: curvature parts and linear parts. The linear parts can be attributed to the antiferromagnetic phase of the sample, while the curvature parts may originate from the change of the inversion parameter induced by the preparation technique when the particle size decreases to the nanometer scale.

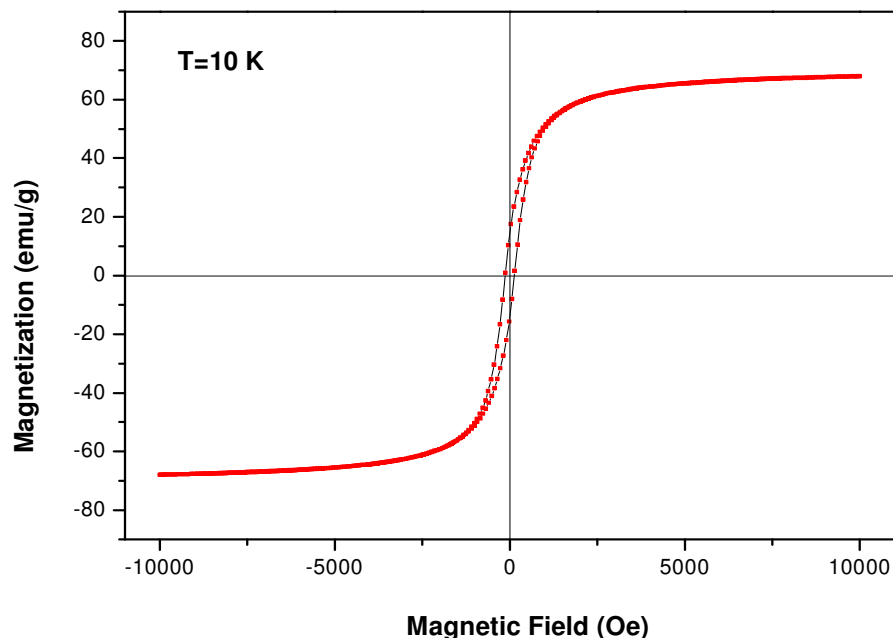


Figure 4.36 Magnetic field vs magnetization curve of Zn_{0.4}Ni_{0.6}Fe₂O₄ synthesized by hydrothermal method using PEG 400 as surfactant at 10K.

From M-H curve of Zn_{0.4}Ni_{0.6}Fe₂O₄ nanoparticles a saturation magnetization of 68 emu/g is observed at 10K which denotes magnetization is increased by decreasing temperature. Also a non-attainment of saturation is observed even at high applied magnetic fields. The magnitude of coercive field is measured as 132 emu/g at 10K temperature.

The temperature dependence of magnetization of Zn_{0.4}Ni_{0.6}Fe₂O₄ nanoparticles synthesized by hydrothermal method using PEG 400 as surfactant is given in Fig. 4.37.

as seen from the figure, the magnetization of the sample increases with decreasing temperature down to 150 K for both ZFC and FC cases. Below 148 K, while FC magnetization is increasing, the ZFC magnetization is decreasing by further decreasing the temperature. From this graph, the blocking temperature (T_B) of the sample can be determined as 148 K. Above the blocking temperature; both curves have the same values of magnetization. At room temperature, both ZFC and FC magnetizations have a value of about 10 emu/g. At blocking temperature, ZFC magnetization has a peak value of 12.6 emu/g. At 10 K, while the FC magnetization has a value of 14.2 emu/g, the ZFC magnetization has a value of 3.5 emu/g.

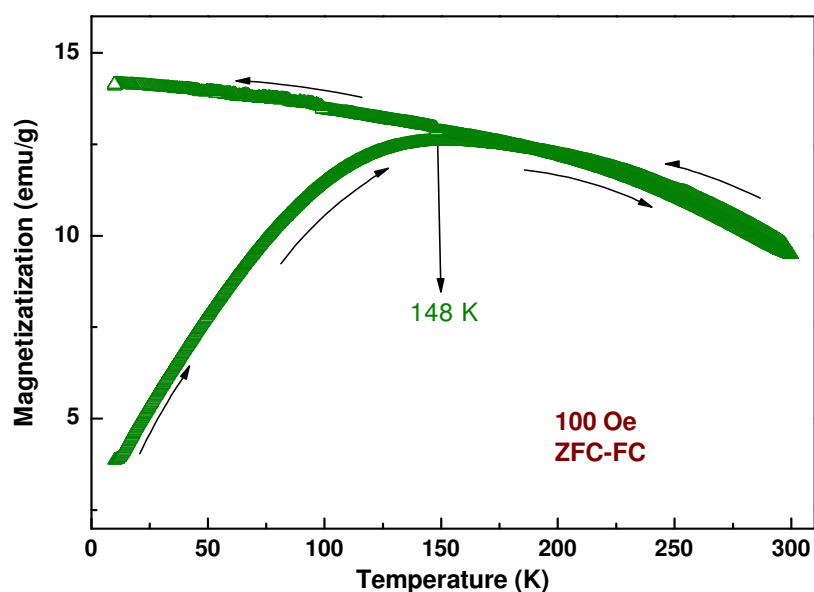


Figure 4.37 Magnetization vs temperature curve of $\text{Zn}_{0.4}\text{Ni}_{0.6}\text{Fe}_2\text{O}_4$ synthesized by hydrothermal method using PEG 400 as surfactant.

Below the blocking temperature, the particles do not have enough thermal energy to complete a thermal equilibrium with the exchange energy [64]. So it can be said that the low magnetization of particles in ZFC is based on the exchange interaction energy which keeps them aligned a little bit and makes us to observe it. While the $\text{Zn}_{0.4}\text{Ni}_{0.6}\text{Fe}_2\text{O}_4$ nanoparticles behave as superparamagnetic above the blocking temperature, they behave as ferromagnetic or ferrimagnetic below T_B .

4.4.4.4 $\text{Zn}_{0.6}\text{Ni}_{0.4}\text{Fe}_2\text{O}_4$ Nanoparticles

The magnetization curve of $\text{Zn}_{0.6}\text{Ni}_{0.4}\text{Fe}_2\text{O}_4$ nanoparticles synthesized by hydrothermal method using PEG 400 is analysed at room and 10 K temperature in Fig. 4.38 and 4.39.

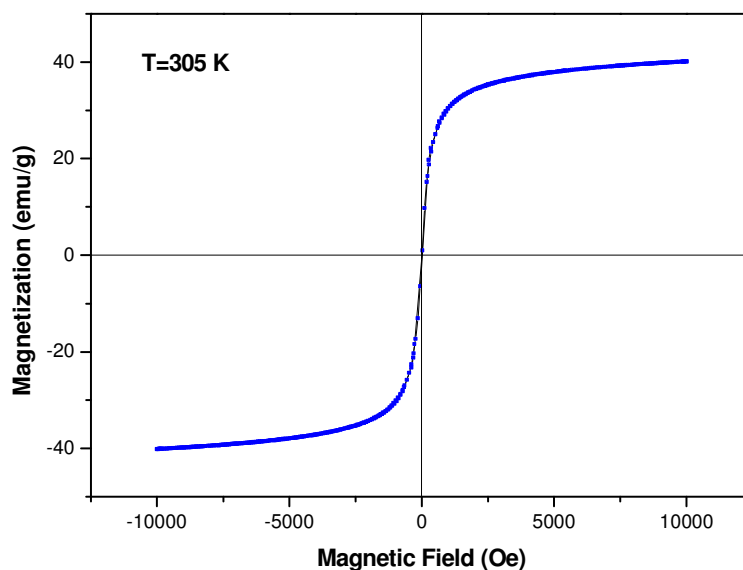


Figure 4.38 Magnetic field vs magnetization curve of $\text{Zn}_{0.6}\text{Ni}_{0.4}\text{Fe}_2\text{O}_4$ synthesized by hydrothermal method using PEG 400 at room temperature.

It is observed that the room temperature M-H curve of $\text{Zn}_{0.6}\text{Ni}_{0.4}\text{Fe}_2\text{O}_4$ powders does not show a hysteresis in Fig. 4.38. The value of magnetization sharply increases with the external magnetic field strength. M-H curve has an s shape at low field region and the high field side of the curve is almost linear with the external field [23]. However, a saturation state of magnetization has not been reached yet in the presence of a relatively strong magnetic field of even 10 kOe, which is consistent with the previous studies [60, 65]. A saturation magnetization of 40.3 emu/g is obtained for room temperature measurement. Zn ratio has 0.6 mol fraction in this sample so that it has been expected that coercive field and saturation magnetization values decreased again.

It is known that fine particles are easy to activate thermally and overcome magnetic anisotropy. Particles lost their hysteresis property above blocking temperature and magnetic moments follow the same direction with applied magnetic field. So the magnetic moments do not have any remanent magnetization and a hysteresis loop to observe coercive field.

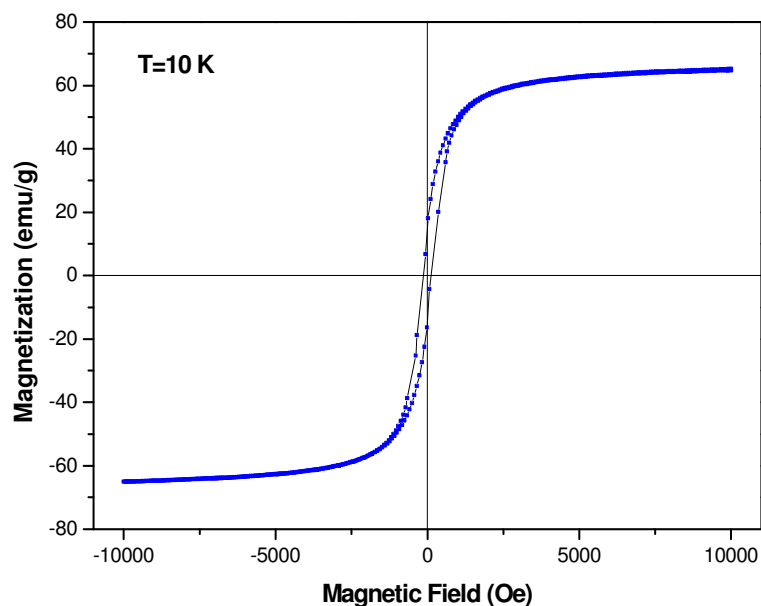


Figure 4.39 Magnetic field vs magnetization curve of Zn_{0.6}Ni_{0.4}Fe₂O₄ synthesized by hydrothermal method using PEG 400 as surfactant at 10K temperature.

The M-H curve of Zn_{0.6}Ni_{0.4}Fe₂O₄ nanoparticles denoted that coercive field and saturation magnetization increased at 10 K temperature in Fig. 4.39. Coercive field is measured as 132 Oe which is higher than 305K value. And saturation magnetization reached 65.35 emu/g because of the magnetic exchange energy. The width of hysteresis terminates around 50 emu/g values , after that a line follows a continuous shape by increasing applied field. An increasing trend in saturation magnetization is also observed in the high magnetic field regime.

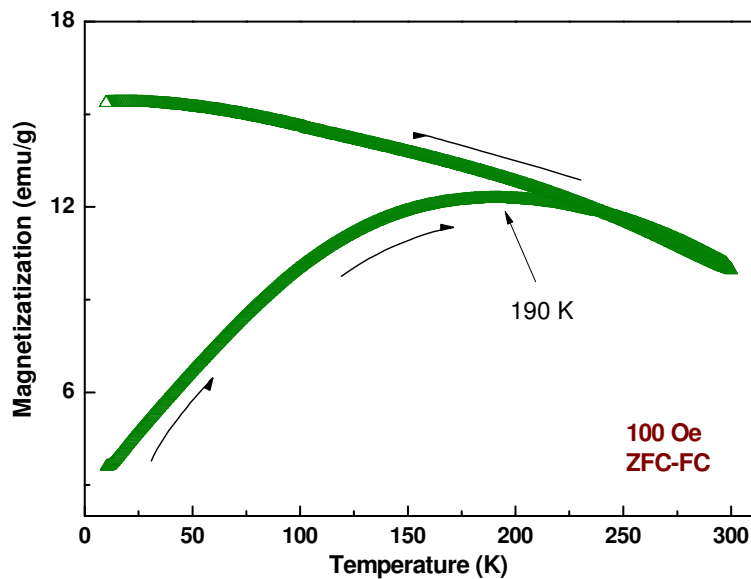


Figure 4.40 Magnetization vs temperature curve of $\text{Zn}_{0.6}\text{Ni}_{0.4}\text{Fe}_2\text{O}_4$ synthesized by hydrothermal method using PEG 400 as surfactant.

The magnetization vs temperature curve of $\text{Zn}_{0.6}\text{Ni}_{0.4}\text{Fe}_2\text{O}_4$ synthesized by hydrothermal method using PEG 400 as surfactant has been obtained in Fig. 4.40. The magnetization of the $\text{Zn}_{0.6}\text{Ni}_{0.4}\text{Fe}_2\text{O}_4$ sample increases by decreasing temperature in FC (field cooling) measurement. The magnetization of $\text{Zn}_{0.6}\text{Ni}_{0.4}\text{Fe}_2\text{O}_4$ nanoparticles at 10 K temperature is measured as 15 emu/g in FC process which means the magnetization direction of each particle is frozen in the field direction. The ZFC magnetization exhibits a maximum around a critical temperature which is blocking temperature T_B . Both curves, only joins at 190 K temperature only and then diverges. Here, T_B of $\text{Zn}_{0.6}\text{Ni}_{0.4}\text{Fe}_2\text{O}_4$ nanoparticles is can be said as 190 K in Fig. 4.40. After ZFC process magnetization of $\text{Zn}_{0.6}\text{Ni}_{0.4}\text{Fe}_2\text{O}_4$ nanoparticles is measured as 4 emu/g which denotes that the magnetic moments did not align at 10 K temperature.

4.4.4.5 $\text{Zn}_{0.8}\text{Ni}_{0.2}\text{Fe}_2\text{O}_4$ Nanoparticles

The hysteresis curve of $\text{Zn}_{0.8}\text{Ni}_{0.2}\text{Fe}_2\text{O}_4$ nanoparticles synthesized by hydrothermal method using PEG 400 at room temperature is given in Fig. 4.41. The rapid increase of magnetization draws a line with a huge slope. Here the curve seems like an ideal “s” shape of a superparamagnetic substance, so no coercive force is obtained. The saturation magnetization, M_s , of the sample is about 17 emu/g obtained by extrapolating M vs. $1/H$ again.

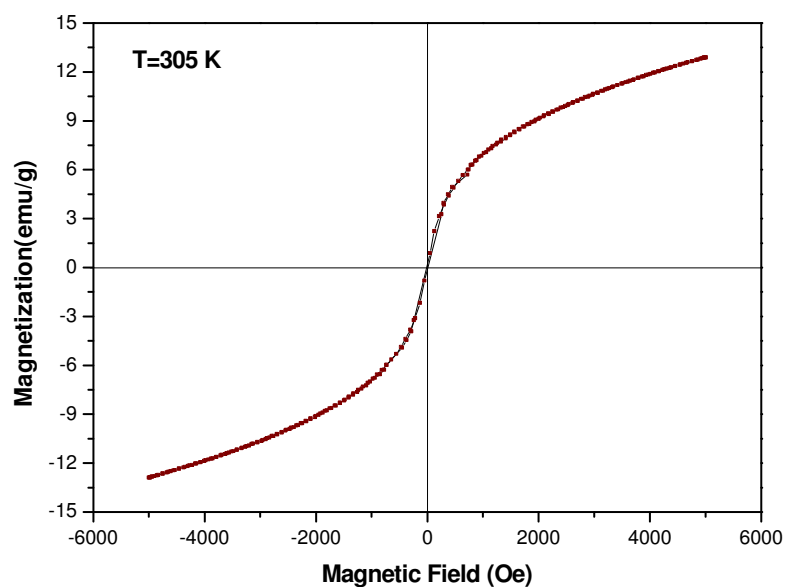


Figure 4.41 Magnetic field vs magnetization curve of $\text{Zn}_{0.8}\text{Ni}_{0.2}\text{Fe}_2\text{O}_4$ synthesized by hydrothermal method using PEG 400 as surfactant at room temperature.

This value of saturation magnetization is very low compared with the previous ones due to %80 mole percent of Zn contribution. Because, magnetization of ferrites were strongly dependent to the cation distribution in octahedral and tetrahedral sites, the dominant role of the Zn cations are expected in this sample. The ratio of Ni atoms is very low and it may not be enough to obtain aligned magnetic moments for this sample.

And this situation will cause to change saturation magnetization, coercive force, remanent magnetization and blocking temperature.

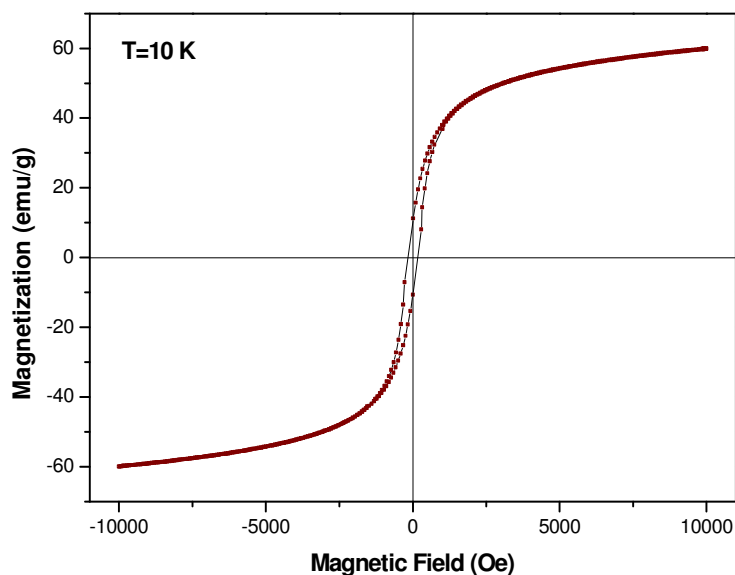


Figure 4.42 Magnetic field vs magnetization curve of $Zn_{0.8}Ni_{0.2}Fe_2O_4$ synthesized by hydrothermal method using PEG 400 as surfactant at 10K temperature.

Magnetization measurements for samples at 10 kOe applied field showed that saturation magnetization increased to the 60.16 emu/g value. A coercive field of 167 Oe is observed for the $Zn_{0.8}Ni_{0.2}Fe_2O_4$ nanoparticles, as well. The curve after origin is unsaturated and its slope increases even at high magnetic fields. But a coercive field can easily be observed by decreasing temperature to 10K. Thermal energy is not dominant here and just the energy of magnetic moments exists. Field and zero field cooling graphs of sample will provide us more information.

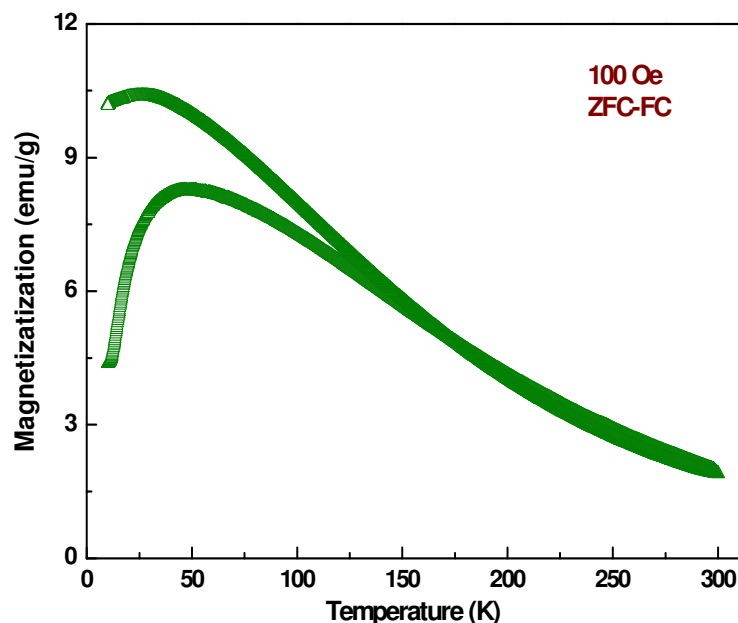


Figure 4.43 Magnetization vs temperature curve of $\text{Zn}_{0.8}\text{Ni}_{0.2}\text{Fe}_2\text{O}_4$ synthesized by hydrothermal method using PEG 400 as surfactant.

Magnetization vs temperature curve of $\text{Zn}_{0.8}\text{Ni}_{0.2}\text{Fe}_2\text{O}_4$ samples is plotted in Fig. 4.43 for both ZFC and FC measurements. The field cooling is started from 300 K. When the temperature is decreased down to 150 K, an almost linear increase in magnetization has been observed for both FC and ZFC cases. Below 150 K, the curve divides itself into two parts. This temperature is called as irreversibility temperature (T_{irr}) [66, 67]. Actually, downside part is called as zero field cooling (ZFC) curve and upper part is called as FC curve. Because, in FC curve the applied magnetic field causes the magnetization to increase. At 25 K, the FC magnetization is at its highest point and its value is 10.54 emu/g. The ZFC curve reaches its highest value of 8.4 emu/g at around 50 K. So, this temperature is called as the blocking temperature of the sample. This small alignment of magnetic moments occurs spontaneously because of spins' own magnetic exchange energy. Temperature is low so that thermal energy is not active here below 50 K. Above T_{B} , the magnetization decreases by the temperature and it has a value of about 2.25 emu/g at room temperature. At zero kelvin we expect that the

magnetic moments of atoms has no alignment, because spins froze at absolute temperature.

4.4.4.6 ZnFe₂O₄ Nanoparticles

This sample is totally zinc ferrite and we expect it to have minimum magnetization. The Fig. 4.44 shows the room temperature M-H curve which is like a straight line and a small deviation at origin was observed. Magnetization of the sample does not reach a saturation state even at an applied field of 10 kOe and it does not have any coercive field. Just an increasing trend can be observed towards high magnetic fields. Nonsaturation in magnetization and no coercivity at room temperature indicates that the substance is superparamagnetic at this temperature.

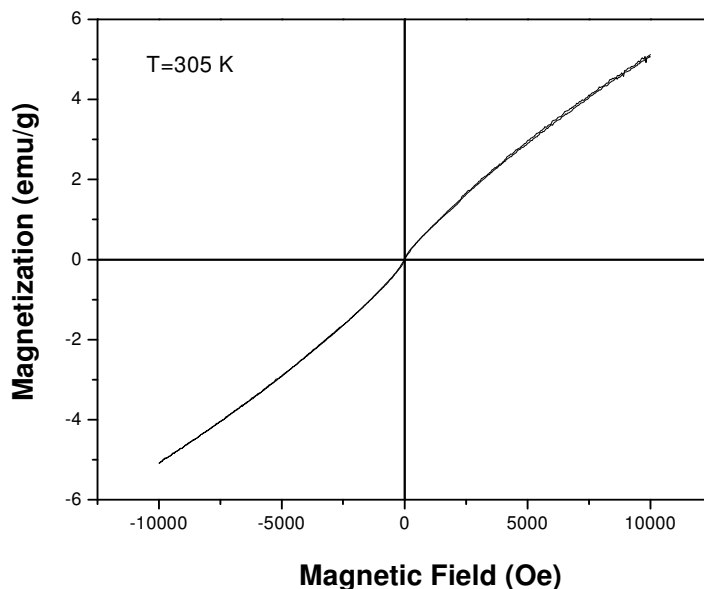


Figure 4.44 Magnetic field vs magnetization curve of ZnFe₂O₄ synthesized by hydrothermal method using PEG 400 as surfactant at room temperature.

Both sides of the curve show a value of magnetization less than 6 emu/g at ± 10 kOe applied field. The saturation magnetization, M_s , at room temperature is nearly 5 emu/g. Typical superparamagnetic “s” shape of hysteresis curve (without open loops) was observed at high temperature region. When the temperature is decreased the magnetization of the sample increases as seen in Fig. 4.45. An M-H curve with a small open hysteresis without saturation is observed.

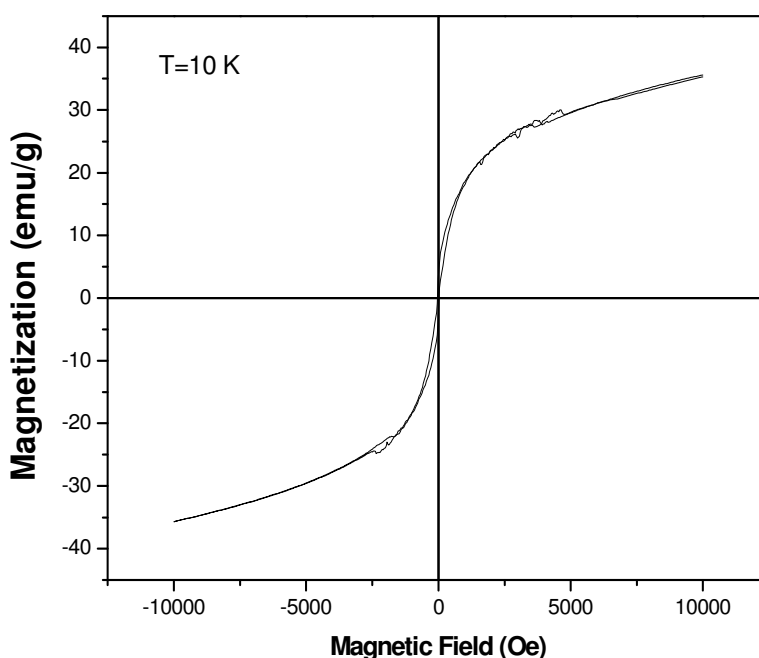


Figure 4.45 Magnetic field vs magnetization curve of ZnFe₂O₄ synthesized by hydrothermal method using PEG 400 as surfactant at 10K temperature.

At 10K, the M-H curve of ZnFe₂O₄ nanoparticles is closer to the hysteresis curve. A coercive field 40 Oe is measured at lowest temperature. The value of magnetization sharply increases with the external magnetic field strength starting from the origin at low field region and, however, it can not reach a saturation state yet in the presence of a relatively strong magnetic field of even 10 kOe. The saturation magnetization, M_s , obtained from M vs. 1/H graph is 37 emu/g. Some small step like deviations are

observed and it can be resulted from the vibration of the sample holder in VSM device . In both sides of the curve, 2500 -3000 Oe regions lost their continuous trend and have small fluctuations in the values of applied field and magnetization.

At different temperatures, M-H curves of ZnFe_2O_4 nanoparticles synthesized by PEG 400 assisted hydrothermal method are given in Fig. 4.46. The magnetic hysteresis curves were recorded by sweeping the external field between ± 10 kOe at different temperatures as well. As can be seen from the figure, the value of magnetization sharply increases with the external magnetic field strength at low field region and, however, it can not reach a saturation state yet in the presence of a relatively strong magnetic field of even 10 kOe, which is consistent with the earlier works [60]. The high field side of the curves is almost linear with the external field. The measured value of saturation magnetization decreases with increasing temperature as well. This behavior implies the co-existence of ferromagnetic and antiferromagnetic interactions. The non-saturated magnetization suggests the existence of strong antiferromagnetic inter-cluster interactions mixed with ferromagnetic interactions inside the clusters [65, 68]. This (co-existence of ferromagnetic and antiferromagnetic) can also cause the canted spin structures inside the clusters. By increasing the applied field, the ferromagnetic part tends to saturate, where as the antiferromagnetic part increases linearly, resulting in lack of saturation of magnetization even at 10 kOe magnetic field.

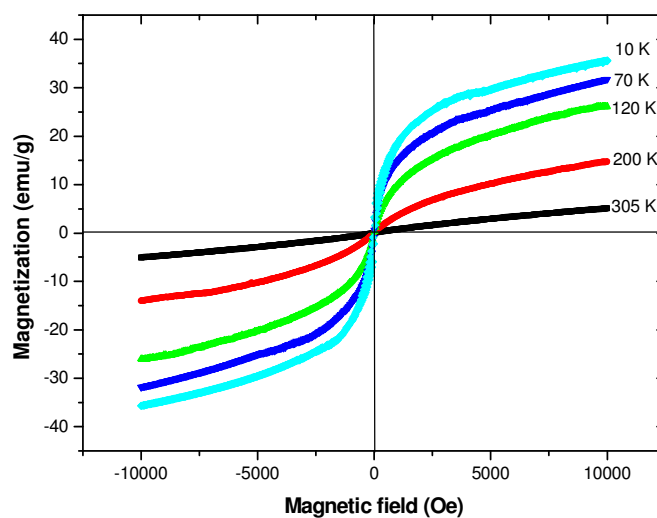


Figure 4.46 Magnetic hysteresis loops of ZnFe_2O_4 nanoparticles at different temperatures.

'S'-like shape of hysteresis curves (without open loops- coercive forces are zero) indicating typical superparamagnetic behavior were observed at high temperature region. Those 'S'-like shape loops can be divided into two parts: curvature parts and linear parts. While the curvature parts may originate from the change of the inversion parameter induced by the preparation technique when the particle size decreases to the nanometer scale, the linear parts can be attributed to the antiferromagnetic phase of the sample [60].

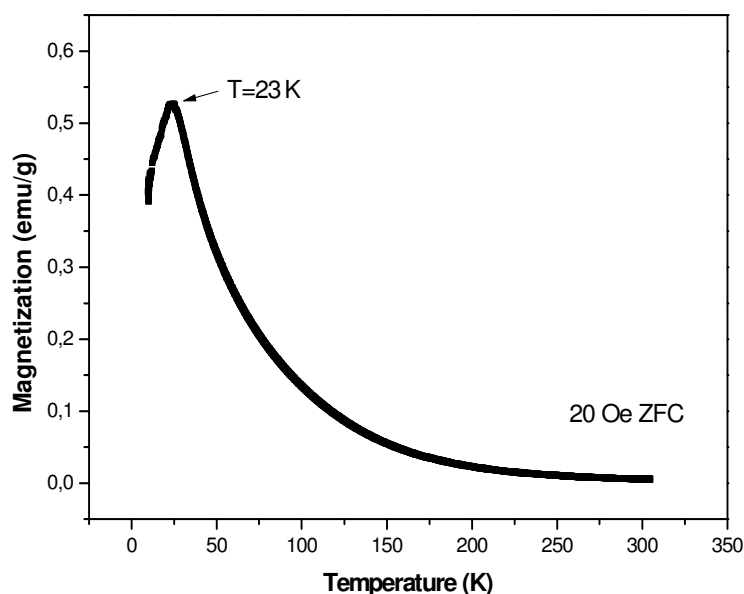


Figure 4.47 ZFC M-T curve of ZnFe_2O_4 nanoparticles with applied field of 20 Oe.

The ZnFe_2O_4 samples were cooled either in the presence of an external magnetic field (Field cooling case-FC) or in zero field (Zero field cooling case-ZFC) to measure temperature dependence of magnetization.

Fig. 4.47 and Fig. 4.48 display the M-T curves of the sample at the applied field of 20 Oe (ZFC) and 1 kOe (FC), respectively. For ZFC curve, while the magnetization increases with decreasing temperature down to 23 K, it exhibits a maximum at around 23 K and start to decrease below this temperature. The decrease in magnetization below this temperature may indicate that there are strong antiferromagnetic inter-cluster

interactions between the particles [65, 68, 69]. In the case of the FC curve with 1 kOe magnetic field applied, the peak (kink) shifts down to about 16 K, which can be attributed to the magnetic ordering of clusters resulting a decrease of spin-canting with increasing the applied field [70].

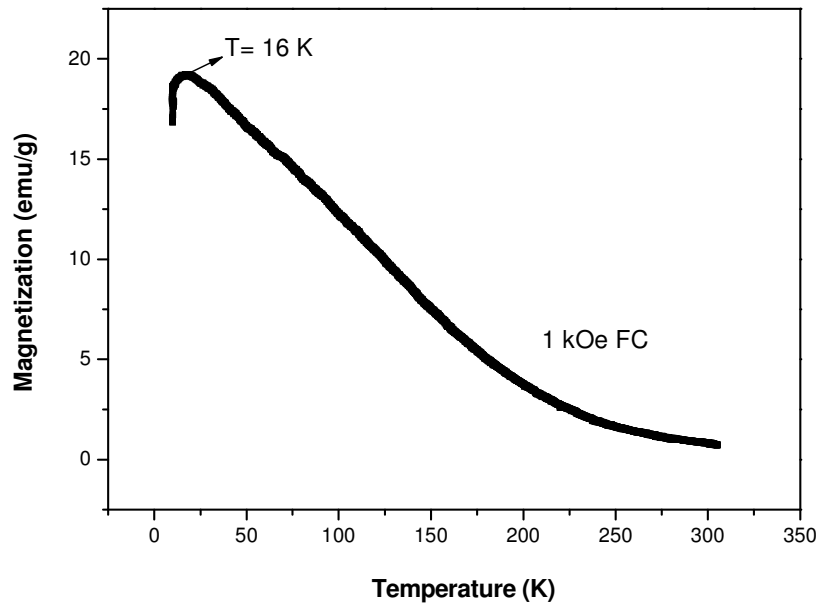


Figure 4.48 FC M-T curve of ZnFe_2O_4 nanoparticles with applied field of 1 kOe.

In another way, the decrease in magnetization at higher temperatures and linear increase with external field could be explained with super-paramagnetic response of individual magnetic clusters that can be ferro-magnetic or ferrimagnetic in nature. In this view, un-compensated spins of antiferromagnetic clusters give rise to finite and giant effective spins that response to external field like super-paramagnetic systems [24]. However, since there is antiferromagnetic interaction both in intra-clusters and interclusters spins, and size (effective moment) distribution of the particles, the resultant overall magnetic behavior would naturally be expected to be considerably different than that of conventional super-paramagnetic systems. This results support predictions of Oliver and Chinnasamy et al. for spin-glass-like behavior for nanosized ZnFe_2O_4 particles [24, 71-73].

As a result, for the samples synthesized by PEG assisted hydrothermal method, the magnetic behaviors of the samples strongly change by Zn content. Zn content vs blocking temperature graph of $Zn_xNi_{1-x}Fe_2O_4$ synthesized by hydrothermal method using PEG 400 is given in Fig. 4.49. The blocking temperatures of the samples are decreasing by the Zn content as observed in earlier work [74]. Cationic stoichiometry and the site occupancy of Zn ions may influence the blocking temperature.

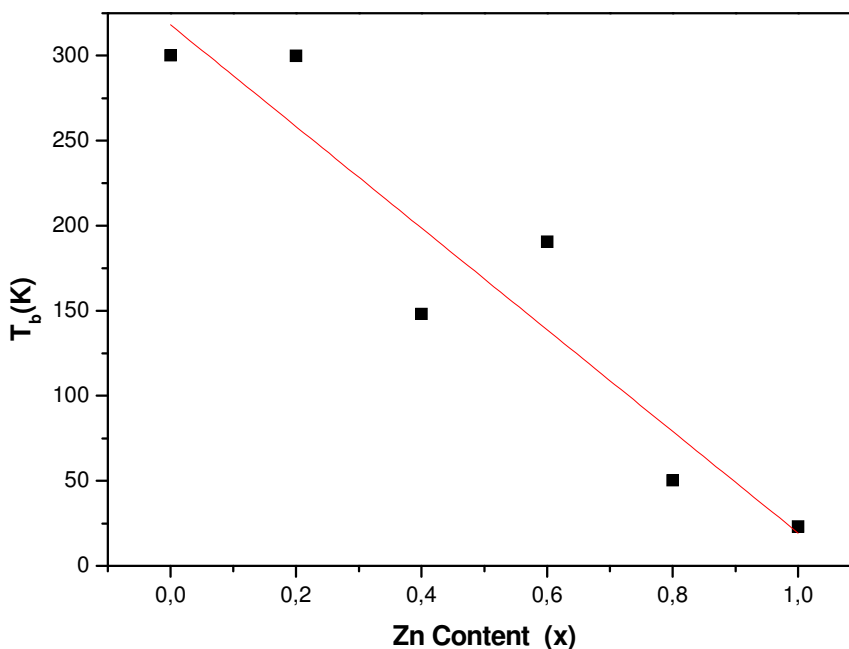


Figure 4.49 Zn content vs blocking temperature graph of $Zn_xNi_{1-x}Fe_2O_4$ synthesized by hydrothermal method using PEG 400.

For a cubic system of a spinel, the magnetic order is mainly belongs to a superexchange interaction between A and B sites. The substitution of non-magnetic Zn ion denotes the decrease of exchange interactions between A and B sublattices. That's why the magnetic properties of ferrites decrease by Zn content and magnetic properties of fine nanoparticles can be varied by Zn addition as it can be seen from the Table 4.9.

Table 4.9 Mean particle diameter and magnetic parameters with an applied magnetic field of $Zn_xNi_{1-x}Fe_2O_4$ nanoparticles synthesized using PEG 400.

| Compound | Mean Diameter D (nm) | H_c (Oe) (at 305K) | M_s (emu/g) (at 305K) | H_c (Oe) (at 10K) | M_s (emu/g) (at 10K) | T_B (K) |
|---------------------------|---------------------------|---------------------------|------------------------------|--------------------------|-----------------------------|-----------|
| $NiFe_2O_4$ | 35.15 | 44 | 77.94 | 212 | 93.55 | 300.06 |
| $Zn_{0.2}Ni_{0.8}Fe_2O_4$ | 33.18 | 16 | 49.33 | 129 | 54.38 | 299.99 |
| $Zn_{0.4}Ni_{0.6}Fe_2O_4$ | 15.46 | 16 | 39.67 | 132 | 68.21 | 148.21 |
| $Zn_{0.6}Ni_{0.4}Fe_2O_4$ | 19.07 | 12 | 40.25 | 132 | 65.35 | 190.54 |
| $Zn_{0.8}Ni_{0.2}Fe_2O_4$ | 13.32 | 6 | 16.64 | 167 | 60.16 | 50.18 |
| $ZnFe_2O_4$ | 14.35 | 0 | 5.12 | 40 | 35.65 | 23.00 |

Fig. 4.50 shows the room temperature magnetic hysteresis of $Zn_xNi_{1-x}Fe_2O_4$ nanoparticles synthesized by PEG assisted hydrothermal method.

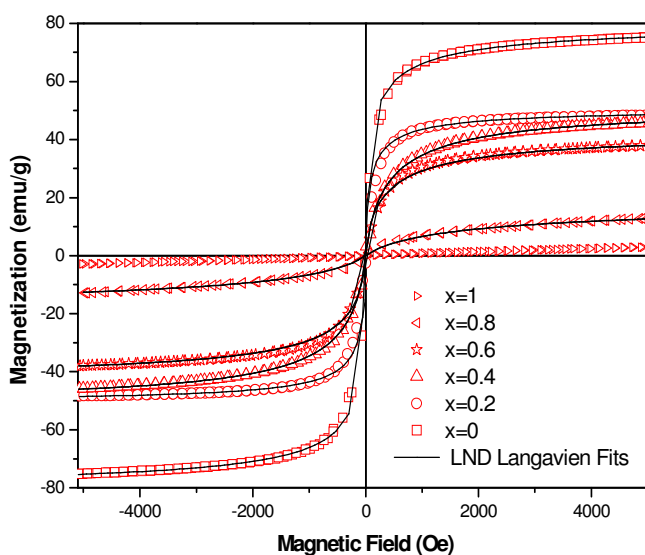


Figure 4.50 M vs H curves at room temperature and their size weighted Langevian fits

At room temperature the magnetization curves have non-hysteretic behaviour and not saturated even at 5 kOe applied field. And this effect is called as superparamagnetic behavior except for Zn-ferrite ($x = 0$).

The curves for $x = 0.2 - 1.0$ are well fitted with the size distributed Langevien function [75]:

$$M(D, H) = \sum M_i V_i f(d_i) L(x_i) \quad (4.5)$$

where M_i and V_i , magnetization and volume of i^{th} particle, and $f(d_i)$ is the log-normal function of $f(d_i) = 1/(\sqrt{2\pi} \ln \sigma_m) \exp(-(\ln d - \ln d_m)^2 / 2 \ln \sigma_m^2)$ depends on the statistical median d_m and geometric standart deviation of σ_m , and $L(x_i) = \coth(x_i) - 1/x_i$ with $x_i = M_i H V_i / kT$. It is noted that the parameter d_m is not the average diameter. The average diameter from magnetic measurement, which is denoted as D_m (Table 4.7), hereafter, is expressed as the avrage diameter and is obtained by

$$D_m = \frac{\sum d_i f(d_i)}{n} \quad (4.6)$$

The magnetic sizes are found in between 8.76 and 21.66 nm and all d_m , σ_m and D_m tabulated in Table 4.9. And, the size distribution results from magnetic measurements were also presented in Table 4.7 again to compare the results with XRD results.

The sizes found from VSM belong to the magnetic core of the samples and does not include the outer parts. So the magnetic dead layers, both the coating part and the non magnetic surface between core and the coating, can not be detected by the magnetic measurements.

Table 4.10 Statistical median size (d_m), geometric standard deviation (σ_m) and average diameter (D_m) of $Zn_xNi_{1-x}Fe_2O_4$ nanoparticles ($x = 0$ to 1) obtained from magnetization measurements.

| Composition x | VSM size distributions | | | |
|------------------|------------------------|-------|------------|-------|
| | Ms(emu/g) | d_m | σ_m | D_m |
| 0 | 80.45 | 9.0 | 0.48 | 19.6 |
| 0.2 | 50.56 | 12.8 | 0.55 | 21.66 |
| 0.4 | 51.14 | 8.8 | 0.64 | 11.86 |
| 0.6 | 42.80 | 8.9 | 0.58 | 13.88 |
| 0.8 | 18.64 | 6.5 | 0.64 | 8.76 |
| 1 | - | - | - | - |

The sizes calculated by VSM are found to be smaller than the XRD and TEM results. It is observed that there is a good agreement in the relative sizes of samples obtained by VSM, XRD, and the TEM. Here the fluctuated size distributions (StD) may be caused that the size is not only effected by magnetization, also cation disorder, small inter particle and intra particle interactions affect the magnetization.

Table 4.10 also includes the values of saturation magnetization at room temperature, and by using these values the magnetic moment per formula unit in Bohr magneton was calculated using the following equation [53]:

$$n_B = \frac{M \cdot wt \times M_s}{5585} \quad (4.7)$$

The low temperature hysteresis curves still have small increase in magnetization at relatively high field of 5kOe (Fig 4.49). This tendency of saturation magnetizations are analyzed by the extrapolation to the intercepts of the magnetization axes in magnetization versus reciprocal of magnetic field, then saturation magnetization values are taken and the remanance magnetization values are directly taken from the M vs H graph.

Figure 4.51 shows the M-H curves for $Zn_xNi_{1-x}Fe_2O_4$ nanoparticles for $x = 0.0-1.0$ measured at 10 K. As it is observed from the figure, the magnetization and the coercivity of the samples decrease by the Zn content.

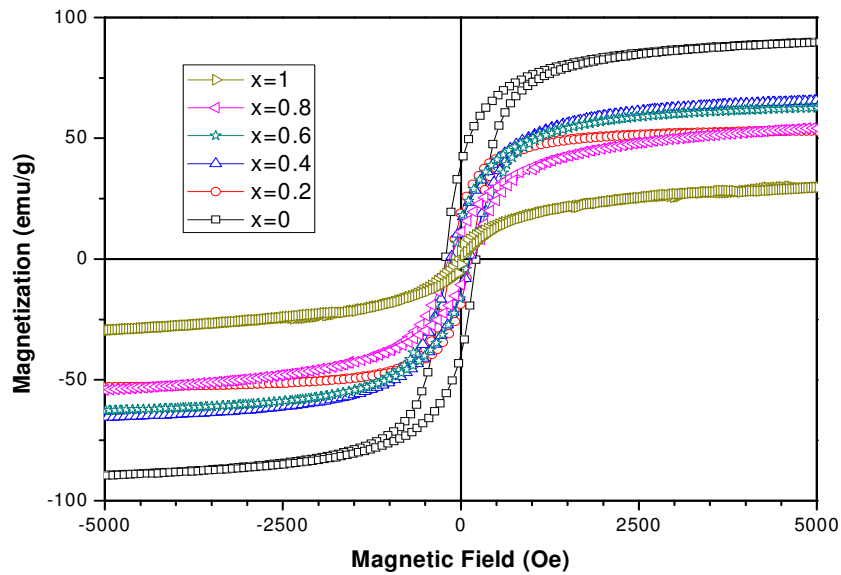


Figure 4.51 Magnetization vs Applied magnetic field curves of $Zn_xNi_{1-x}Fe_2O_4$ nanoparticles ($x = 0$ to 1) at 10 K.

The M_s is slightly decreasing from 100 emu/g to 50 emu/g with increasing Zn content, because Zn has no magnetic moment and M_r values are lower than 25 emu/g except for Zn ferrite ($x = 0$) as shown in Fig. 4.51 and Fig. 4.52, [75].

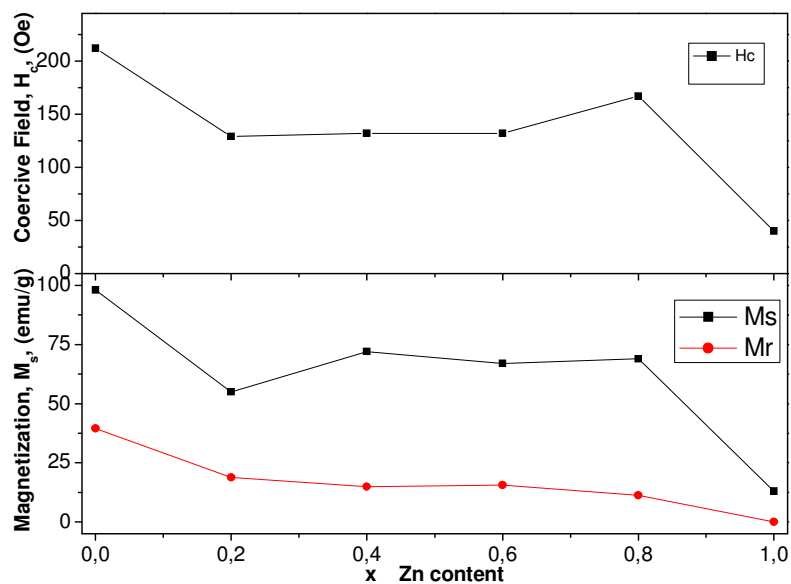


Figure 4.52 Zn composition dependent H_c , M_r and M_s values of 10 K hysteresis curves.

For the ferrite samples, the non-saturated magnetization curve even at 5 kOe suggests the existence of strong antiferromagnetic inter-cluster interactions mixed with ferromagnetic interactions inside the clusters [65, 68]. The co-existence of ferromagnetic and antiferromagnetic mechanism can also cause the canted spin structures inside the clusters.

The observed magneton numbers with VSM are summarized in Table 4.10. The calculated magneton number using XRD data agree very well with the experimentally obtained magneton number by VSM, which confirms the collinear magnetic structure in Zn doped Ni ferrites.

CHAPTER 5

CONCLUSION

The effects of synthesis methods and catalyzers on the structural and characteristic properties of $Zn_xNi_{1-x}Fe_2O_4$ nanoparticles were studied. The substitution of zinc (with a of molar variation from $x = 0$ to 1) was analyzed in Ni-ferrites, successfully prepared by microwave combustion method and PEG-assisted hydrothermal method. In detail, urea and citric acid are used as a fuel in microwave combustion method and PEG 400 is used as a surfactant in hydrothermal method.

The samples synthesized by microwave combustion method using citric acid as fuel, resulted Ni-Zn ferrite nanoparticles with the spinel structure at absorptions of $578 - 619 \text{ cm}^{-1}$ in wavenumber and with crystallite sizes in the range of $19 - 31 \text{ nm}$ where measurements performed in FT-IR and X-Ray powder diffractometer. The linear increase in the lattice parameters from 8.34 to 8.43 \AA by increasing zinc substitution is also observed. Citric acid synthesis provided higher saturation magnetization and coercivity when the Zn is decreased in the contribution. Samples revealed ferromagnetic behavior at the room temperature measurements of VSM, with saturation magnetizations in the interval of $18 - 76 \text{ emu/g}$ and coercivities in the $81 - 187 \text{ Oe}$ range. The TEM micrographs, which are used to obtain information for morphology, showed blurred images for samples. Sizes calculated from the XRD measurements are compared with the TEM results in which, a good agreement is obtained.

The synthesis of the samples by using urea, the absorbance of the Ni-Zn spinels is measured in $584 - 616 \text{ cm}^{-1}$ interval. The linear dependence of zinc substitution in the lattice constants from 8.34 to 8.43 \AA is observed for urea as well. Crystallite sizes are

calculated in the range of 23 – 35 nm, and those sizes are found good agreement (± 3 nm) with the TEM images. The lack of saturation, tiny coercivity and the absence of the remanent magnetization showed that the samples are superparamagnetic at room temperature. The difference of this behavior between citric acid and urea should be attributed to the molar heat differences of urea and citric acid that used as fuels during the synthesis process. Because of the lower heat transfer ignition of urea can not effect formation of well crystallinity.

Finally, the samples synthesized with the hydrothermal method with a substitution of Zn are analysed. Wavenumbers for samples synthesized by using PEG 400 are found in the range of 574 – 602 cm^{-1} where these datas are lower compared with the Ni-Zn spinels in the microwave combustion synthesis. The linear increase in lattice constant from 8.38 to 8.45 Å by increasing zinc substitution is also observed. The particle sizes calculated by using Debye-Scherrer formula from the output of the XRD device are found in the range of 11 – 30 nm. M-H curves, measured at room temperature resulted superparamagnetic behavior for PEG assisted synthesis of samples. The increase in saturation magnetization (from 5 – 78 emu/g at room temperature, to 36 – 94 emu/g at 10 K temperature) and the coercivity in the magnetization measurements at 10 K temperature denoted that particles are ferromagnetic. The decrease of blocking temperature by increasing Zn content is also observed from the FC (100 Oe) and ZFC measurements. The particle sizes are fitted using cation distribution in octahedral and tetrahedral sites and it is seen that, the results from the profiles fit were in 9 – 27 nm interval. VSM sizes are fitted by Langevien function where the particle size range was found as 9 – 22 nm from the magnetic measurements which shows the existence of magnetic cores and nonmagnetic shells. The size of particles generally increases by substitution of zinc. In the theoretical cation distribution study, the Zn^{+2} cations are mostly found in octahedral site by the estimated causes such as low temperature synthesis and coating effects. The Fe^{+3} cations sited remarkably in tetrahedral site. So the samples have partly inverse spinel structure, close to the inverse, according to the calculations. The calculated results agreed well with the results of the magnetic measurements. Finally TEM micrographs were taken. The size estimations by counting from the TEM image are done with a range of 13 – 37 nm. All these results agreed with each other in particle sizes for the samples synthesized with PEG 400. The lower values

in particle sizes compared with the microwave combustion method, should be a result of PEG which prevents the agglomeration during the synthesis process.

Generally, from magnetic measurements, at high temperatures, remanent magnetization and coercivity were observed for Ni-ferrites. When zinc is substituted to Ni-ferrites, they show non-saturated hysteresis curve and non-zero magnetic moments as expected for Zn-ferrite. Replacing some of Ni ions with Zn ions generally decreases the saturation magnetization and coercivity of the sample compared with Ni-ferrite.

As a result, the nanoparticles showing superparamagnetic properties can be used as a contrast agent in MRI, drug carrier and in hypothermia. The nanoparticles indicating ferro-ferrimagnetic properties can be used in magnetic recording, read-write heads, etc.

Finally, microwave absorbing properties and electrical properties of these nanoparticles will be studied later on.

REFERENCES

- [1] D.S. Mathew, R.S. Juang, Chem. Eng. Journ., 129 (2007), 51.
- [2] T. Ozkaya, M. S. Toprak, A. Baykal, H. Kavas, Y. Köseoğlu, B. Aktaş, Jour. All. And Comp., (2008), doi:10.1016/j.jallcom.2008.04.101.
- [3] P. Poddar, J. Gass, D.J. Rebar, S. Srinath, H. Srikanth, S.A. Morrison, E.E. Carpenter, J. Magn. Magn. Mater., 307 (2006), 227.
- [4] A.E. Virden, K. O'Grady, J. Magn. Magn. Mater., 290 (2005), 868.
- [5] J.Y. Lee, G.J. Lee, H.S. Kim, S.H. Lee, D.H. Lee, C.H. Yo, K.H. Kim, K. Ahn, Mat. Chem. and Phy., 52 (1998), 270.
- [6] A. Baykal, N. Kasapoğlu, Y. Köseoğlu, M. S. Toprak, H. Bayrakdar, Jour. All. And Comp., (2007), doi:10.1016/j.jallcom.2007.10.041.
- [7] N. Kasapoğlu, A. Baykal, Y. Köseoğlu, M.S. Toprak, Script. Mat., 57 (2007) , 441.
- [8] Y. Li, Q. Li, M. Wen, Y. Zhang, Y. Zhai, Z. Xie, F. Xu, S. Wei, J.Elec.Spec. And Rel. Pheno., 160 (2007), 1.
- [9] A. Kundu, C. Upadhyay, H.C. Verma, Phy. Lett. A, 311 (2003), 410.
- [10] H.Ehrhardt, S.J.Campbell, M.Hofmann, Scrp. Mat., 48 (2003), 1141.
- [11] M. Sorescu, L. Diamandescu, R. Peelamedu, R. Roy, P. Yadoji, J. Magn. Magn. Mater., 279 (2004), 195.
- [12] M. M. Bahout, S. Bertrand, O. Peña, Journ. Sol. Stat. Chem., 178 (2005), 1080.
- [13] G. Vaidyanathan, S. Sendhilnathan, R. Arulmurugan, J. Magn. Magn. Mater., 313 (2007), 293.
- [14] A. Verma, R. Chatterjee, J. Magn. Magn. Mater., 306 (2006), 313.
- [15] D. Arcos, R. Valenzuela, M. Vázquez, M. Vallet-Regí, 141 (1998), 14.
- [16] R. Arulmurugan, G. Vaidyanathan, S. Sendhilnathan, B. Jeyadevan, Physica B, 363 (2005), 228.
- [17] C.K. Kim, J.H. Lee, S.Katoh, R.Murakami, M.Yoshimura, Mat.Res.Bull., 36 (2001), 2241.
- [18] S.S. Kim, D.H. Han, IEEE Trans. Mag. , 30 (1994), 4554.
- [19] M. Sorescu, L. Diamandescu, D.T. Mihaila, V. Teodorescu, Mat. Chem. And Phy., 273 (2007), 1.
- [20] A. Dias, R.L. Moreira, Mat. Lett., 39 (1999), 70.

- [21] M. M. Bucko, K. Haberko, *Jour. of Eur. Cer. Soc.*, 27 (2007), 723.
- [22] J.H. Lee, C.K. Kim, S.Katoh, R. Murakami, *Jour. All. And Comp.*, 325 (2001), 276.
- [23] M. Sertkol, Y. Köseoğlu, A. Baykal, H. Kavas, A.C. Başaran, *J. Magn. Magn. Mater.*, (2008), doi:10.1016/j.jmmm.2008.08.083.
- [24] Y. Köseoğlu, A. Baykal, M. S. Toprak, F. Gözüak, A. C. Başaran, B. Aktaş, *Jour. All. And Comp.*, 462 (2008), 211.
- [25] G. Vaidyanathan, S. Sendhilnathan, *Physica B*, 403 (2008), 2157.
- [26] D. Zhao, X. Wu, H. Guan, E. Han, *J. Supercritical Flu.*, 42 (2007), 226
- [27] S.H. Yu, T. Fujino, M. Yoshimura, *J. Magn. Magn. Mater.*, 256 (2003), 421.
- [28] Z. Chen, L. Gao, *Mat. Sci. And Eng. B*, 141 (2007), 82.
- [29] K. Byrappa, T. Adschiri, *Prog. Cry. Grow. and Char. Mat.*, 53 (2007), 121.
- [30] D.E. Zhang, X.J. Zhang, X.M. Ni, H.G. Zheng, D.D. Yang, *J. Magn. Magn. Mater.*, 292 (2005), 79.
- [31] <http://www.tompotter.us/b.html>.
- [32] http://www.aacg.bham.ac.uk/magnetic_materials/type.htm
- [33] D. Craik, *Magnetism Principles and Applications*, John Wiley & Sons, Great Britain, 1995.
- [34] T.K. McNab, R.A. Fox, A.J.F. Boyle, *J. App. Phys.*, 39 (1968), 5703.
- [35] R.N. Panda, N.S. Gajbhiye, G. Balaji, *Jour. All. And Comp*, 326 (2001), 50.
- [36] Y. Köseoğlu, H. Kavas, *Jour. of Nanosci. and Nanotech.*, 8 (2008), 584.
- [37] http://www.rareearth.org/magnets_magnetism.htm.
- [38] Y. Köseoğlu, H. Kavas, B. Aktaş, *Phys. Stat. Sol. (a)*, 203 (2006), 1595.
- [39] Qing Song, "Size And Shape Controlled Synthesis And Superparamagnetic Properties Of Spinel Ferrites Nanocrystals", Ph.D. Thesis, Georgia Institute of Technology, Georgia, 2005.
- [40] F.S. Li, L. Wang, J.B. Wang, Q.G. Zhou, X.Z. Zhou, H.P. Kunkel, G. Williams, *J. Magn. Magn. Mater.*, 268 (2004), 332.
- [41] O. Masala, D. Hoffman, N. Sundaram, K. Page, T. Proffen, G. Lawes, R. Seshadri, *Sol. Stat. Sci.*, 8 (2006), 1015.
- [42] C.C. Hwang, J.S. Tsai, T.H. Huang, C.H. Peng, S.Y. Chen, *Jour. of Sol. Stat. Chem.*, 178 (2005), 383.
- [43] C. Kittel, *Introduction to Solid State Physics*, Wiley, Newyork, 1996.

- [44] F. Li, X. Liu, Q. Yang, J. Liu, D.G. Evans, X. Duan, *Mat. Res. Bull.*, 40(2005), 1250.
- [45] J.Smit, H.P.J.Wijn, *Ferrites*, vol.44, Philips Techno.Library, Eindhoven, Netherlands, 1959.
- [46] A.M. El-Sayed, *Ceram. Int.*, 28 (2002), 363.
- [47] C.K. Kim, J.H. Lee, S.Katoh, R.Murakami, M.Yoshimura, *Mat. Res. Bull.*, 36 (2001), 2241.
- [48] O. Carp, L. Patron, A. Reller, *Mat. Chem. and Phys.*, 101 (2007), 146.
- [49] A.C.F.M. Costa, V.J. Silva, D.R. Cornejo, M.R. Morelli, R.H.G.A. Kiminami, L. Gama, *J. Magn. Magn. Mater.*, 320 (2008), e371.
- [50] J.Gao, Y.Cui, Z.Yang, *Mat. Sci. and Eng. B*, 110 (2004), 111.
- [51] M.G. Buerger, *Crystal Structure Analysis*, Wiley Interscience, New York, 1960.
- [52] H. Ohnishi, T. Teranishi, *J.Phys. Soc Jpn.*, 6 (1969), 36.
- [53] S.Singhal, K.Chandra, *Jour. Sol. Stat. Chem.*, 180 (2007), 296.
- [54] Wohlfarth, *Ferromagnetic materials*, Vol 3, North holland Publishing Company, 1982.
- [55] Q.M. Wei, J.B. Li, Y.J. Chen, Y.S. Han, *Mat. Chem. and Phys.*, 74 (2002), 340.
- [56] L. Nell, *C.R. Acad. Sci.*, 230 (1950), 375.
- [57] M. U. Rana, M.-ul Islam, T. Abbas, *Mat. Chem. and Phys.*, 65 (2000), 345.
- [58] H.H. Joshi R.G. Kulkarni, *J. Mat. Sci.*, 21 (1986), 2138.
- [59] P.K. Roy, J. Bera, *Jour. of Mat. Pro. Tech.*, 197 (2008), 282.
- [60] F. Li, H. Wang, L. Wang, J. Wang, *J. Magn. Magn. Mater.*, 309 (2007), 295.
- [61] T. Wejrzanowski, R. Pielaszek, A. Opalinska, H. Matysiak, W. Łojkowski, K.J. Kurzydłowski, *App. Sur. Sci.*, 253 (2006), 204.
- [62] T. Kim, and M. Shima, *J. App. Phys.*, 101 (2007), 09M516.
- [63] D. Chen, D. Chen, X. Jiao, Y.Zhao, M. He, *Powder Tech.*, 133 (2003), 249.
- [64] H. Nathani, S. Gubbala, R.D.K. Misra, *Mat. Sci. And Eng. B*, 111 (2004), 95.
- [65] R.N. Bhowmik, R. Ranganathan, *J. Magn. Magn. Mater.*, 248 (2002), 101.
- [66] H. Nathani, R.D.K. Misra, *Mat. Sci. And Eng. B*, 113 (2004), 228.
- [67] R. K.Selvan, C.O. Augustin, C. Sanjeeviraja, D. Prabhakaran, *Sol.Stat. Com.*, 137 (2006), 514.
- [68] D. Fiorani, S. Vitiocoli, J.L. Dorman, J.L. Tholence, A.P. Murani, *Phys. Rev. B*, 30 (1984), 2776.

- [69] R.W. Chantrell, N.S. Walmsley, J. Gore, M. Maylin, *J. Appl. Phys.*, 85 (1999), 4340.
- [70] T. Song, R.M. Roshko, *IEEE Trans. Magn.*, 36(2000), 223.
- [71] V.I. Nikolaev, T.A. Bushina, K. E. Chan, *J. Magn. Magn. Mater.*, 213(2000), 213.
- [72] J.T. Lue, *J. Phys. and Chem. Sol.*, 62 (2001), 1599.
- [73] M.F. Hansen, S. Morup, *J. Magn. Magn. Mater.*, 184 (1998), 262.
- [74] R. Arulmurugan, G. Vaidyanathan, S. Sendhilnathan, B. Jeyadevan, *J. Magn. Magn. Mater.*, 298 (2006), 83.
- [75] K. Yakushiji, S. Mitani, K. Takanashi, J.G. Ha, H. Fujimori, *J. Magn. Magn. Mater.* , 212 (2000), 75.
- [76] H.E. Zhang, B.F. Zhang, G.F. Wang, X.H. Dong, Y. Gao, *J. Magn. Magn. Mater.*, 312 (2007), 129.